PETROGRAPHY AND TRACE ELEMENT CHEMISTRY OF CALCITE VEINS IN THE DEEP DRILL 1972 DRILL CORE, BERMUDA ISLANDS

Michael Powell

SUBMITTED IN PARTIAL FULFILLMENT OF THE REQUIREMENTS FOR
THE DEGREE OF BACHELOR OF SCIENCES, HONOURS
DEPARTMENT OF EARTH SCIENCES
DALHOUSIE UNIVERSITY, HALIFAX, NOVA SCOTIA

Abstract

The Deep Drill 1972 drill core of the Bermuda Islands provides a representative sampling of Bermuda's volcanic basement lithologies. Although there have been studies of the two primary lithologies over the past 50 years, no published work has characterized the nature of geological veining found throughout the core. Veins are defined by the shape and chemistry of their minerals, which are representative of the physical and chemical conditions under which the veins developed. This work focuses on petrographic description and mineral chemistry of veins in a selection of 13 samples from the mafic units of Bermuda. Optical microscopy reveals that veins are predominantly blocky calcite. All sample veins are interpreted to be syntaxial. Wavelength-dispersive spectroscopy point analyses and element mapping shows that calcite across all samples is chemically homogenous, with zoning produced by varying manganese concentration occurring in just one sample. Laser ablation inductively coupled plasma mass spectrometry was carried out for rare earth element + yttrium analyses on select samples. Rare earth element + yttrium signatures indicate that most samples represent high-temperature hydrothermal fluid with possible remobilization, with the sample containing manganese-zoned calcite showing an ambiguous, mixed-fluid trend. These findings suggest that vein minerals in the Bermuda mafic units precipitated from a fluid which was low velocity or stagnant, above 250˚C, and did not undergo significant chemical change as calcite precipitation progressed. This work lays the basis for future study on the veins of the Deep Drill 1972 drill core which should produce a representative sample of veins and expand the suite of analytical tools.

Key Words: Calcite, Vein, Deep Drill 1972, Bermuda igneous basement, Petrography

Table of Contents

Abstract ..... **i**

Table of Contents ..... **ii**

List of Tables ..... **iv**

List of Figures ..... **v**

List of Abbreviations ..... **ix**

Acknowledgements ..... **x**

Chapter 1: Introduction **1**

1.1 Background on Bermuda 1

1.2 Motivation for Study 2

1.3 Vein Formation and Mineral Growth 3

1.4 Chemical Signatures of Vein Minerals 6

1.5 Thesis Objectives 10

Chapter 2: Methods **11**

2.1 Sample Selection 11

2.2 Laboratory Methods 11

Chapter 3: Results **13**

3.1 Sample Suitability Assessment 13

3.2 Morphological and Phase Descriptions 14

3.3 EMP Analysis of Select Samples 40

3.4 Calcite Substitution Characterization 53

3.5 REY in Calcite 54

Chapter 4: Discussion **61**

4.1 Vein Mineral, Crystal Shape, and Vein Texture Interpretation 61

4.2 Calcite Chemistry Interpretation 63

4.3 Fluid Source from REY 64
4.4 Limitations 67
4.5 Proposal for Future Study 68
Chapter 5: Conclusions **69**
References **70**

List of Tables

Table 1	Summary of samples and techniques used.	13
Table 2	WDS spot analysis results for calcite in sample 62.1207.	40
Table 3	WDS spot analysis results for calcite in the pure calcite vein in sample 72.1387.	41
Table 4	WDS spot analysis results for calcite in the mixed phase vein in sample 72.1387.	42
Table 5	WDS spot analysis results for calcite in the single domain side of the vein in sample 113.2202.1.	43
Table 6	WDS spot analysis results for calcite in the dual domain side of the vein in sample 113.2202.1.	46
Table 7	WDS spot analysis results for calcite in sample 123.2396A.	47
Table 8	WDS spot analysis results for calcite in sample 123.2409 in the main vein.	48
Table 9	WDS spot analysis results for calcite in sample 123.2409 in the small vein.	49
Table 10	REY patterns for sample 62.1207.	54
Table 11	REY patterns for sample 72.1387.	55
Table 12	REY patterns for sample 113.2202.1	56
Table 13	REY patterns for sample 123.2396A.	58
Table 14	REY patterns for sample 123.2409.	59

List of Figures

Figure 1	Map of Bermuda and drillhole locations from Olsen 2005.	1
Figure 2	Summary of crystal shapes and vein textures from Bons et al. 2012.	5
Figure 3	High- vs low-temperature hydrothermal fluids from Sharma and Srivastava 2014.	8
Figure 4	Characteristic REY trends for fluids from Zhao et al. 2021.	9
Figure 5	Thin section image of sample 14.313	15
Figure 6	Cross-polarized light image of sample 14.313	16
Figure 7	Thin section scan of sample 29.599	17
Figure 8	Cross-polarized light image of sample 29.599	18
Figure 9	Thin section scan of sample 47.924	19
Figure 10	Cross-polarized light image of sample 47.924	20
Figure 11	Thin section scan of sample 62.1204.4	21
Figure 12	Cross-polarized light image of sample 62.1204.4	22
Figure 13	Thin section scan of sample 62.1207	23
Figure 14	Cross-polarized light image of sample 62.1207	24
Figure 15	Epoxy mount scan of sample 72.1387	25

Figure 16 Thin section scan of sample 113.2200.5 26

Figure 17 Cross-polarized light image of sample 113.2200.5 27

Figure 18 Thin section scan of sample 113.2202.1 28

Figure 19 Cross-polarized light image of sample 113.2202.1 29

Figure 20 Thin section scan of sample 123.2393 30

Figure 21 Cross-polarized light image of 123.2393 31

Figure 22 Thin section scan of sample 123.2396A 32

Figure 23 Cross-polarized light image of sample 123.2396A 33

Figure 24 Thin section scan of sample 123.2396B 34

Figure 25 Cross-polarized light image of sample 123.2396B 35

Figure 26 Thin section scan of sample 123.2400 36

Figure 27 Cross polarized light image of sample 123.2400 37

Figure 28 Thin section scan of sample 123.2409 38

Figure 29 Cross polarized light image of sample 123.2409 39

Figure 30 BSE image of sample 62.1207 40

Figure 31 BSE image of the pure calcite vein in sample 72.1387 41

Figure 32 BSE image of the mixed phase vein in sample 72.1387 42

Figure 33 BSE image of the single domain side of the vein in sample 113.2202.1 43

Figure 34 BSE image of the dual domain side of the vein in sample 113.2202.1 45

Figure 35 BSE image of sample 123.2396A 47

Figure 36 BSE image of sample 123.2409 in the main vein. 48

Figure 37 BSE image of sample 123.2409 in the small vein. 49

Figure 38 Element map of sample 62.1204.4 50

Figure 39 Element map of sample 62.1207 51

Figure 40 Element map of sample 72.1387 52

Figure 41 Scatterplots of common Ca substitutions. 53

Figure 42 REY trends for sample 62.1207. 54

Figure 43 REY trends for sample 72.1387. 55

Figure 44 REY trends for sample 113.2202.1. 56

Figure 45 REY trends for sample 123.2396A 58

Figure 46 REY trends for sample 123.2409. 59

Figure 47 REY data divided by sample to show different trends. 66

List of Abbreviations

Back-scattered electron (BSE)
Calcium (Ca)
Celsius (C)
Centimeter (cm)
Cerium (Ce)
Dysprosium (Dy)
Electron microprobe (EMP)
Electron-dispersive spectrometer (-try) (EDS)
Erbium (Er)
Europium (Eu)
Feet (ft)
Gadolinium (Gd)
Heavy rare earth elements (HREE(s))
Holmium (Ho)
Lanthanum (La)
Laser ablation inductively-coupled plasma mass spectrometer (-try) (LA-ICP-MS)
Lead (Pb)
Light rare earth elements (LREE(s))
Lutetium (Lu)
Medium rare earth elements (MREE(s))
Metre (m)
Millimeter (mm)
Nova Scotia (NS)
Parts per million (ppm)
Post Archaean Australian Shale (PAAS)
Praseodymium (Pr)
Promethium (Pm)
Rare earth elements (REE(s))
Rare earth elements and yttrium (REY(s))
Rubidium (Rb)
Samarium (Sm)
Scanning electron microscopy (SEM)
Silica (SiO_2)
Silicon (Si)
Strontium (Sr)
Terbium (Tb)
Thulium (Tm)
Uranium (U)
Wavelength-dispersive x-ray spectrometer (-try) (WDS)
Weight % (wt%)
Ytterbium (Yb)
Yttrium (Y)

Acknowledgements

My heartfelt thanks go out to the entire department of Earth and Environmental Sciences at Dalhousie University, which I have called my home for the past four years. Particularly, I would like to thank all members of the Dawson Geology Club, both past and present, for contributing to an excellent undergraduate experience. I thank my fellow honours classmates and Dr. Tarah Wright for their support throughout the completion of this thesis. Dan MacDonald, Xiang Jang, and Bryan Maciag all have my thanks for their help with the analytical techniques found herein. And above all, I thank Dr. Lexie Arnott for being my supervisor on this project, and for providing calmness when patience was pertinent, sternness when diligence was demanded, and laughter when a reprieve was required.

Chapter 1: Introduction

1.1 Background on Bermuda

The Bermuda Islands are the largest of four northeast trending carbonate seamounts perched on the Bermuda Rise, a 1500km long expanse of igneous units rising roughly 1km above the oceanic crust (Vogt and Jung 2007). Despite a handful of shallow boreholes penetrating these units, very little igneous material had been recovered until researchers from Dalhousie University drilled a drill core in 1972 providing a 767m record of igneous material (Aumento and Gunn 1974; Olsen 2005; Figure 1).

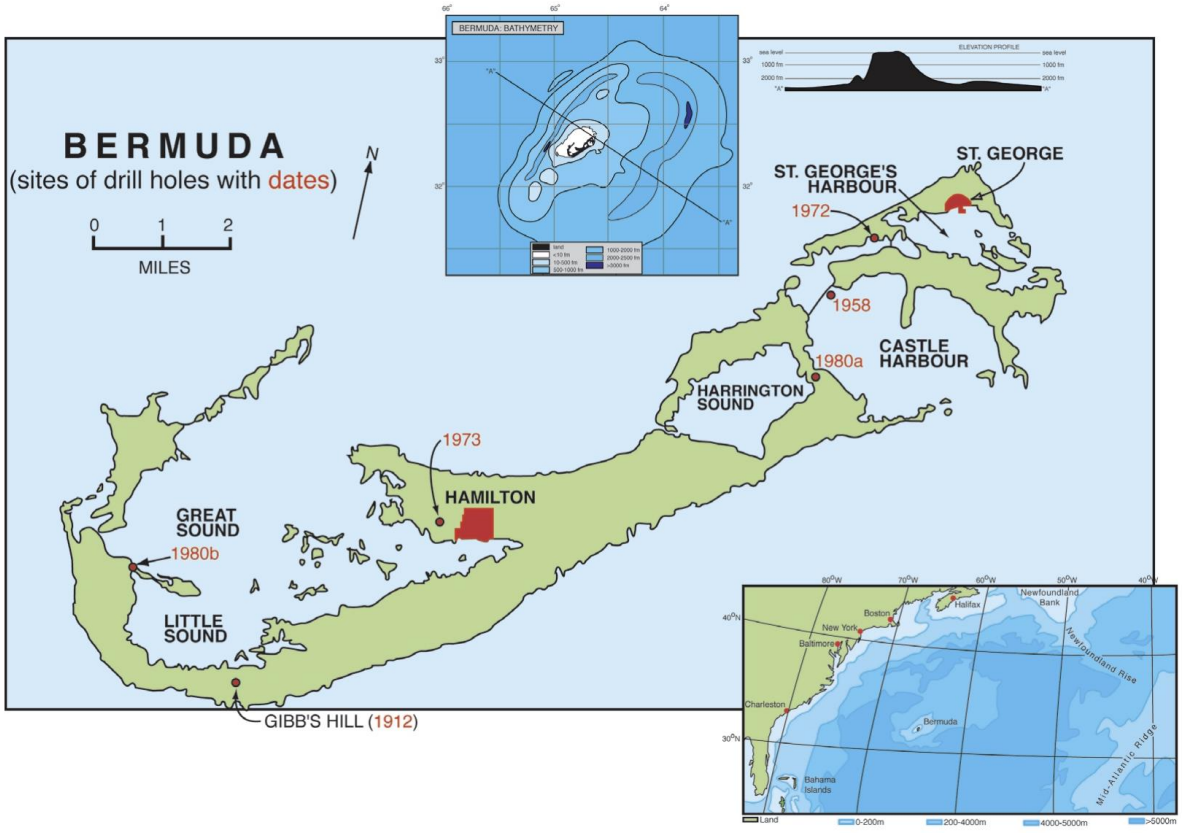

Figure 1 The Bermuda Islands, including the location of drillholes (red circles), bathymetric data (both insets), and the location of Bermuda in the Atlantic Ocean (bottom right inset). From Olsen 2005.

Assessment of the Deep Drill 1972 drill core reveals two distinct igneous units of mafic volcanic flows (uncertain age ~40-100Ma) and ultramafic composition dykes (~30Ma age) which were both emplaced as hundreds of thin layers (Aumento and Gunn

1974; Olsen 2005; Vogt and Jung 2007; Mazza et al 2019). Geochemical analysis shows that mafic units have a silica (SiO_2) content of 49.7-54.9 wt% with pervasive alteration and the presence of pillow structures (Olsen 2005; Mazza et al. 2019). The ultramafic units display a silica undersaturated composition (SiO_2 < 42.4wt%), exceptionally high calcium (Ca), volatile, and trace element content, and are less altered than the mafic units (Olsen 2005; Mazza et al. 2019).

The geological and thermodynamic model for the development of these volcanic units has been debated; hypotheses include an intraplate mantle plume model, an unconventional “lava lamp” plume model, and a localized convection plume-absent model (Vogt and Jung 2007; Mazza et al. 2019). Various conflicting observations exist for each proposed model. The typical hotspot model would necessarily lead to the production of additional volcanic extrusions along the seafloor, but none are known to exist (Vogt and Jung 2007). Some authors have attempted to explain the Bermuda igneous suites as related to igneous units found within the continental United States of America, thus proposing “lava lamp” plume models in which infrequent pulses of magma are released; numerous spatiotemporal issues exist for these models (Morgan 1981; Duncan 1984; Vogt and Jung 2007). Most recently a local convection model which does not require the presence of a mantle plume has been proposed to explain the extreme composition of ultramafic layers (Mazza et al. 2019).

1.2 Motivation for Study

Despite previous characterization of the igneous basement units of Bermuda, no known works have characterized the secondary veining and related breccias found throughout the Deep Drill 1972 drill core. Indeed, it is common practice to intentionally avoid these vein features as they often represent a decoupled mineralization event leading to alteration of the host rock (for example, see Mazza et al. 2019 sampling methods). The precise relationships between these vein features and the mafic and ultramafic units are unknown.

Characterizing the veins present in the igneous units of the Deep Drill 1972 core is needed to fully understand the geological processes which have occurred during the

development of Bermuda. Identifying vein modes and crystal shapes provides insight into the physical-chemical environment of the igneous basement at the time of vein formation. Trace element analysis of vein calcite can reveal the nature of the fluid from which they precipitated, allowing us to identify whether they are related to magmatic fluid exsolution, high-temperature hydrothermal fluid, low-temperature hydrothermal fluid, or ambient seawater (similar to seafloor alteration).

1.3 Vein Formation and Mineral Growth

Veins are defined as mineral precipitates nucleating from a nutrient-saturated fluid (nutrients being those elements required for mineral formation) and growing into a void space created through dilational stress and brittle fracturing of the host rock (Bons et al. 2012). Veins can be categorized based on both their morphological and geochemical characteristics. Over broader physical scales, such as in outcrop, vein morphology can be related to the regional tectonic regime as characteristics such as vein spacing, length, and sigmoidicity (Bons et al. 2012). On the finer physical scales relevant to the current work, such as those observed in rock cores, vein morphology is primarily defined by crystal morphology and growth direction (Bons et al. 2012).

Crystal morphology and growth direction in vein minerals are a consequence of the competing effects of deformation and crystal precipitation. The fundamental mechanism is the so-called crack-seal mechanism, a term coined by Ramsay (1980). As a rock fractures (the “crack”), fluid enters the fracture and begin to precipitate crystals. These crystals fill void space within the crack and will eventually fill the space entirely, preventing further precipitation (the “seal”). Throughout a deformational event, this process can occur once or repeat dozens of times (Ramsay 1980). Subsequent works have expanded on the crack-seal mechanism, with new theories allowing for no time between the crack and the seal. In this case, mineral precipitation occurs instantaneously with void space development thus inhibiting nucleation and requiring crystallographically-preferred growth (Bons and Montenari 2005). In effect, this means that no “crack” truly occurs as the void space is filled immediately.

Where the crack-seal mechanism describes the mechanism for vein development, mineral shape is more directly controlled by the location of the growth direction(s). Growth of precipitating crystals may occur in one direction from the vein wall toward the centre of the vein. Such veins are called syntaxial veins (Bons et al. 2012). If nucleation occurs along the vein wall and crystal growth is sufficiently rapid, an elongate or fibrous crystal shape may result because of crystallographically-preferred growth (Figure 2). Alternatively, growth competition may occur, with nucleation outpacing the growth of previously precipitated crystals, resulting in a blocky, equant shape (Figure 2). Syntaxial veins can arise from a single crack-seal cycle or numerous crack-seal cycles (Bons et al. 2012; Figure 2). In contrast, growth of precipitating crystals may occur in two directions, from the centre of the vein toward the vein wall, and where there are no clear crack-seal cycles as discussed above. Such veins are called antitaxial veins (Bons et al. 2012). Within antitaxial veins there is always some “median zone” at the centre of the veins from which the two growth planes extend (Figure 2).

Bons et al. (2012) suggest that where numerous crack-seal cycles occur and the location of the growth plane is variable, a vein may be termed a “stretching vein” (Figure 2). This requires careful interpretation when the term “stretch(-ed/-ing)” is used, as it is used in one sense as a crystal shape descriptor and in the other as a textural interpretation.

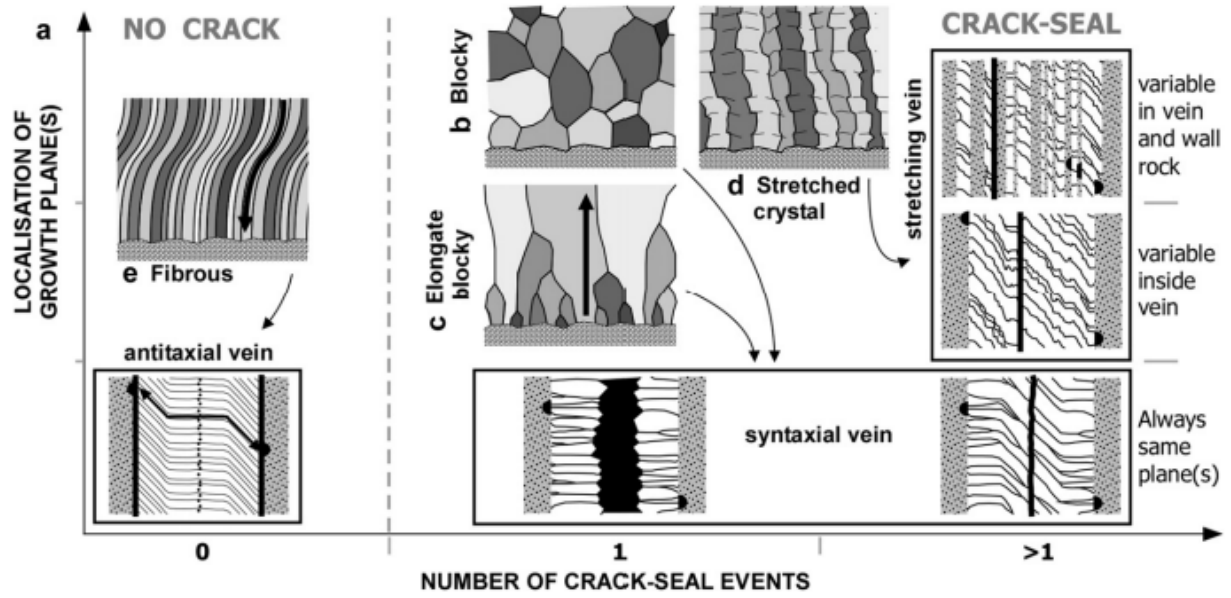

Figure 2 Overview of vein mineral morphologies and their relationship to the number of crack-seal cycles and the variability of the growth direction(s). Antitaxial veins are distinguished in that they have no clear crack-seal separation as mineral precipitation occurs simultaneously with dilation. They have two growth directions, each leading from the median zone toward the vein wall. Syntaxial veins can have one or many crack-seal cycles, but always demonstrate a single growth direction from vein wall to the centre of the vein. Bons et al. (2012) define a “stretching vein” texture, in which the number of crack-seal events is very high and the growth direction is variable. Figure from Bons et al. 2012.

The physical-chemical factors controlling nucleation location, nucleation rate, and growth direction, and their relationship to crystal shape, are numerous and varied. The fundamental consideration for crystal precipitation is fluid supersaturation, which is achieved when the Gibbs free energy of the solute is greater than what it would be in solid form (Oliver and Bons 2001; Griffin et al. 2014). Temperature, pressure, pH, Eh, redox conditions, fluid residence time, fluid velocity, fluid immiscibility, fluid mixing, reaction with the host rock, and the temporal changes in all of these factors as crystallization progresses, can change the solubility of precipitate minerals and thus change the point at which the fluid reaches supersaturation (Oliver and Bons 2001; Bons et al. 2012). Furthermore, the concentration of minor and trace elements in solution can affect nucleation and crystal shape as cation substitution reactions occur in mineral precipitates (Barker and Cox 2011). The present work does not attempt to capture all of these factors,

but instead focuses on the identification of the vein minerals, variation (or lack thereof) in vein mineral crystal shape, interpretation of crystal shape in terms of vein development, and the concentration of minor and trace elements in these vein crystals.

1.4 Chemical Signatures of Vein Minerals

Vein minerals are constituted of the nutrients present in the fluid, which vary according to the fluid source (e.g. magmatic, seawater, etc.). While many minerals can be deposited in veins, the most common vein minerals are calcite and quartz (Bons et al. 2012). Fluid-host rock mass transfer can affect the nutrient budget for vein minerals, with the competing effects of fluid diffusion and fluid advection either contributing to or reducing the budget of the fluid according to the permeability of the host rock.

When permeability is low, diffusion contributes more to the total nutrient budget relative to advection. In analyses of diffusion-fed veins, it has been found that diffusion depletes the host rock locally, contributing up to 80% of the nutrients required to form vein minerals, and that these veins can be of centimeter-scale widths (Fisher et al. 1995). Conversely, when permeability is high, fluid advection contributes more to the nutrient budget than diffusion. Advection can occur over crustal scales (Oliver and Bons 2001; Bons et al. 2012). Veins dominated by advection result in less reaction with the host rock and precipitating a chemical signature faithful to that of the advecting fluid (Bons et al. 2012).

The rare earth elements (REE) are comprised of the lathanide series of elements: lanthanum (La), cerium (Ce), praseodymium (Pr), promethium (Pm), samarium (Sm), europium (Eu), gadolinium (Gd), terbium (Tb), dysprosium (Dy), holmium (Ho), erbium (Er), thulium (Tm), ytterbium (Yb), and lutetium (Lu). Yttrium (Y) is commonly included in REE analysis by Earth scientists due to its similarities to Ho; when Y is included, these elements are collectively abbreviated as REY(s) (Migaszewski and Galuszka 2014). REYs are considered “trace elements” because they compose <1000 parts per million (ppm) (<0.1 weight% (wt%)) in most geologic systems (Kennedy 1999). REYs can be grouped according to their mass, with La to Eu representing the light rare earth elements (LREEs) and Gd to Lu (including Y) representing the heavy rare earth elements (HREEs).

REYs are typically trivalent, but divalent species can occur (most commonly in Eu), along with rare tetravalent species (most commonly in Ce). The middle rare earth elements (MREEs) are occasionally referenced as Sm to Ho, but this classification is not considered in the current work (Migaszewski and Galuszka 2014). The chemical behaviour of REYs changes systematically due to the progressive filling of the 4f electron shells from 0 electrons in La to 14 electrons in Lu, and due to the progressive reduction in ionic radius from La to Lu (Zhao et al. 2021). REYs are normalized to reference standards to account for the Oddo-Harkins effect; this eliminates the “zig-zag” pattern observed in REYs (Migaszewski and Galuszka 2014). Normalization also allows for comparison of different chemical environments to a set reference point. In carbonate systems, the most commonly used reference standard is the post-Archaean Australian Shale (PAAS) (McLennan 1989; Migaszewski and Galuszka 2014; Zhao et al. 2021)

The systematic change in behaviour of REYs leads to fractionation of REYs representative of the chemical environment from which they are substituted, with reference to the chosen normalization. REYs can substitute into carbonate minerals according to Equations 1.0, 2.0, and 3.0 (Zhao et al. 2021):

$$2Ca^{2+} = REY^{3+} + Na^{+}$$

Equation 1.0

$$3Ca^{2+} = 2REY^{3+} + \square$$

Equation 2.0

$$Ca^{2+} = REY^{3+} + F^{-}$$

Equation 3.0

Where □ represents an empty lattice site.

The chemical environments pertinent to the current work are the three potential sources of fluid from which carbonate minerals precipitated into veins in the Bermuda igneous units: hydrothermal fluid developed with magmatic fluids, hydrothermal fluids developed from seawater circulation, and ambient seawater.

Hydrothermal fluids are any fluid phase which is heated above ambient temperature (Sharma and Srivastava 2014). High-temperature (>250˚C) hydrothermal

fluids occur when a heat source outside of the typical geothermal gradient is present to increase the temperature of fluids, such as when a magma chamber occurs at depth below the fluid system (Figure 3) (Sharma and Srivastava 2014). High-temperature hydrothermal fluids can also undergo chemical changes as magmatic fluids mix with the convecting fluid (Figure 3) (Sharma and Srivastava 2014). Low-temperature (<200˚C) hydrothermal fluids occur when such a heat source is not present and increases in temperature are strictly due to convection of fluids through a geothermal gradient (Figure 3) (Sharma and Srivastava 2014). A chemical distinction between high-temperature and low-temperature hydrothermal fluids can be made as the REY patterns between them are different (Bau and Dulski 1999; Sharma and Srivastava 2014; Debruyne et al. 2016; Zhao et al 2021).

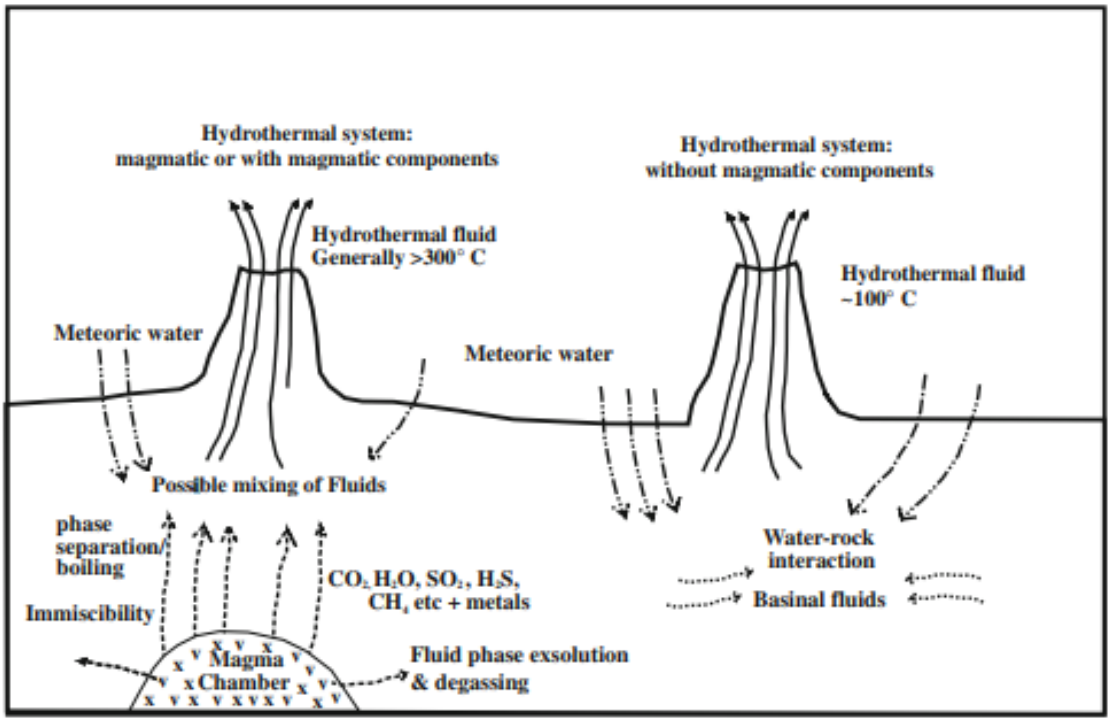

Figure 3 Differences in heat source and fluid influences between high-temperature hydrothermal fluids (left) and low-temperature hydrothermal fluids (right). From Sharma and Srivastava 2014.

The main difference in REY signature between the two types of hydrothermal fluid is in the magnitude of the positive Eu anomaly, with high-temperature hydrothermal fluids presenting a larger positive anomaly than low-temperature hydrothermal fluids (Figure 4)

(Zhao et al. 2021). This difference is caused by the higher solubility of Eu^{2+} at high temperature relative to Eu^{3+} and Eu's trivalent REY neighbours (Zhao et al. 2021). It is noted that for both high- and low-temperature hydrothermal fluids, the LREE/HREE ratio is ~1 (Zhao et al. 2021).

Both forms of hydrothermal fluids can also be distinguished from an ambient seawater REY signature. In seawater, LREE are depleted relative to HREE, high magnitude negative Ce anomalies are present, and moderately positive Y anomalies are present (Figure 4) (Zhao et al. 2021). The exact mechanisms behind the development of these REY characteristics in seawater are controversial, but are mostly due to differences in complexation with oceanic anions (Zhao et al. 2021).

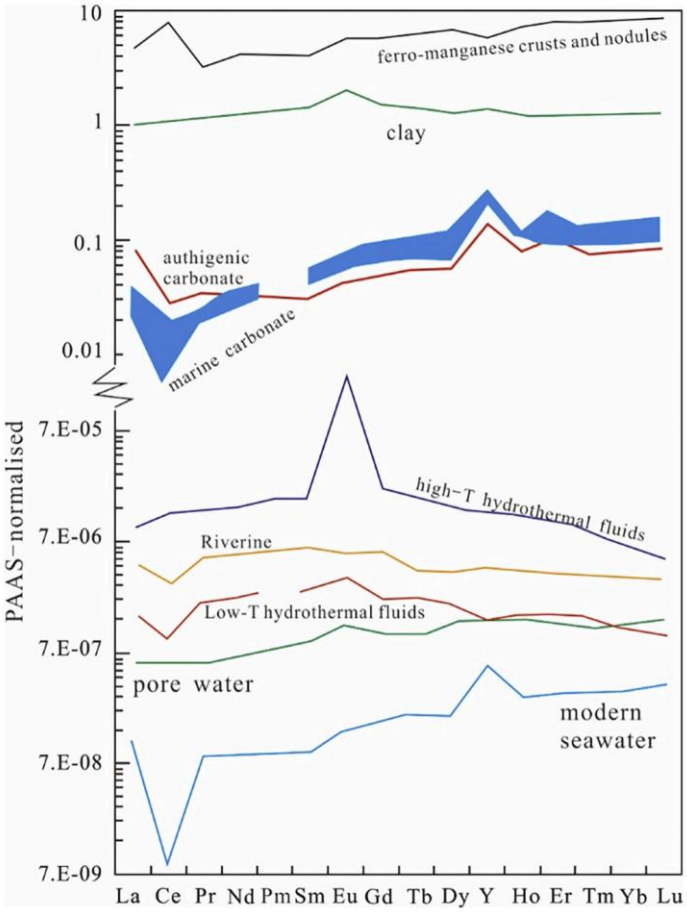

Figure 4 Representative REY trends of different sources for carbonate precipitation. The most relevant trends to the current work are those of high-T hydrothermal fluids (purple), low-T hydrothermal fluids (red), and modern seawater (blue). From Zhao et al. 2021.

1.5 Thesis Objectives

In this pilot study of the carbonate veining of the Bermuda igneous basement, we use optical microscopy and back-scatter imaging to provide detailed morphological and textural descriptions of vein minerals. Using major and trace element analyses, we narrow down the possible source regimes for the fluids which lead to precipitation of calcite within veins by comparing the REY trends and anomalies between the calcite in different veins. We aim to determine the mode of vein formation, the mineralogy of veins, whether or not the veins are chemically zoned, and to narrow down the source of the fluid from which vein minerals precipitated.

Chapter 2: Methods

2.1 Sample Selection

Samples were chosen from locations where the veins were of adequate thickness for optical microscopy and with clear relations to their host rock. Once chosen the core was split longitudinally at the sample location to ensure proper maintenance of the full core record; one half for sampling, the other half to remain in the record. A tile saw in the Dalhousie Crystal Extraction Lab was used to extract target locations and produce rock chips for thin section and epoxy mounting. Thin sections were produced at Acadia University Petrographic Lab (Wolfville, Nova Scotia (NS)). Thin sections are ¬40µm thick with a simple glass backing. Epoxy mounts were produced in the Dalhousie University Sample Prep Lab (Halifax, NS), progressively polished to 1µm fineness.

2.2 Laboratory Methods

Optical microscopy was performed using a Nikon LV-UEPI petrographic microscope at Dalhousie University. Plane polarized and cross polarized light were used to identify phases, grain-scale textures, and growth morphologies in veins.

Scanning Electron Microscopy (SEM) was performed using a TESCAN Mira3 LMU at the Saint Mary's University Electron Microscopy Centre (Halifax, NS), equipped with an Oxford Instrument INCA X-max 80mm^2 energy-dispersive X-Ray spectrometer (EDS) system. INCA internal software was used for data collection. SEM work included back-scattered electron (BSE) imaging and EDS analysis to identify phases and microtextures relating to mineral intergrowth and interstitial material.

Electron Microprobe (EMP) work was performed using a JEOL JXA-8200 at the Robert M. MacKay Electron Microprobe Lab at Dalhousie University. This EMP is equipped with five wavelength-dispersive X-ray spectrometers (WDS) and a single EDS. Analyses were performed using a voltage of 15 kv, amperage of 20nA, and beam size of 1µm. Both JEOL internal software and *Probe for EMPA*™ external software were employed for data collection. All analyses employed ZAF corrections. Analysed elements for all samples are: Mg, Al, Si, S, Ca, V, Mn, Fe, Sr, Ba, Pb. All analyses were spot analyses and are reported as % oxides, later converted to ppm for comparison with REYs.

Calcite, dolomite, quartz, and celestine standards were interspersed with analytical analyses, roughly every 15 spots.

Trace element analyses were performed at the Dalhousie Laser Ablation Inductively Coupled Mass Spectrometry (LA-ICP-MS) Laboratory, using an ESI NWR213 laser ablation instrument coupled to a Thermo iCAP Q quadrupole mass spectrometer. QTEGRA 2.1 software was used for data collection. Since calcite is readily ablated, analyses were performed as linescans to minimize slide damage and allow for longer ablation time. Analyses used spot sizes of 100 μm, and ablated at 5-7 Hz with 20% total energy. Run times ranged from 103 s to 141 s (average = 124, n = 28), with an additional 20 s laser warm-up and 60s He-gas flush, resulting in 183 s to 221 s total time per analysis. Variation in total run time is due to variation in ablation time according to calcite crystal size and thus linescan length. A total of 10 NIST 610 and 3 FAP standard analyses were interspersed with analytical runs. Analysed isotopes for all samples are: ^{24}Mg, ^{29}Si, ^{32}S, ^{43}Ca, ^{44}Ca, ^{55}Mn, ^{57}Fe, ^{66}Zn, ^{88}Sr, ^{89}Y, ^{137}Ba, ^{139}La, ^{140}Ce, ^{141}Pr, ^{145}Pm, ^{146}Nd, ^{147}Sm, ^{153}Eu, ^{157}Gd, ^{159}Tb, ^{163}Dy, ^{165}Ho, ^{166}Er, ^{169}Tm, ^{172}Yb, ^{175}Lu, ^{206}Pb, ^{208}Pb, ^{232}Th, and ^{238}U. Data reduction was performed using iolite4 software (Paton et al. 2011). Base levels were determined visually with ^{29}Si, ^{43}Ca, and ^{88}Sr peaks to avoid anomalous intensities.

Chapter 3: Results

3.1 Sample Suitability Assessment

A total of 19 samples (13 thin sections, and 6 epoxy pucks) were prepared (Table 1). Samples were named according to their core box and depth in the format of "XXX.YYYY", where XXX is the core box number and YYYY is the depth in feet. Where multiple samples were taken from the same core box and depth, suffix modifiers of "A" and "B" are used to distinguish between each sample. For example, sample "123.2396B" is from core box 123, corresponds to a depth of 2396', and is the second sample taken from the same box and depth combination. Screening of samples for geochemical analysis suitability was performed via optical microscopy and SEM work. Samples determined to have high quality polish, sufficiently large vein phases, minimal alteration, and clear vein relationships (e.g., no crosscutting veins which may interfere with chemical signatures) were selected to be the geochemical analysis samples; ultimately samples 62.1207, 72.1387, 113.2202.1, 123.2396A, and 123.2409 were selected for geochemical analysis (Table 1).

Table 1 Summary of names, locations, and techniques used for all samples developed for study of calcites in veining found in the Deep Drill 1972 core of Bermuda Islands. Samples in bold are those which were chosen for detailed geochemical study.

Sample Name (thin sections)	Sample Depth (m)	Optical Descriptions	EMP Trace Element Analysis (WDS)	LA-ICP-MS Trace Element and REY Analysis
14.313	95.40	✓		
29.599	182.58	✓		
47.924	281.64	✓		
62.1204.4	367.10	✓		
62.1207	**367.90**	✓	✓	✓
113.2200.5	670.71	✓		
113.2202.1	**670.86**	✓	✓	✓
123.2393	729.39	✓		
123.2396A	**730.30**	✓	✓	✓
123.2396B	730.30	✓		
123.2400	731.52	✓		
123.2409	**734.26**	✓	✓	✓

Sample Name (epoxy pucks)	Sample Depth (ft)	Optical Descriptions	EMP Trace Element Analysis (WDS)	LA-ICP-MS Trace Element and REY Analysis
62.1207A	367.89			
62.1207B	367.89			
72.1387	**422.76**	**limited**	✓	✓
72.1390	423.67			
72.1398	426.11			
113.2200.5	670.71			

3.2 Morphological and Phase Descriptions

Morphological and phase descriptions of samples are based on optical microscopy, BSE imaging, and EDS spectra for phase identification. Such descriptions were produced for all thin sections. The epoxy puck samples had poor quality polish and did not receive sufficient BSE imaging to make definitive morphological conclusions, therefore the only epoxy sample with limited morphological description is 72.1387.

All analyzed veins are hosted by the mafic units of the core. The dominant phase in most veins is calcite. Almost all veins display blocky calcites, with only a single analyzed vein displaying evidence of a stretched crystal shape (a small vein within sample 123.2409). Some quartz-dominated veins are present (e.g., sample 62.1207) and are blocky to elongate blocky in shape, but quartz mostly occurs as an anhedral, interstitial material in calcite-dominated veins. Frequent accessory phases are pyrite and magnetite, with rare anhydrite. Pyrite and magnetite are usually euhedral. Large, euhedral anhydrite occurs in sample 123.2396A. An unknown silicate with cation proportions of 2Si:Al:Fe:Mg is usually present at vein edges, although sometimes also occurs centrally within veins; henceforth this phase is simply called “the FeMg silicate”. Samples are described below in order of increasing depth.

Sample 14.313

Sample 14.313 has two very small veins (maximum width = 0.3mm) which intersect at a sharp angle (Figure 5). Both veins are mainly calcite, with fine interstitial crystals (several µm diameter) of the FeMg silicate identified through EDS. Due to the very fine crystal size it is sometimes difficult to identify crystal shape, but the majority of visible crystals are blocky (Figure 6). Calcite appear largely unaltered, although some unknown alteration minerals occur immediately adjacent to the host rock (Figure 6).

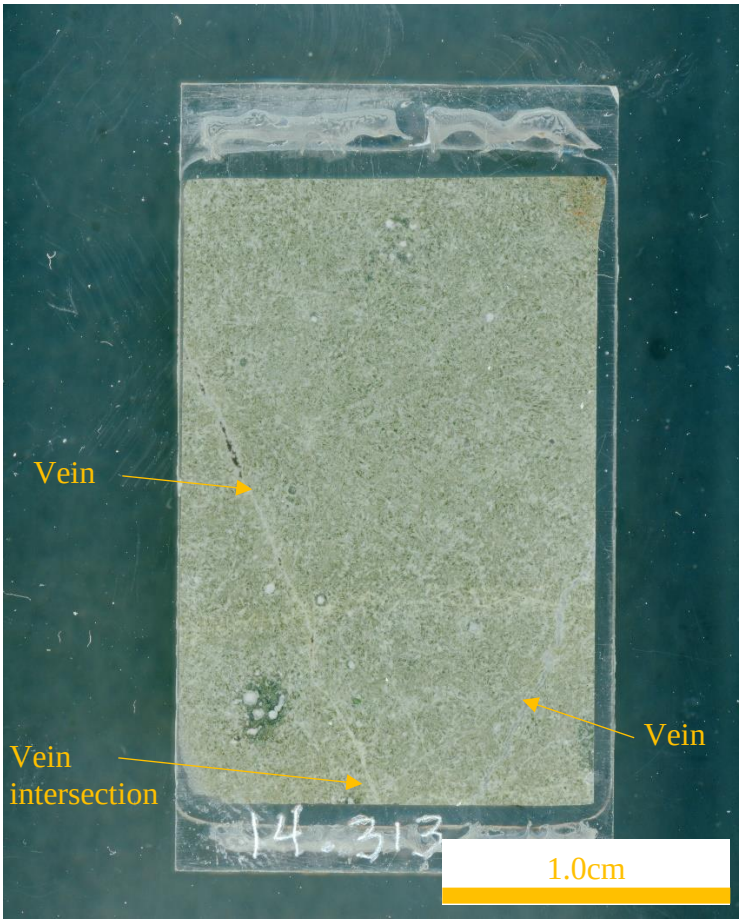

Figure 5 Thin section scan of sample 14.313. Two veins are present in this sample which intersect at a high angle.

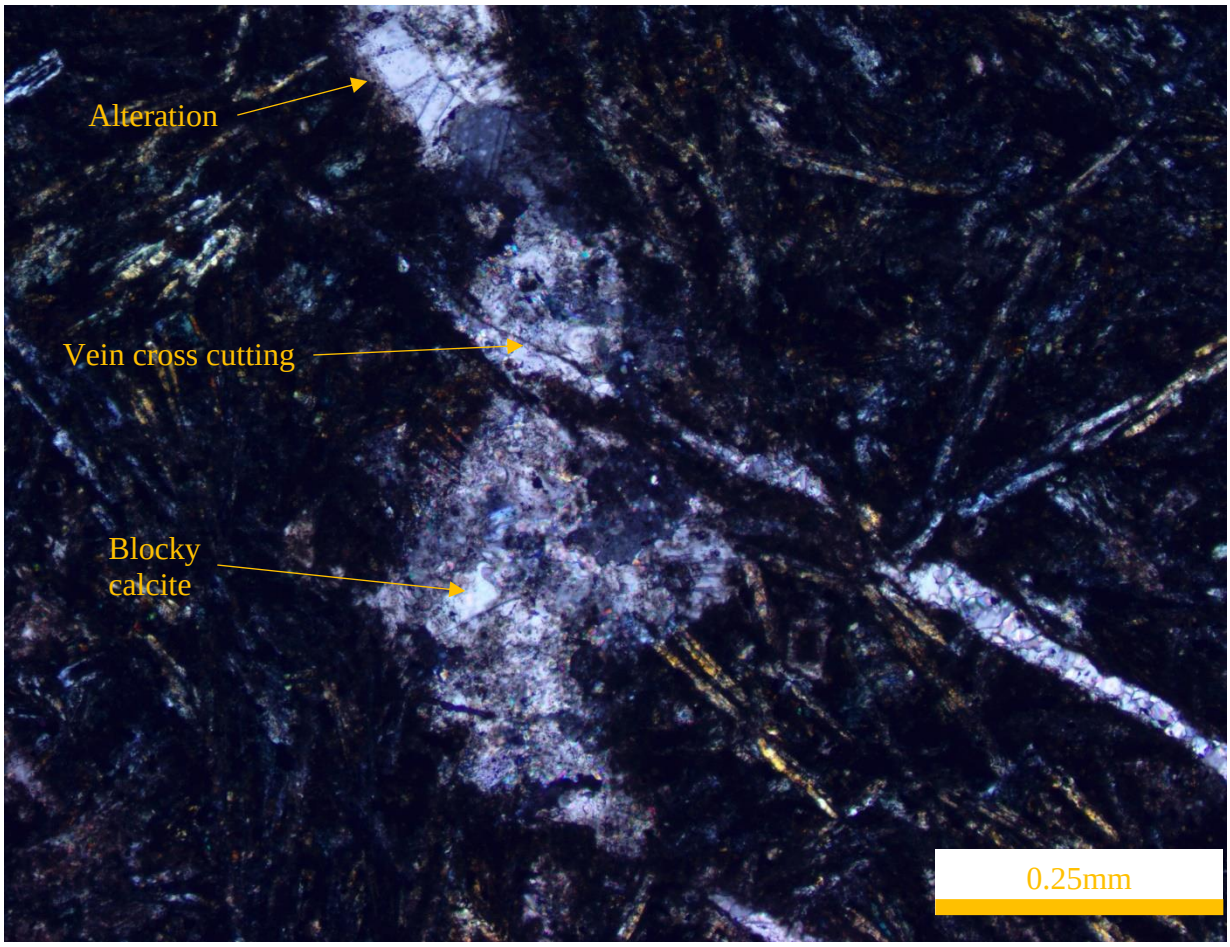

Figure 6 Cross polarized light microphotograph of sample 14.313. Calcite is the dominant phase with miniscule, interstitial crystals of an unknown silicate phase identified through EDS. The two veins present in this sample intersect at high angle.

Sample 29.599

The most altered sample, all vein edges within sample 29.599 present severe alteration and a dark brown, glassy, altered host rock (Figure 7; Figure 8). The precise number of veins present in this sample is unclear as numerous cross-cutting relationships exist (Figure 8). Separate veins within the sample are often deformed (Figure 8). Veins are dominantly calcite, but quartz, titanite, and the FeMg silicate were also identified through EDS. Vein calcite is blocky, with all other vein minerals being anhedral (Figure 8). Amygdules are also present in this sample, occasionally contacting veins (Figure 7; Figure 8). Amygdules contain calcite, quartz, and titanite. Amygdule minerals are all anhedral. Issues of polish quality are noted in this sample causing a speckled appearance in vein minerals (Figure 8).

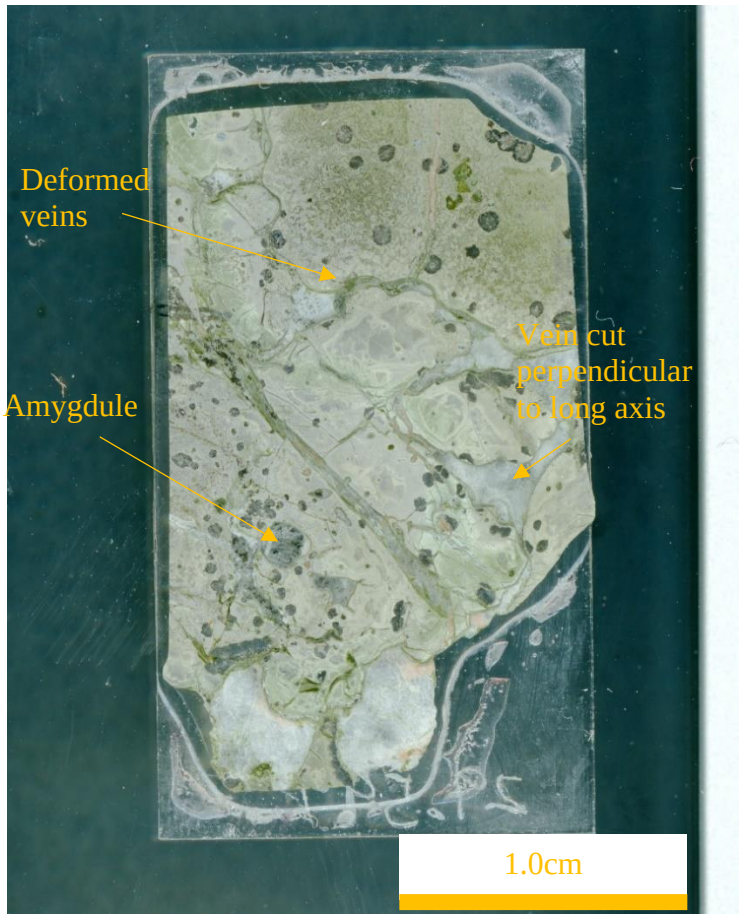

Figure 7 Thin section scan of sample 29.599. Numerous veins are present, but the precise number is unclear due to complex cross-cutting and deformational relationships.

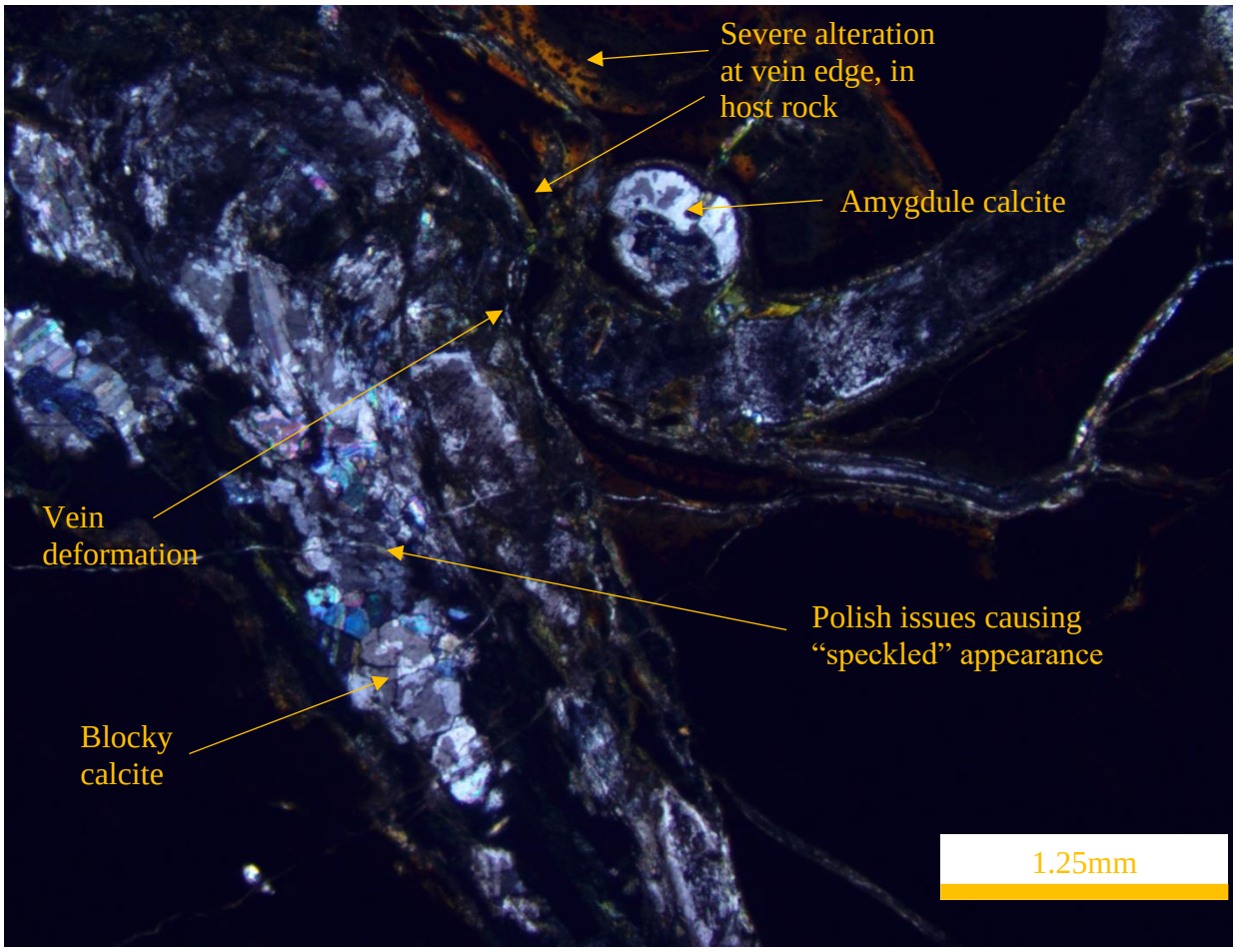

Figure 8 Cross polarized light microphotograph of Sample 29.599. Veins are dominantly blocky calcite, with occasional quartz, titanite, and an unknown silicate. Amygdules contain anhedral calcite, quartz, and titanite.

Sample 47.924

Due to oblique sectioning of sample 47.924, the continuity of the vein is not clear in thin section (Figure 9). Sample 47.924 contains a single main vein with large blocky calcite visible in thin section, with interstitial quartz identified via EDS (Figure 10). Small secondary veins with blocky calcite crosscut the main vein (Figure 10). This sample appears minimally altered.

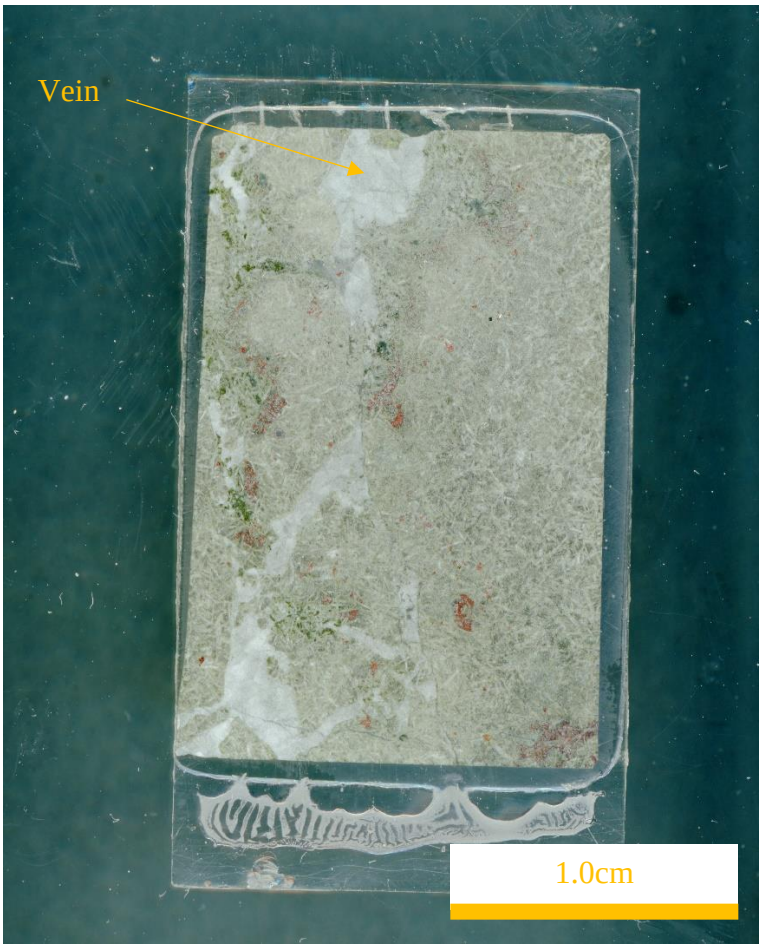

Figure 9 Thin section scan of sample 47.924. Although not clear in thin section, the main vein of this sample is continuous.

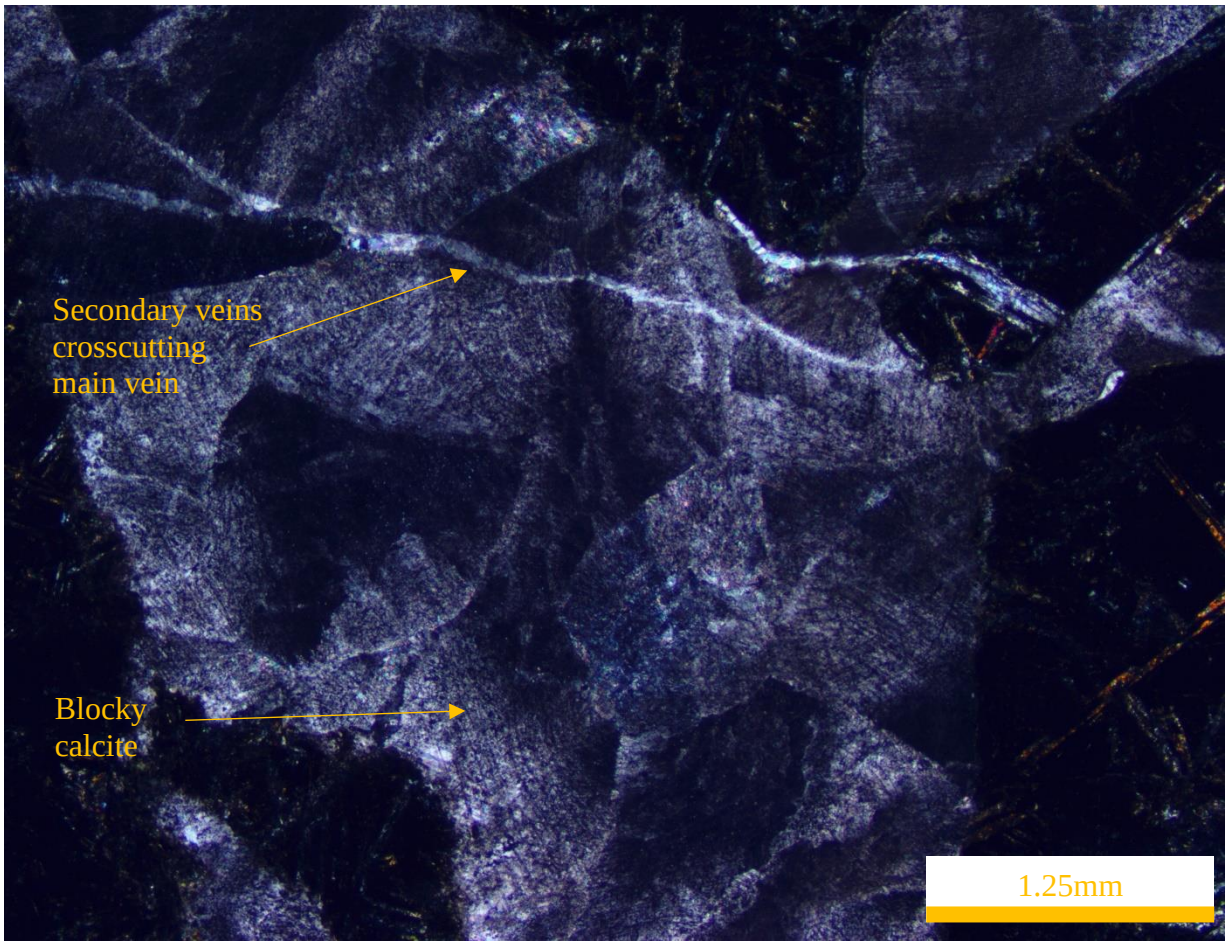

Figure 10 Cross polarized light microphotograph of sample 47.924. This sample has one main vein with smaller secondary veins crosscutting it. Both the main and secondary veins contain blocky calcite. Interstitial quartz was identified in the main vein via EDS.

Sample 62.1204.4

Sample 62.1204.4 has four veins of mainly blocky calcite, with repeating bands of calcite followed by host rock inclusions spanning the vein width (Figure 11; Figure 12). Accessory pyrite is also present in these four veins. A fifth vein, which is cut perpendicular to its long axis, has both blocky calcite and quartz (Figure 11). Amygdules of calcite and quartz are also present throughout the host rock (Figure 11; Figure 12).

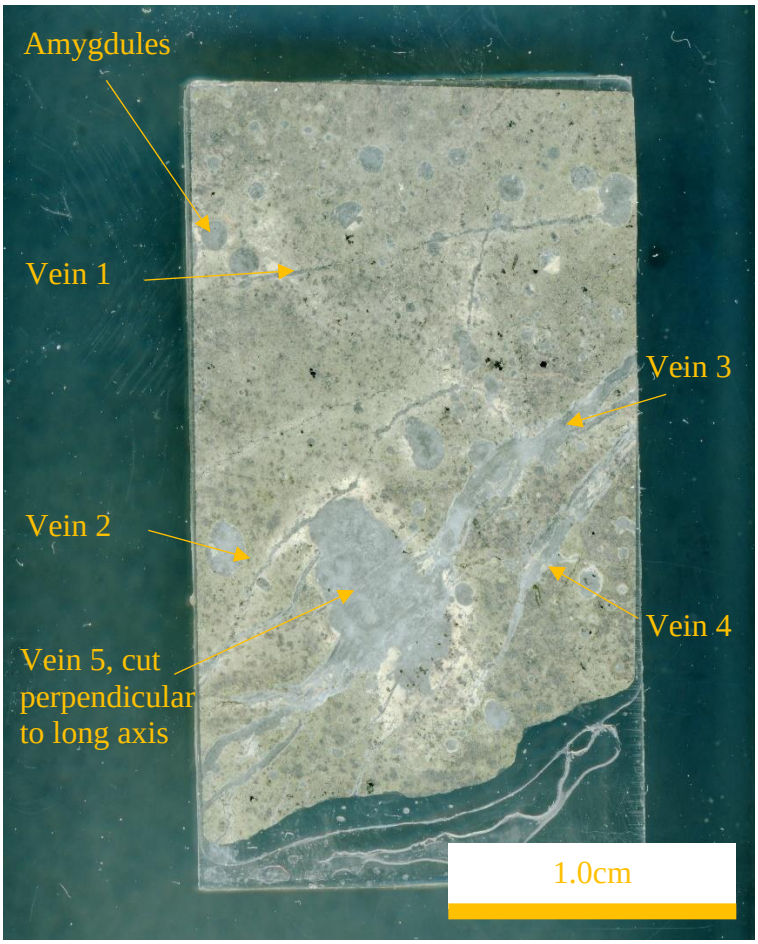

Figure 11 Thin section scan of sample 62.1204.4. Veins 1 through 4 contain alternating bands of calcite and host rock inclusions. Vein 5 is cut perpendicular to its long axis and presents blocky calcite and quartz. Amygdules are present throughout the sample, and contain calcite and quartz.

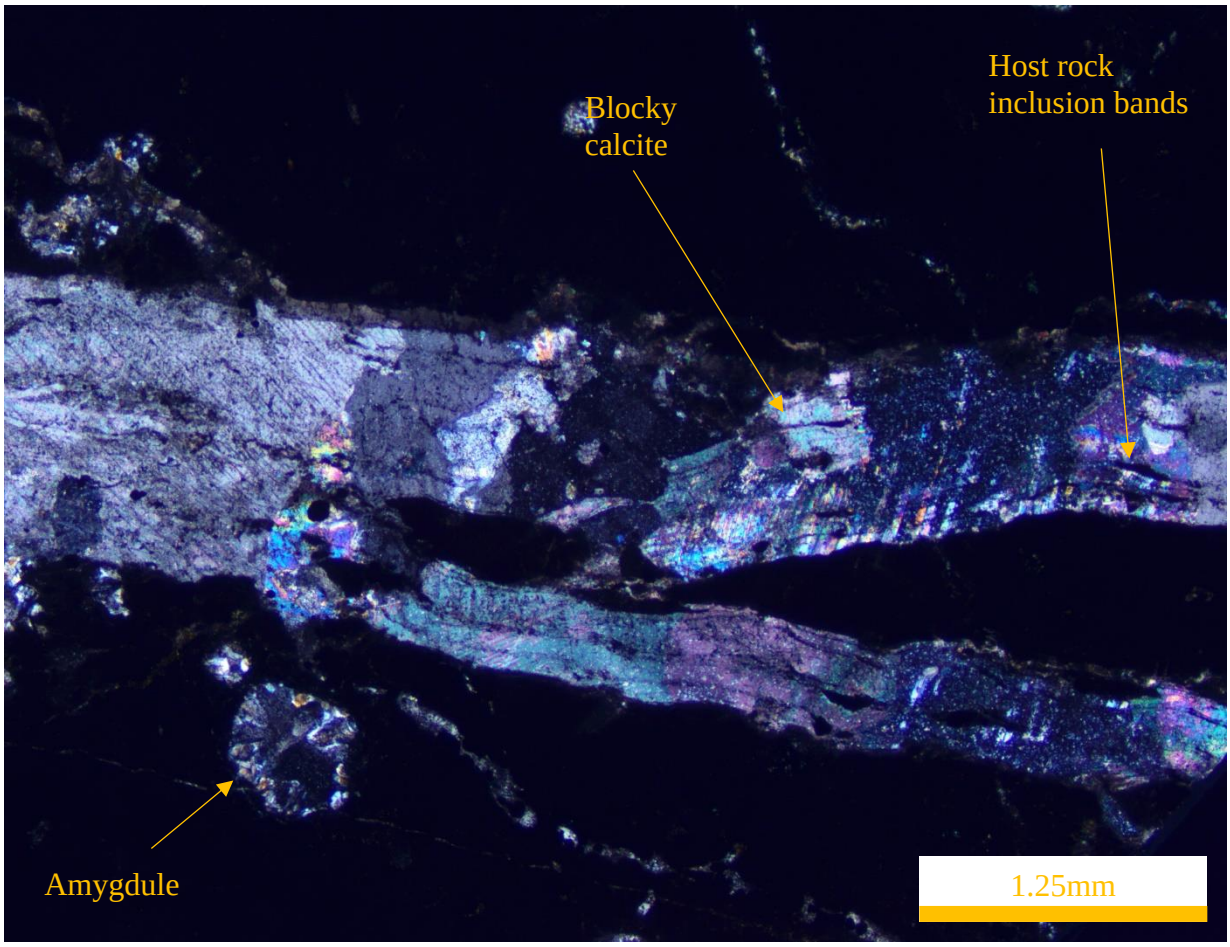

Figure 12 Cross polarized light microphotograph of sample 62.1204.4. Four veins in this sample present repeating bands of blocky calcite and host rock inclusions. Amygdules are also present and contain calcite and quartz.

Sample 62.1207

Sample 62.1207 has numerous veins, which are either exclusively calcite or a mixture of both calcite and quartz (Figure 13). Accessory pyrite is present in all veins. Vein calcite are always blocky, with quartz variously being blocky or elongate blocky (Figure 14). The FeMg silicate is present near vein edges in some cases, particularly where calcite and quartz occur together (Figure 14).

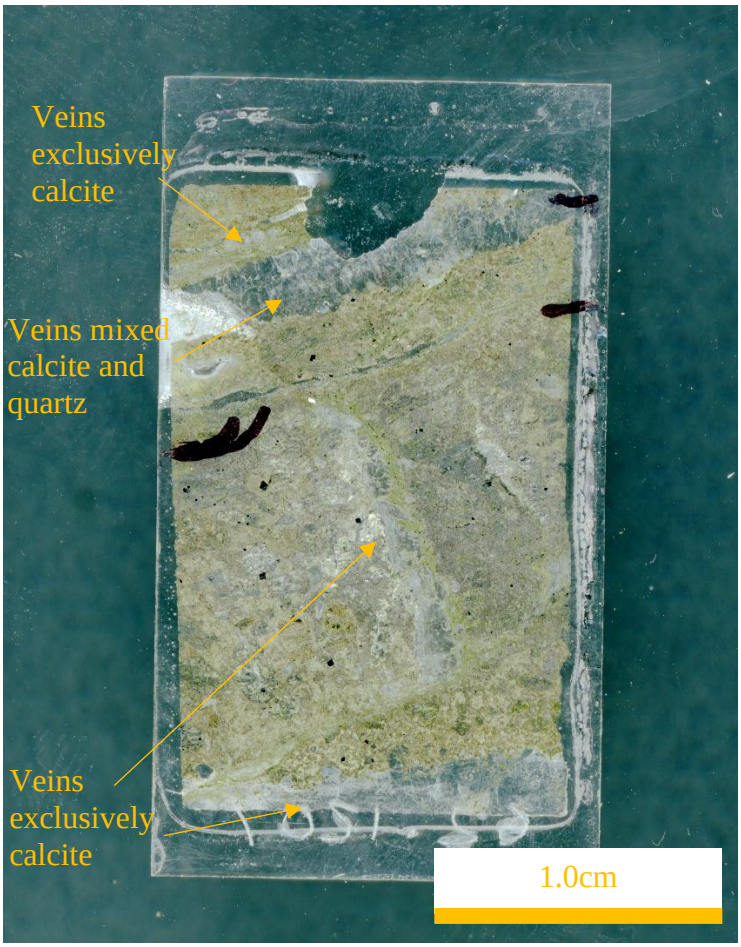

Figure 13 Thin section scan of sample 62.1207. Numerous veins are captured by this sample which can either be exclusively calcite or a mixture of calcite and quartz.

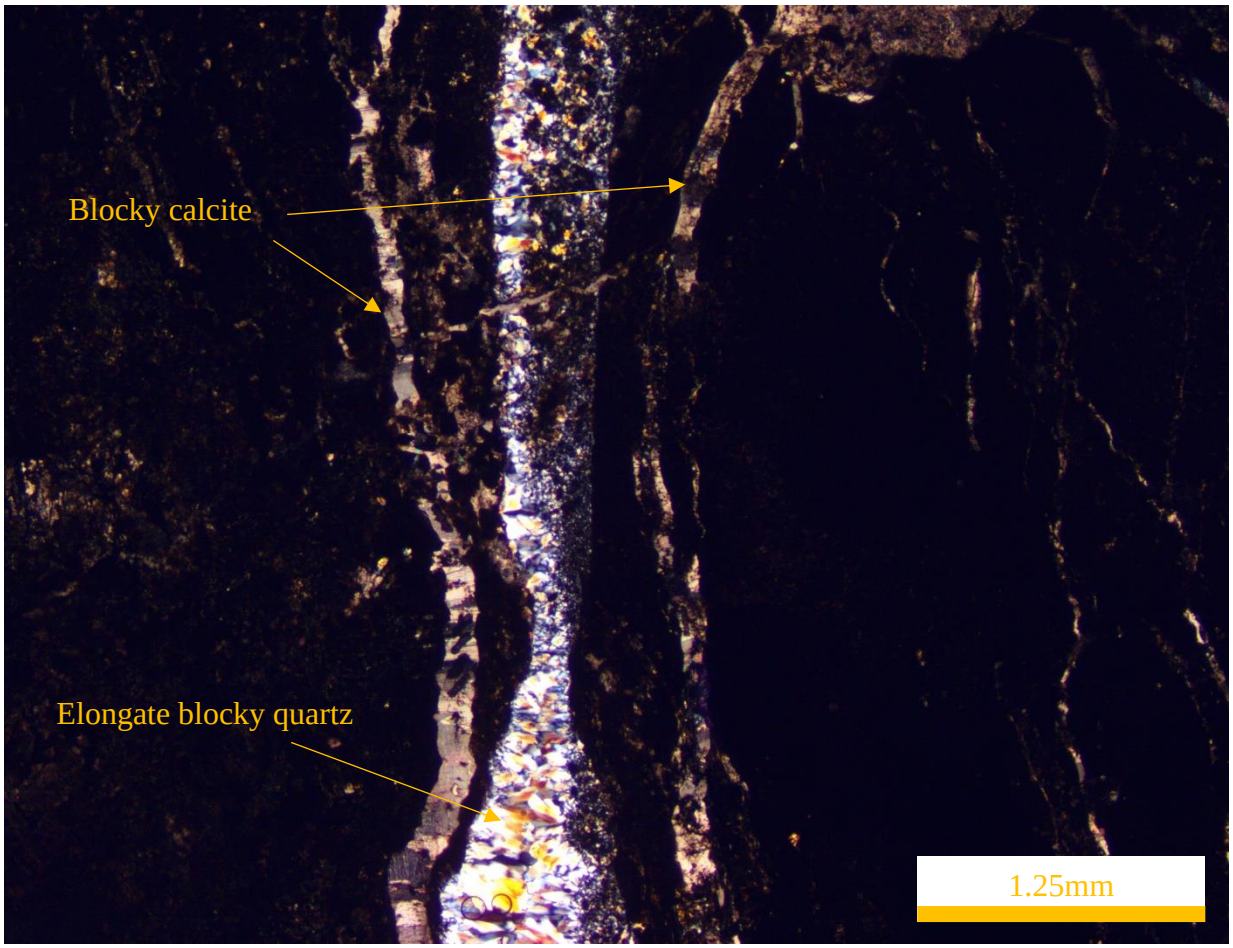

Figure 14 Cross polarized light microphotograph of sample 62.1207. This vein is mixed-phase, with blocky calcite forming on either side of central elongate blocky quartz.

Sample 72.1387

Sample 72.1387 is an epoxy puck-mounted rock chip sample that displays two veins which intersect at near-right angles to form a cross (Figure 15). One vein is entirely blocky calcite and the other is mixed-phase with blocky quartz, anhedral calcite, anhedral Fe-rich dolomite, and the FeMg silicate (Figure 15). This is the only occurrence of a dolomite found in any sample.

Figure 15 Epoxy mount scan of sample 72.1387. Two veins are present, one of which is entirely calcite and which cuts through a mixed vein with calcite, Fe-rich dolomite, and quartz.

Sample 113.2200.5

There are numerous large host rock inclusions within the vein of sample 113.2200.5, typically with alteration haloes (Figure 16; Figure 17). Sample 113.2200.5 contains a single large vein of primarily blocky calcite with occasional interstitial, anhedral quartz and rare magnetite (Figure 17). The sample is moderately altered.

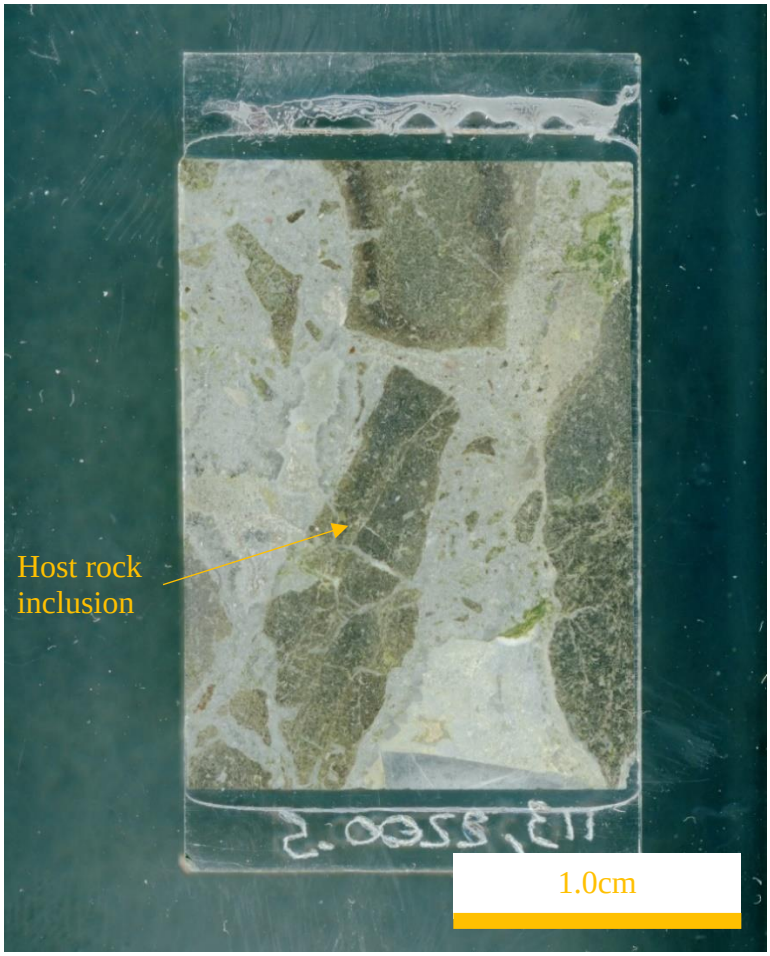

Figure 16 Thin section scan of sample 113.2200.5. A single large vein is present which is constituted of blocky quartz, occasional interstitial quartz, and rare magnetite. Large host rock inclusions are abundant.

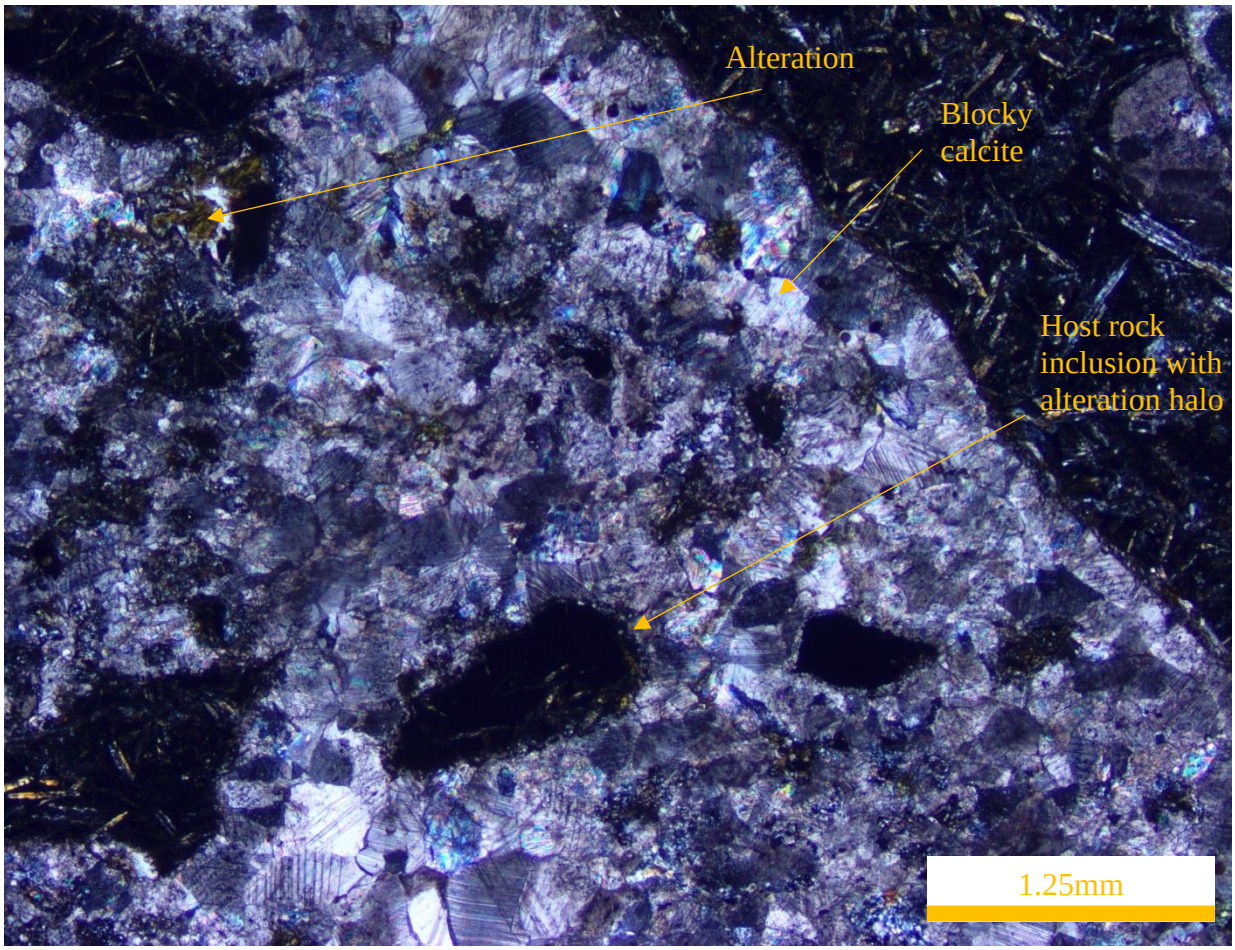

Figure 17 Cross polarized light microphotograph of sample 113.2200.5. This large vein is mostly blocky quartz, with occasional interstitial quartz and rare magnetite. Host rock inclusions are frequent and tend to have alteration haloes.

Sample 113.2202.1

A single dominant vein spans the length of the thin section of sample 113.2202.1 (Figure 18). This vein shows a change in both texture and composition along the length of the vein (Figure 18; Figure 19). One side the vein is entirely blocky calcite with some interstitial, anhedral quartz (Figure 19). The vein evolves texturally into a two-domain vein. One domain continues to be nearly exclusively blocky calcite and the other presents a "dirty" texture of mixed phase composition, with anhedral quartz and calcite, along with bands of accessory pyrite and rare magnetite (Figure 19).

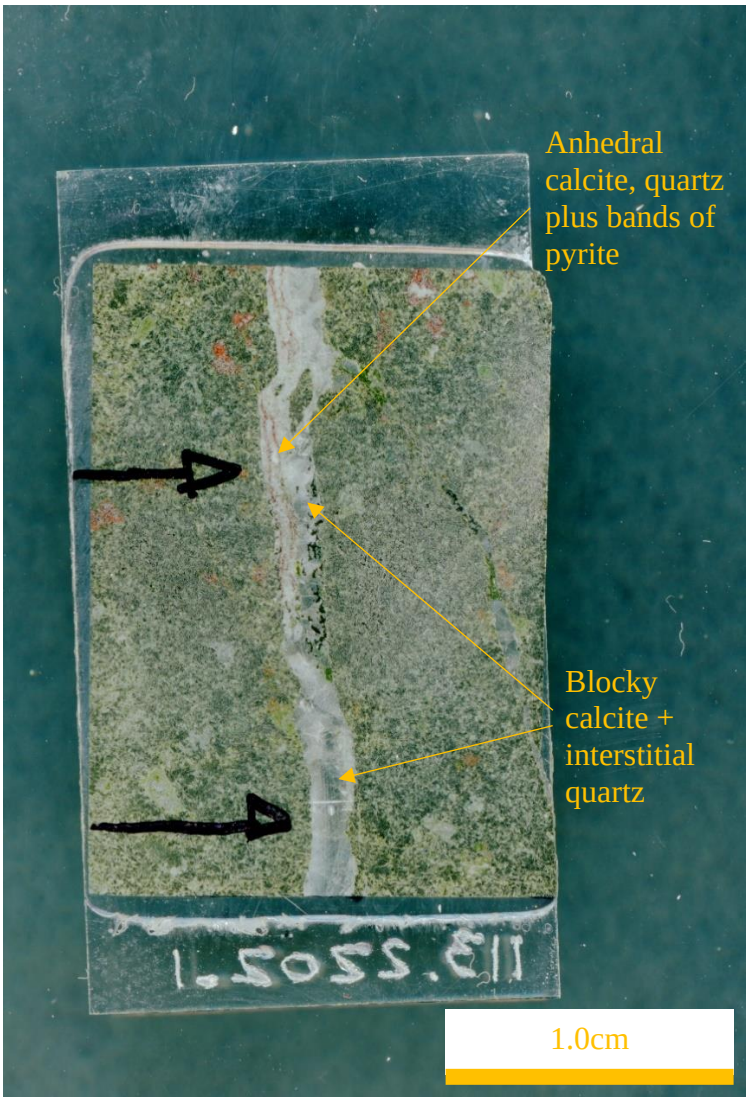

Figure 18 Thin section scan of sample 113.2202.1. This sample shows a lateral evolution from entirely blocky calcite + interstitial quartz (toward bottom of sample) to a region with a domain of blocky calcite + interstitial and a domain of mixed anhedral calcite, quartz, and bands of pyrite (toward top of sample).

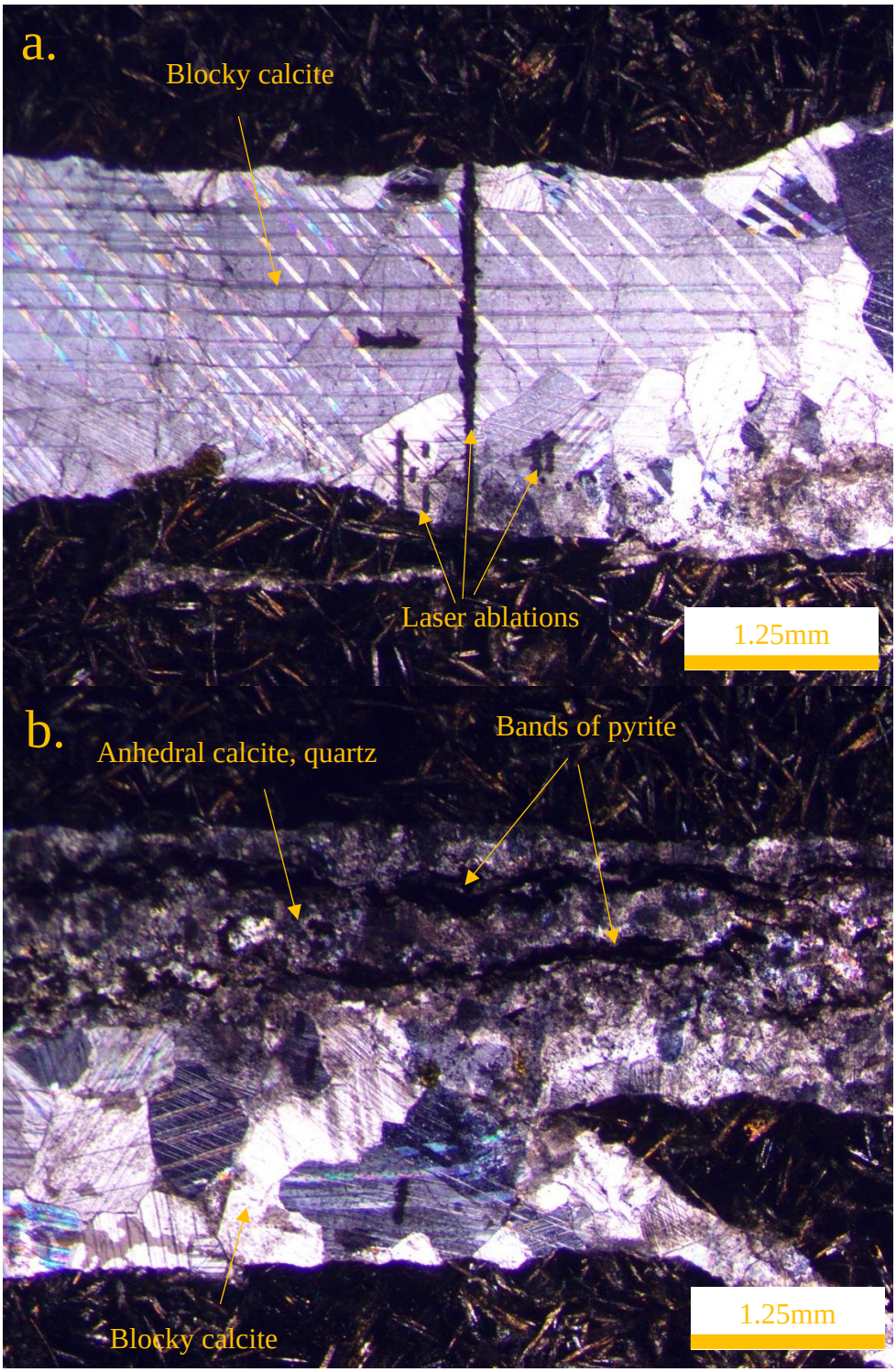

Figure 19 Cross polarized light microphotographs of sample 113.2202.1. One portion of the vein is entirely blocky calcite + interstitial quartz (a.) and the other portion of the vein which spans both domains of blocky calcite + interstitial quartz and mixed anhedral calcite, quartz, and bands of pyrite (b.)

Sample 123.2393

Sample 123.2393 contains a single main vein which is dominated by blocky calcite (Figure 20; Figure 21). Toward one side of this vein crystal size of the blocky calcites is significantly reduced and shows evidence of alteration (Figure 20; Figure 21). Rare occurrences of anhydrite and the FeMg silicate were identified during EDS work. Host rock inclusions are abundant in some regions of the vein (Figure 20). While this sample is interpreted as a single vein, there are some unclear cross-cutting and host rock inclusion relationships which obscure this interpretation somewhat (Figure 20).

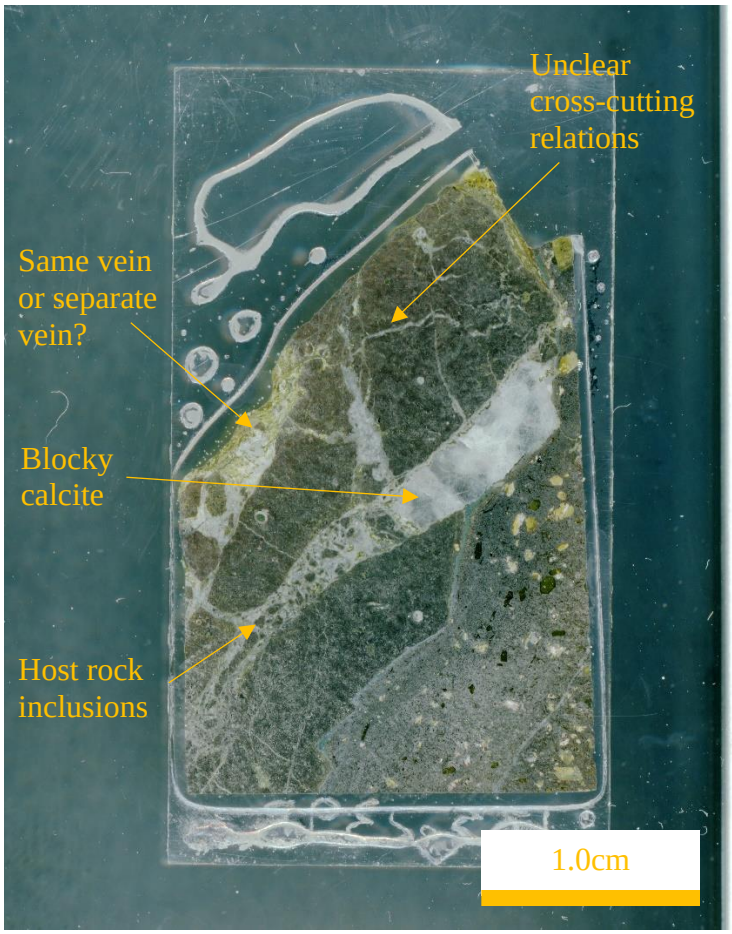

Figure 20 Thin section scan of sample 123.2393. This sample is interpreted to be a single vein, but there are several unclear relationships with host rock inclusions and potential cross-cutting veins which obscure this interpretation.

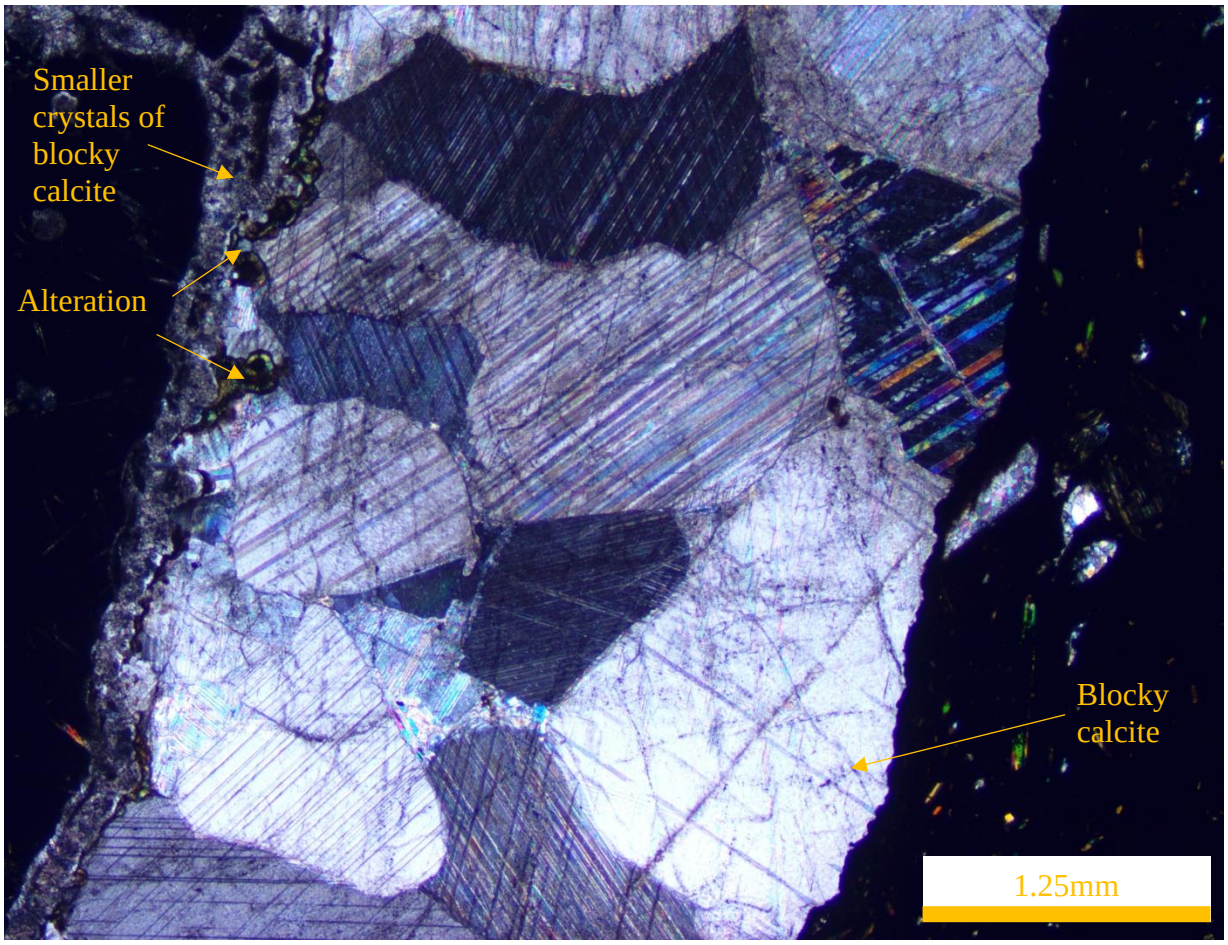

Figure 21 Cross polarized light microphotograph of sample 123.2393. This vein is dominated by blocky calcites, with much smaller crystals occurring to one side. Alteration occurs toward these smaller crystals.

Sample 123.2396A

The main vein present in sample 123.2396A contains small crystals of blocky calcite at the vein edges, with larger blocky calcite and an abundance of large anhydrite associated with anhedral quartz in the centre of the vein (Figure 22; Figure 23). The FeMg silicate forms a ~20µm band at the edges of the vein (Figure 35). Several other veins are visible in the thin section, but due to oblique sectioning the number and precise relationships between these veins is unclear (Figure 22).

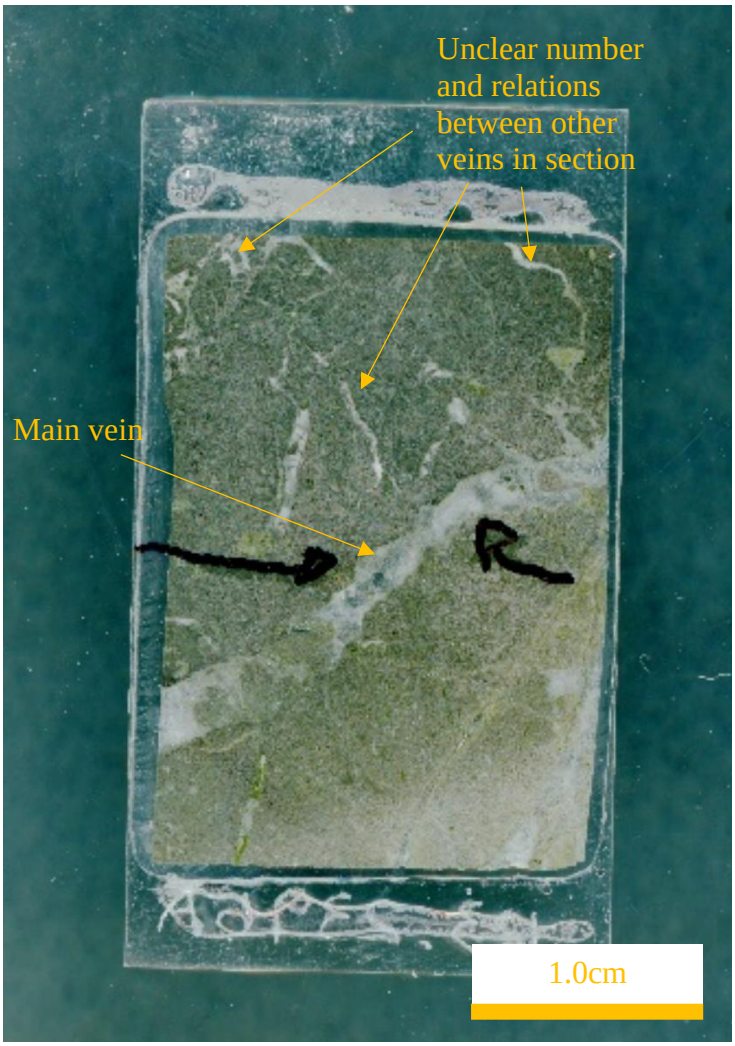

Figure 22 Thin section scan of sample 123.2396A. A single main vein is apparent in this sample, with multiple other veins present. The exact number and relationship between these other veins is unclear as they are obliquely sectioned.

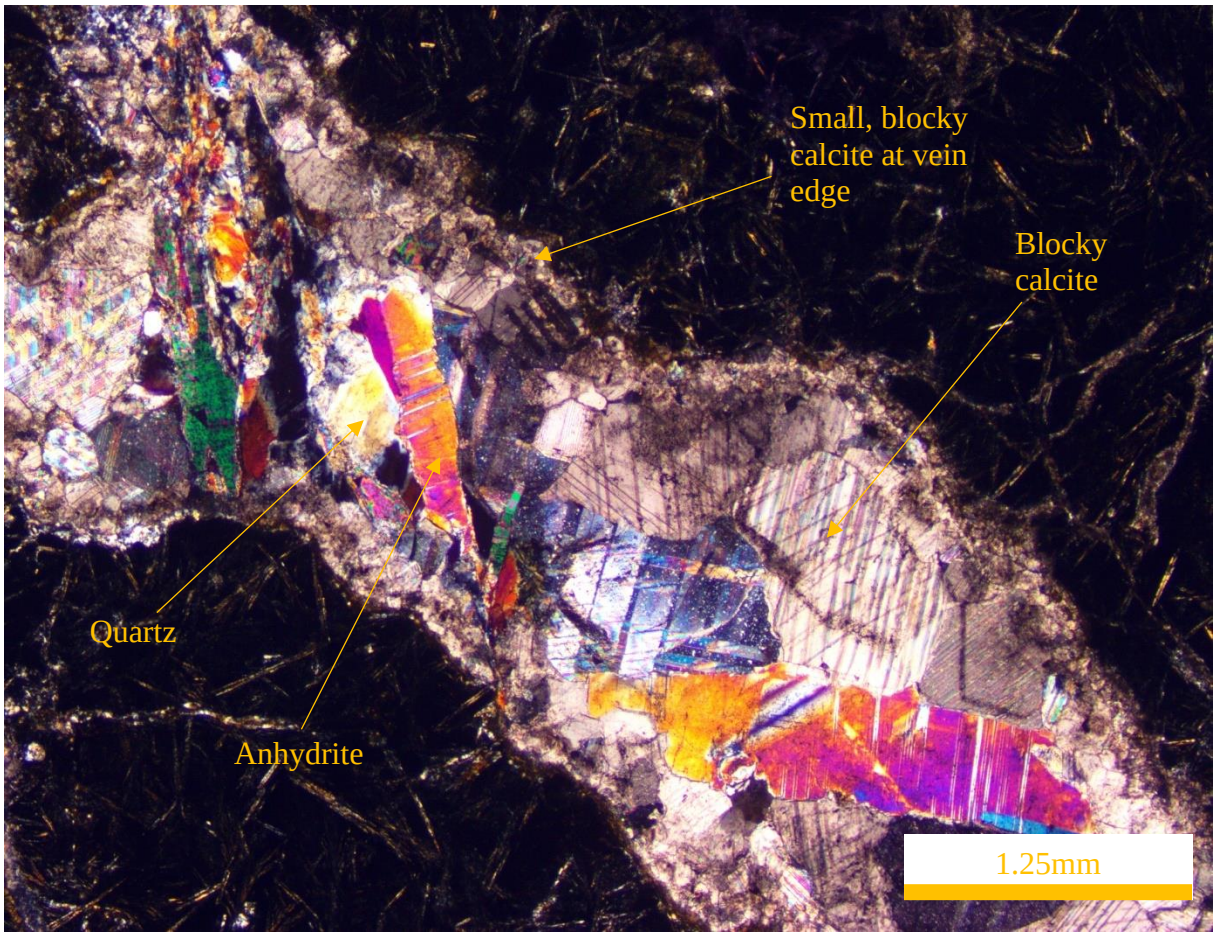

Figure 23 Cross polarized light microphotograph of sample 123.2396A. The main vein in this sample shows small crystals of blocky calcite at vein edges, with larger blocky calcite occurring toward the centre of the vein. The centre of the vein also contains anhydrite which occur as inclusions in anhedral quartz.

Sample 123.2396B

Sample 123.2396B contains a single vein which crosscuts two zones of carbonate breccia (Figure 24) This sample shows several zones of blocky calcite and alteration across its width (Figure 25). Zones of alteration appear on either side of bands of blocky calcite, with three distinct bands of calcite visible (Figure 25). Interstitial quartz and accessory pyrite are also present.

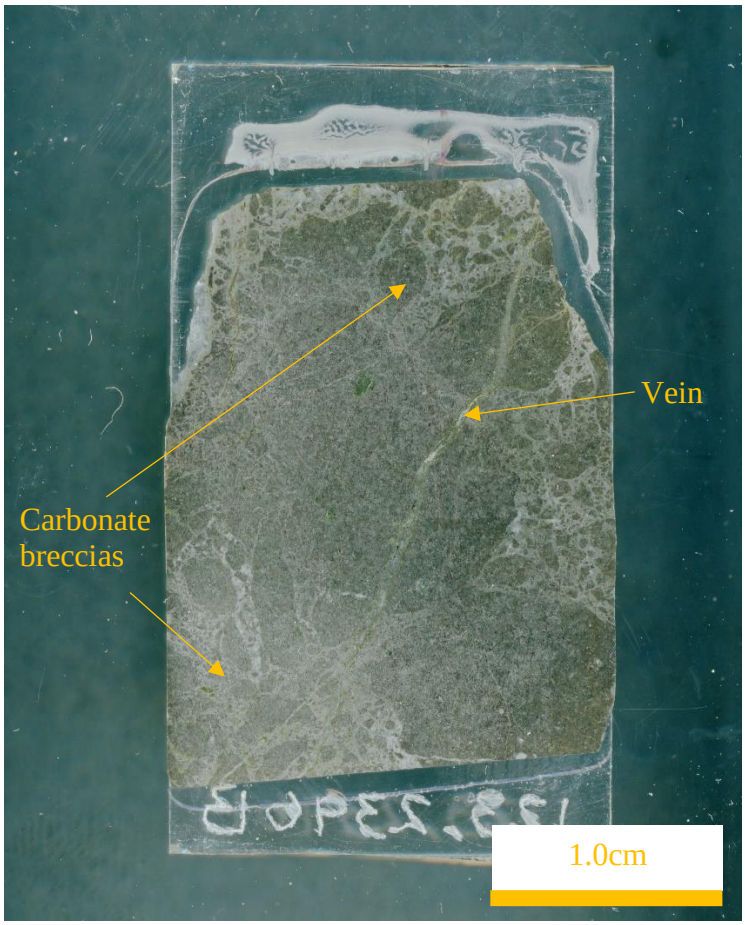

Figure 24 Thin section scan of sample 123.2396B. A single vein is present in this sample which crosscuts two regions of carbonate breccia.

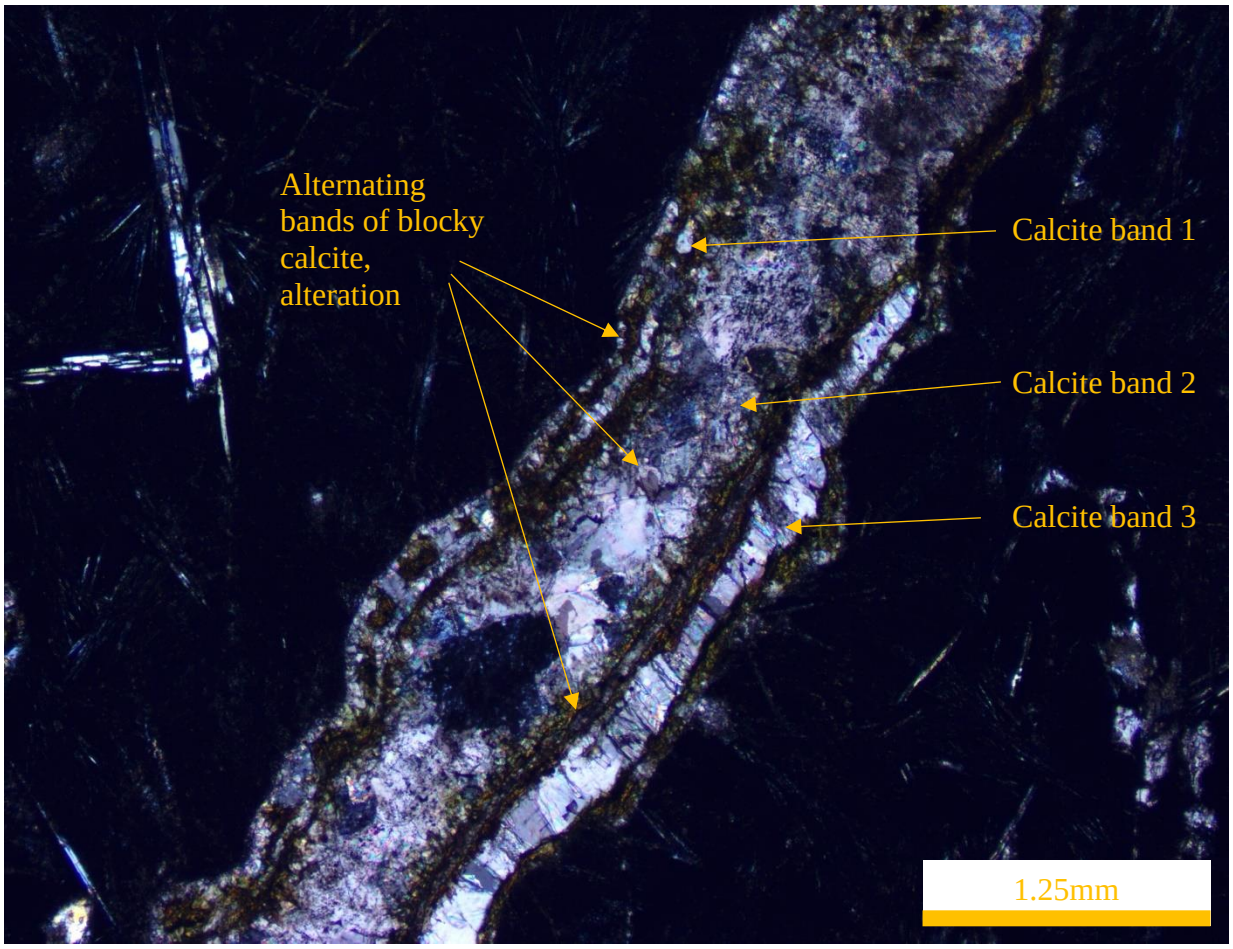

Figure 25 Cross polarized light microphotograph of sample 123.2396B. This vein has presents three alternating bands of calcite and alteration phases across its width.

Sample 123.2400

Four veins are present in sample 123.2400, with three smaller located at the top of the section and a larger, main vein beneath them (Figure 26). Amygdules are also present throughout the sample and contain calcite, but were not analysed for other phases (Figure 26). All veins are dominated by blocky calcite, with minimal interstitial quartz and very rare accessory magnetite (Figure 27). Smaller crystals of blocky calcite are present on one side of the main vein (Figure 27).

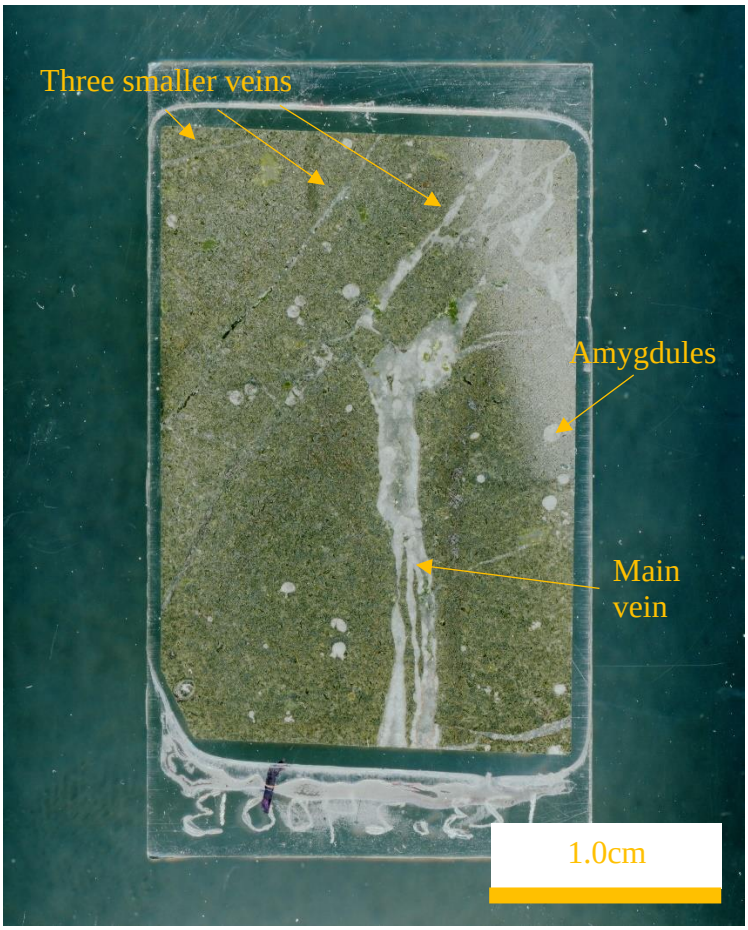

Figure 26 Thin section scan of sample 123.2400. The main vein contains blocky calcite and interstitial quartz, with rare magnetite. The three smaller veins contain similar phase relationships as the main vein. Amygdules contain calcite but were not analyzed for other phases.

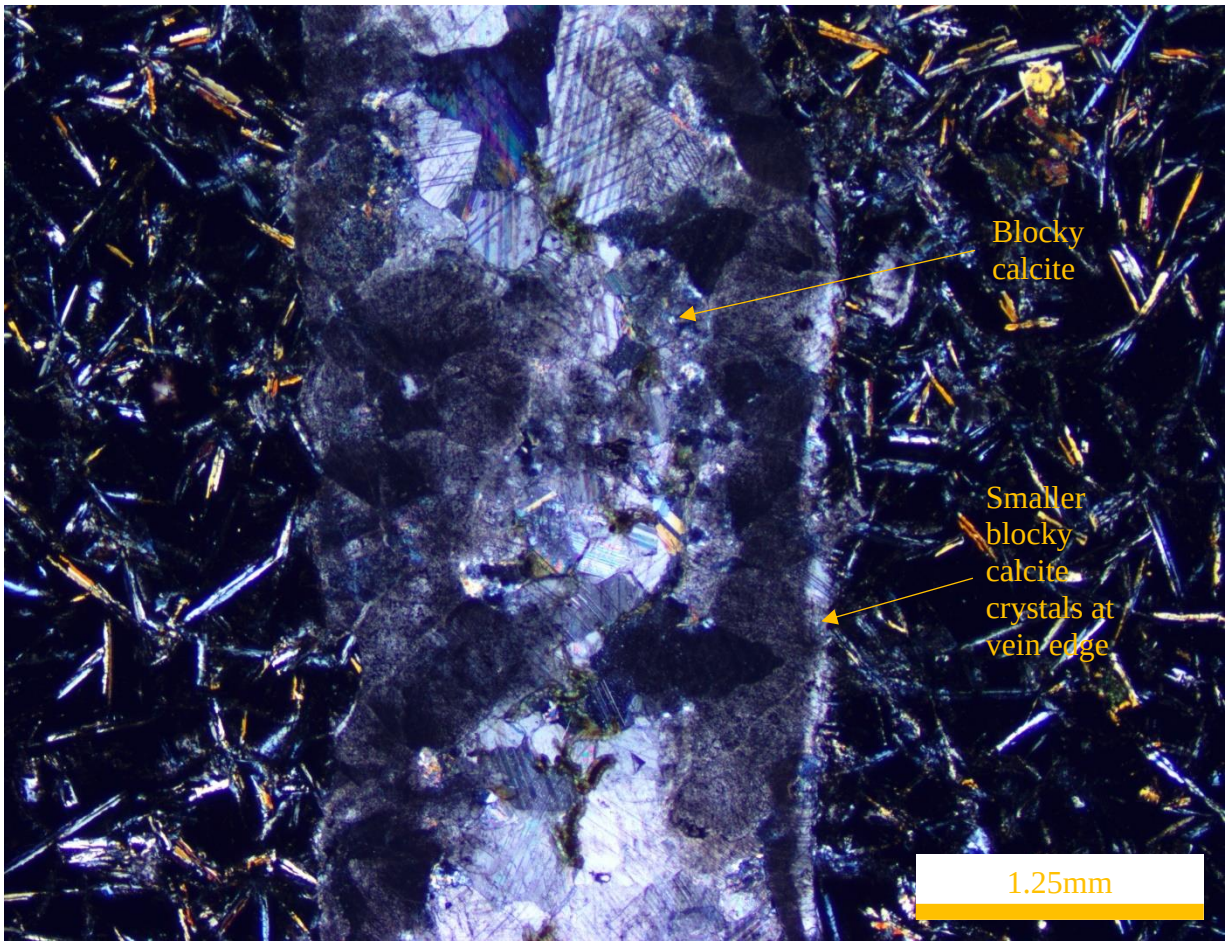

Figure 27 Cross polarized light microphotograph of sample 123.2400. The vein is almost entirely blocky calcite, with smaller blocky calcites occurring to one side of the vein. Interstitial quartz and rare magnetite are also present.

Sample 123.2409

One large, main vein which contains blocky calcite, interstitial quartz, and abundant host rock inclusions is present in sample 123.2409(Figure 28; Figure 29). Blocky calcite appear to occur in bands, variously separated by host rock inclusions or smaller blocky calcite (Figure 29). A second smaller, subsidiary vein occurs adjacent to the main vein and presents elongate blocky to stretched calcite (Figure 28; Figure 29). Carbonate breccia occurs at the bottom of the section (Figure 28).

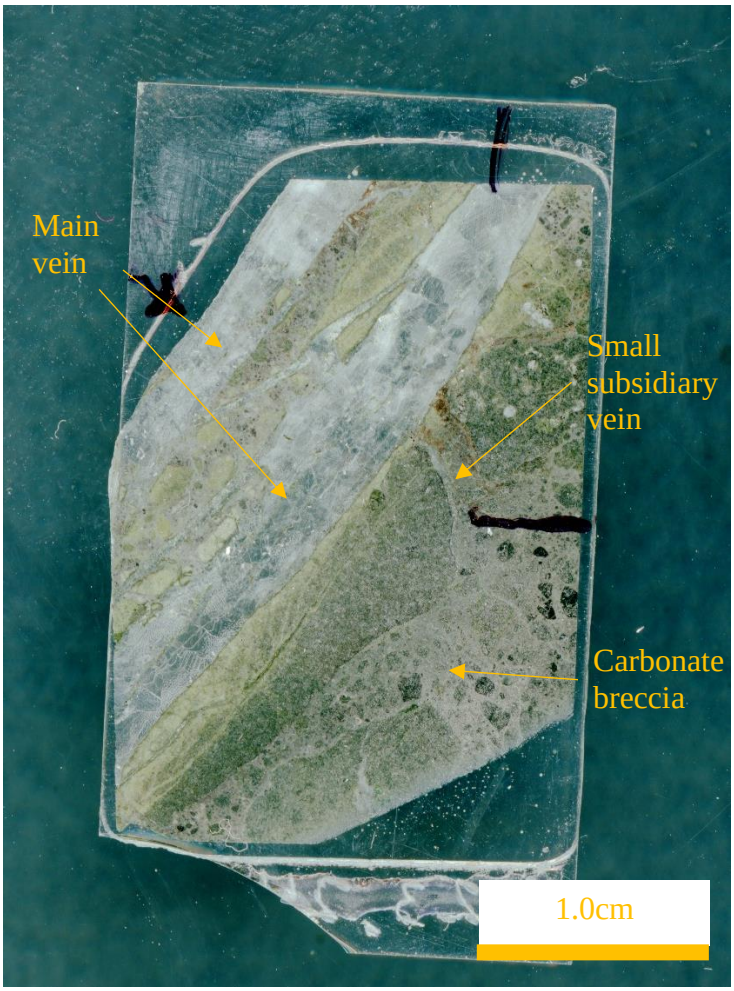

Figure 28 Full thin section scan of sample. This sample presents blocky calcites with interstitial, anhedral quartz.

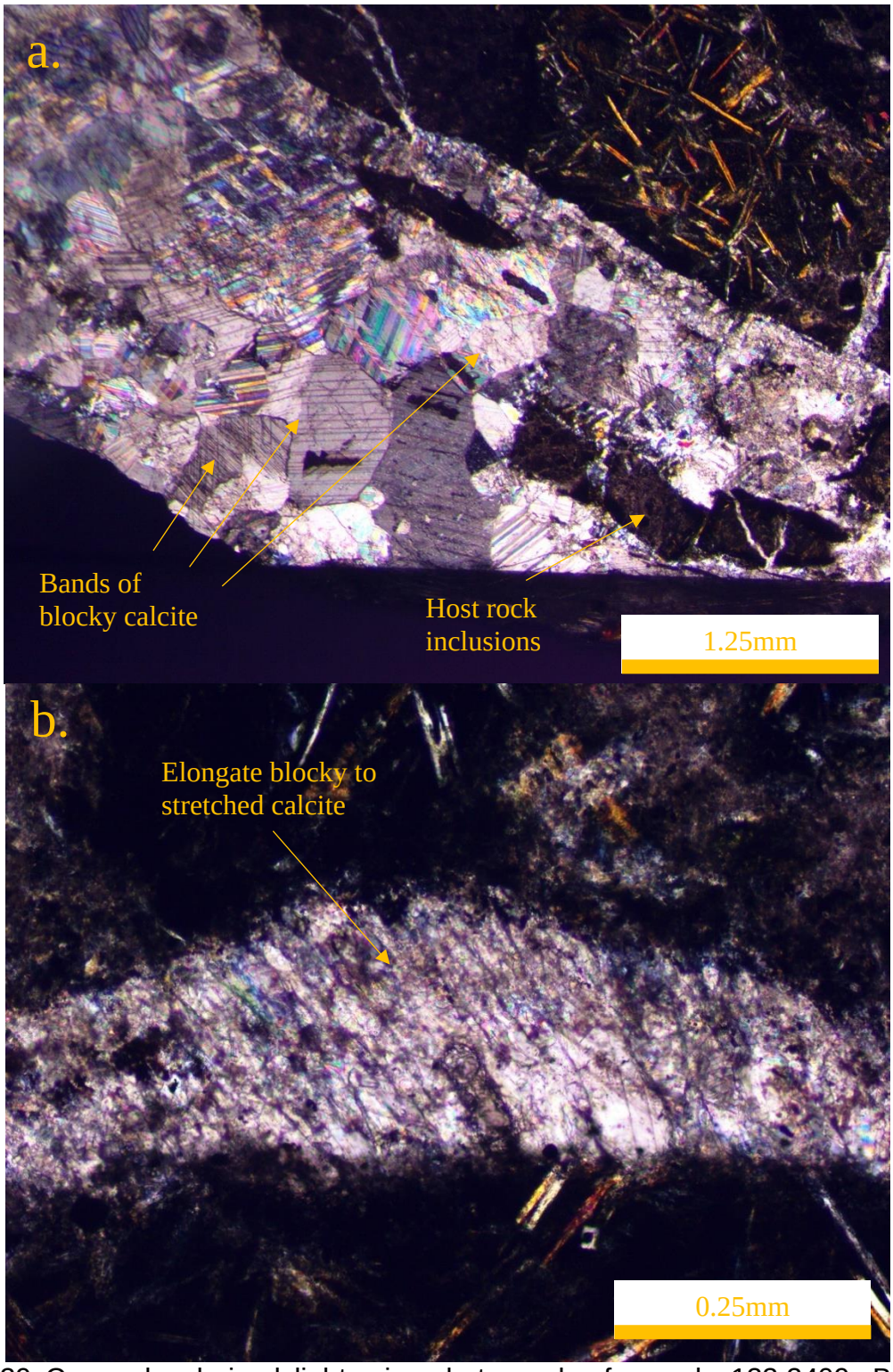

Figure 29 Crossed polarized light microphotograph of sample 123.2409. Bands of blocky calcite and host rock inclusions are representative of the main vein (a.). An elongate blocky to stretched crystal morphology of calcites can be observed in the smaller, subsidiary vein (b.). Note the difference in scale between a. and b.

3.3 EMP Analysis of Select Samples

Further geochemical analyses were conducted on samples 62.1207, 72.1387, 113.2202.1, 123.2396A, and 123.2409. WDS spot analyses were performed on phases spanning veins in these samples, with the primary goal of quantifying the Ca and minor element concentrations in calcite. In sample 62.1207, a single mixed-phase vein was selected for WDS analysis (Figure 30; Table 2). The number beside each labelled calcite crystal in the BSE figures corresponds to the calcite number in each WDS data table, and also corresponds to the calcite number for each LA-ICP-MS analysis.

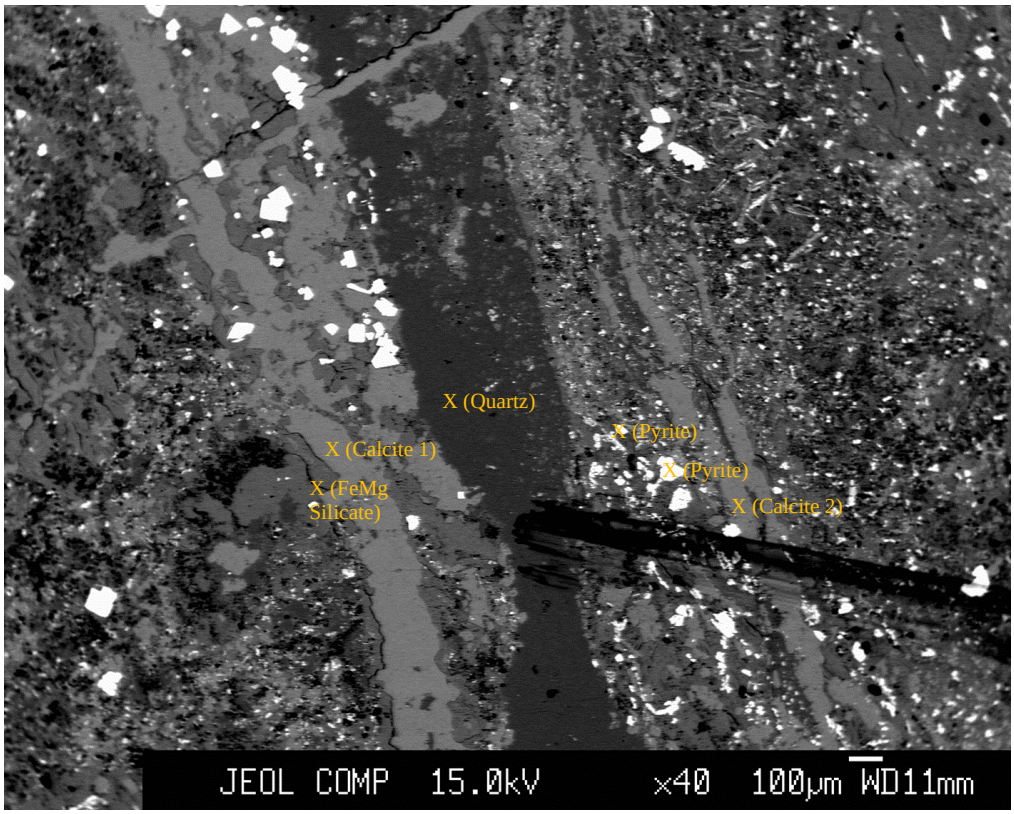

Figure 30 EMP BSE image and location of crystals analyzed for phase confirmation and WDS analysis in sample 62.1207.

Table 2 WDS spot analysis results for calcite in sample 62.1207. Common substitutes for Ca are included. Totals are low because carbon was not analyzed due to the use of a carbon coating.

Sample Name	Calcite #	CaO	MgO	FeO	MnO	BaO	SrO	MgO + FeO + MnO	Total
62.1207 Main Vein	1	54.7751	0.1323	0.9640	1.0952	0.0000	0.0434	2.1915	57.0100
62.1207 Main Vein	2	54.5028	0.2166	1.1333	1.2102	0.0000	0.0738	2.5601	57.1367

In sample 72.1387, WDS analyses were performed on both the pure calcite vein and on the mixed-phase vein (Figure 31; Figure 32; Table 3; Table 4).

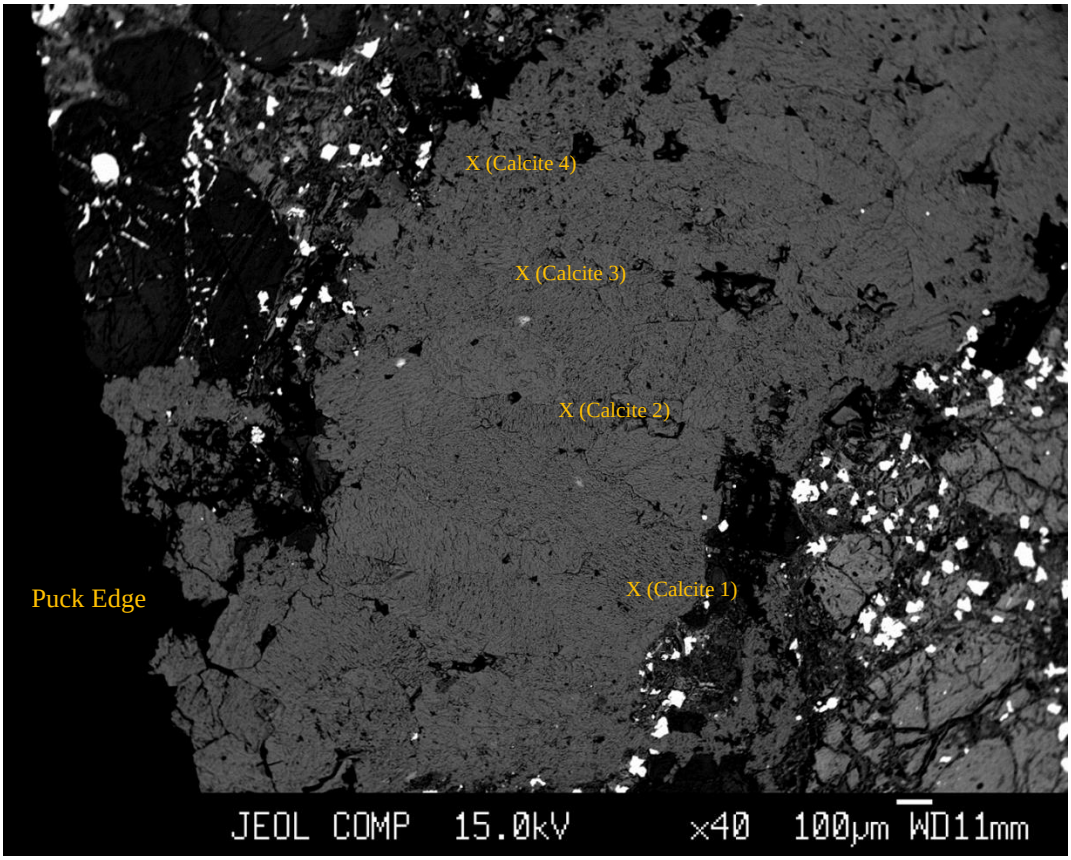

Figure 31 EMP BSE image and location of crystals analyzed for phase confirmation and WDS analysis in sample 72.1387, within its pure calcite vein.

Table 3 WDS spot analysis results for calcite in sample 72.1387 in the pure calcite vein. Common substitutes into calcite are included. Totals are low because carbon was not analyzed due to the use of a carbon coating.

Sample Name	Calcite #	CaO	MgO	FeO	MnO	BaO	SrO	MgO + FeO + MnO	Total
72.1387 Calcite Vein	1	53.0358	0.3868	0.3397	1.7101	0.0000	0.0566	2.4366	55.5290
72.1387 Calcite Vein	2	50.6510	0.5419	0.3608	1.1866	0.0131	0.1242	2.0893	52.8776
72.1387 Calcite Vein	3	54.3501	0.1300	0.2598	0.7636	0.0572	0.2054	1.1535	55.7662
72.1387 Calcite Vein	4	50.8434	0.7651	0.5924	1.3251	0.1269	0.1503	2.6826	53.8032

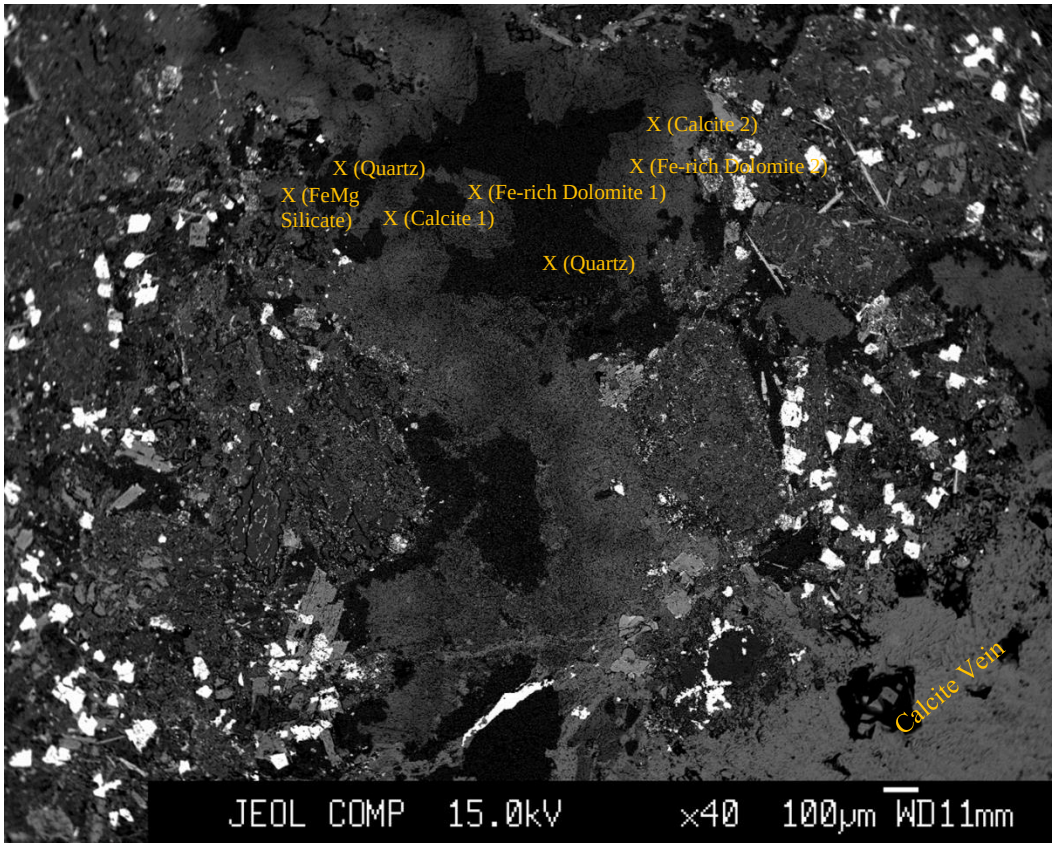

Figure 32 EMP BSE image and location of crystals analyzed for phase confirmation and WDS analysis in sample 72.1387, within its mixed phase vein.

Table 4 WDS spot analysis results for calcite and dolomite in sample 72.1387 in the mixed phase vein. Common substitutes for Ca are included. MgO is excluded from the MgO + FeO + MnO column for dolomite analyses. Totals are low because carbon was not analyzed due to the use of a carbon coating.

Sample Name	Calcite #	CaO	MgO	FeO	MnO	BaO	SrO	MgO + FeO + MnO	Total
72.1387 Mixed Vein	1	49.6502	0.3900	0.9632	0.3404	0.0570	0.4551	1.6936	51.8559
72.1387 Mixed Vein	2	50.9838	0.2781	0.5075	0.7755	0.0000	0.1000	1.5610	52.6448
72.1387 Mixed Vein	Dolomite 1	27.1797	14.2873	7.2978	0.1719	0.0000	0.1690	7.4697	49.1058
72.1387 Mixed Vein	Dolomite 2	28.7919	14.9527	9.0947	0.2661	0.0125	0.2379	9.3608	53.3558

In sample 113.2202.1, WDS analyses were performed on a region of the vein showing only the blocky calcite + interstitial quartz domain and on a region showing both domains (Figure 33; Figure 34). Sample 113.2202.1 is the only sample with visible chemical zonation as observed in the bands of elevated brightness, which is defined by Mn; note the differences in Mn in the 113.2202.1 single domain calcite 3, 4, 5, and 113.2202.1 dual domain calcite 5 (Table 5 and Table 6).

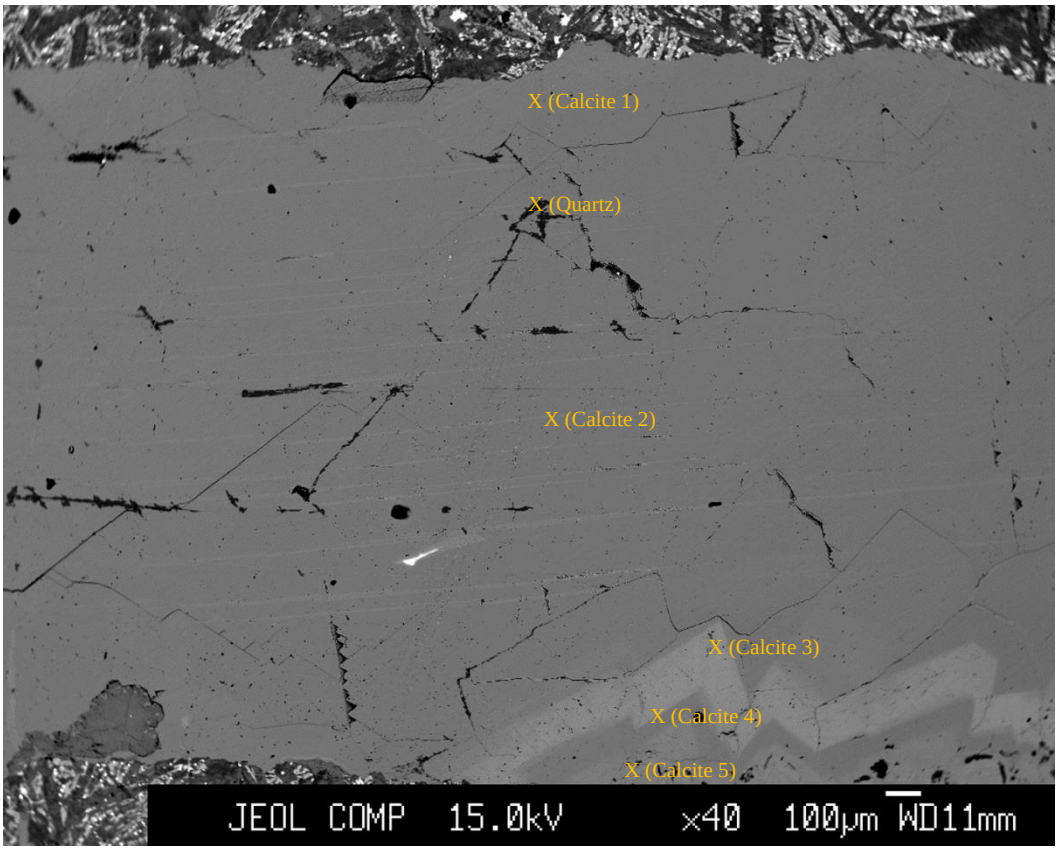

Figure 33 EMP BSE image and location of crystals analyzed for phase confirmation and WDS analysis in sample 113.2202.1, within the side only containing a domain of blocky calcite.

Table 5 WDS spot analysis results for calcite in sample 113.2202.1 in the single domain side of the vein. Common substitutes for Ca are included. Totals are low because carbon was not analyzed due to the use of a carbon coating.

Sample Name	Calcite #	CaO	MgO	FeO	MnO	BaO	SrO	MgO + FeO + MnO	Total
113.2202.1 Single Domain	1	55.4581	0.0000	0.0000	0.0416	0.0133	0.0315	0.0416	55.5444

113.2202.1 Single Domain	2	53.0263	0.0000	0.0104	0.0484	0.0530	0.0000	0.0588	53.1381
113.2202.1 Single Domain	3	54.9622	0.1157	0.1383	3.1234	0.0000	0.0659	3.3774	58.4054
113.2202.1 Single Domain	4	55.0295	0.0000	0.0176	0.0166	0.0707	0.0158	0.0342	55.1503
113.2202.1 Single Domain	5	53.9899	0.0579	0.0125	0.7182	0.0176	0.0569	0.7885	54.8529

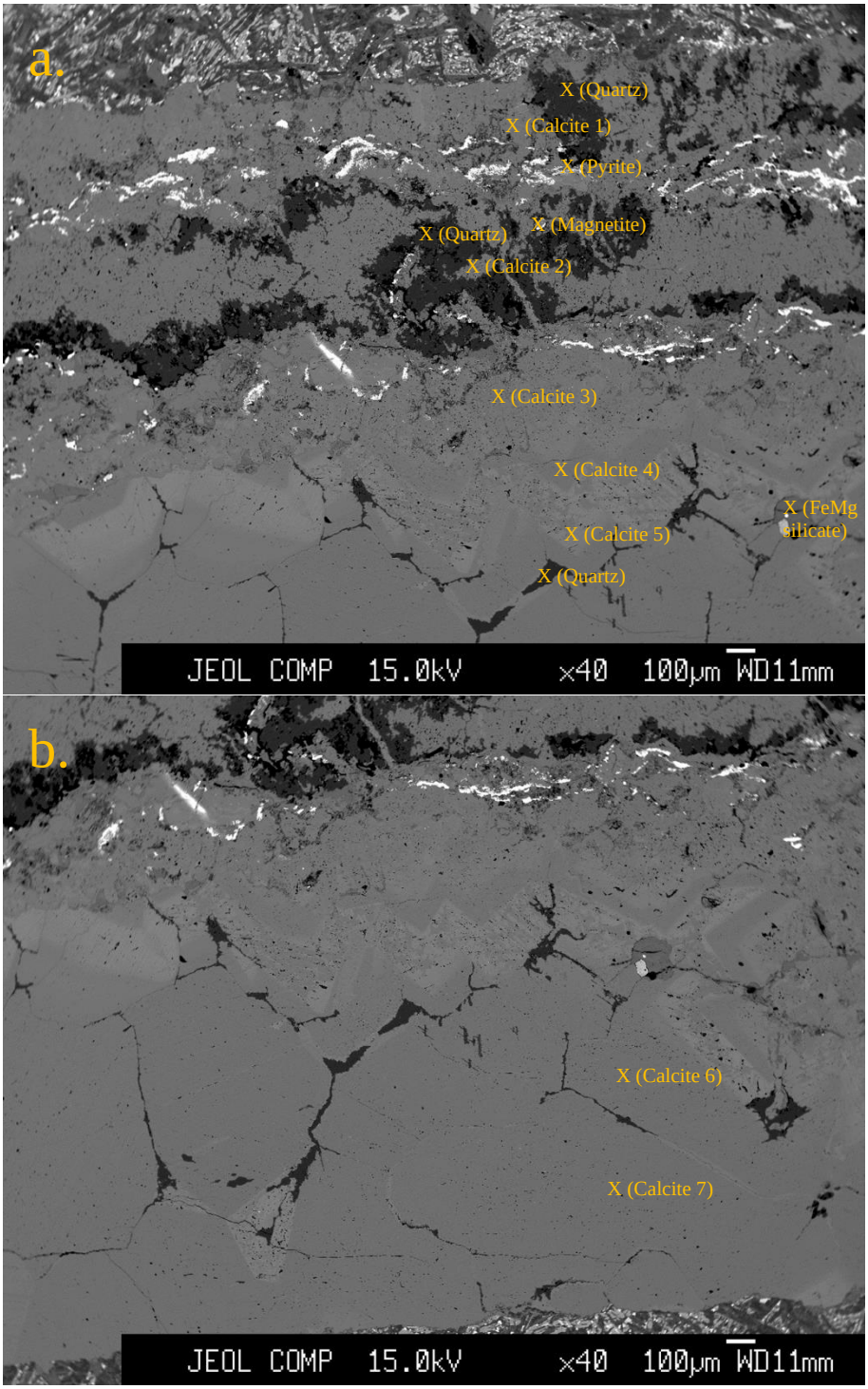

Figure 34 EMP BSE image and location of crystals analyzed for phase confirmation and WDS analysis in sample 113.2202.1, within the side containing a domain of mixed anhedral phases (a.) and a domain of blocky calcite + interstitial quartz (b.). Note the overlap of image extents in a. and b..

Table 6 WDS spot analysis results for calcite in sample 113.2202.1 in the dual domain side of the vein. Common substitutes for Ca are included. Totals are low because carbon was not analyzed due to the use of a carbon coating.

Sample Name	Calcite #	CaO	MgO	FeO	MnO	BaO	SrO	MgO + FeO + MnO	Total
113.2202.1 Dual Domain	1	53.0018	0.0000	0.0171	0.0493	0.0221	0.0515	0.0664	53.1418
113.2202.1 Dual Domain	2	54.5044	0.0193	0.0454	0.3014	0.0000	0.0770	0.3662	54.9476
113.2202.1 Dual Domain	3	53.9356	0.0667	0.0146	0.0399	0.0000	0.0550	0.1212	54.1119
113.2202.1 Dual Domain	4	54.3652	0.0000	0.0000	0.0078	0.0000	0.0447	0.0078	54.4177
113.2202.1 Dual Domain	5	53.8562	0.0890	0.1475	1.1995	0.0220	0.0000	1.4360	55.3142
113.2202.1 Dual Domain	6	55.9682	0.0047	0.0219	0.0728	0.0000	0.0524	0.0994	56.1201
113.2202.1 Dual Domain	7	55.1693	0.0000	0.0060	0.0535	0.0000	0.0590	0.0595	55.2878

In sample 123.2396A, WDS analysis was performed on the main vein near anhydrite occurrences (Figure 35). Anhydrite are found as inclusions in quartz (Figure 35). A thin (~20µm) band of an unknown FeMg silicate mineral is found at the vein edges (Figure 35). While zonation is not visible within calcite as in sample 113.2202.1, the degree of Ca substitution does vary across the sample, with MgO + FeO + MnO ranging from 0.7950 to 3.1503 (Table 7).

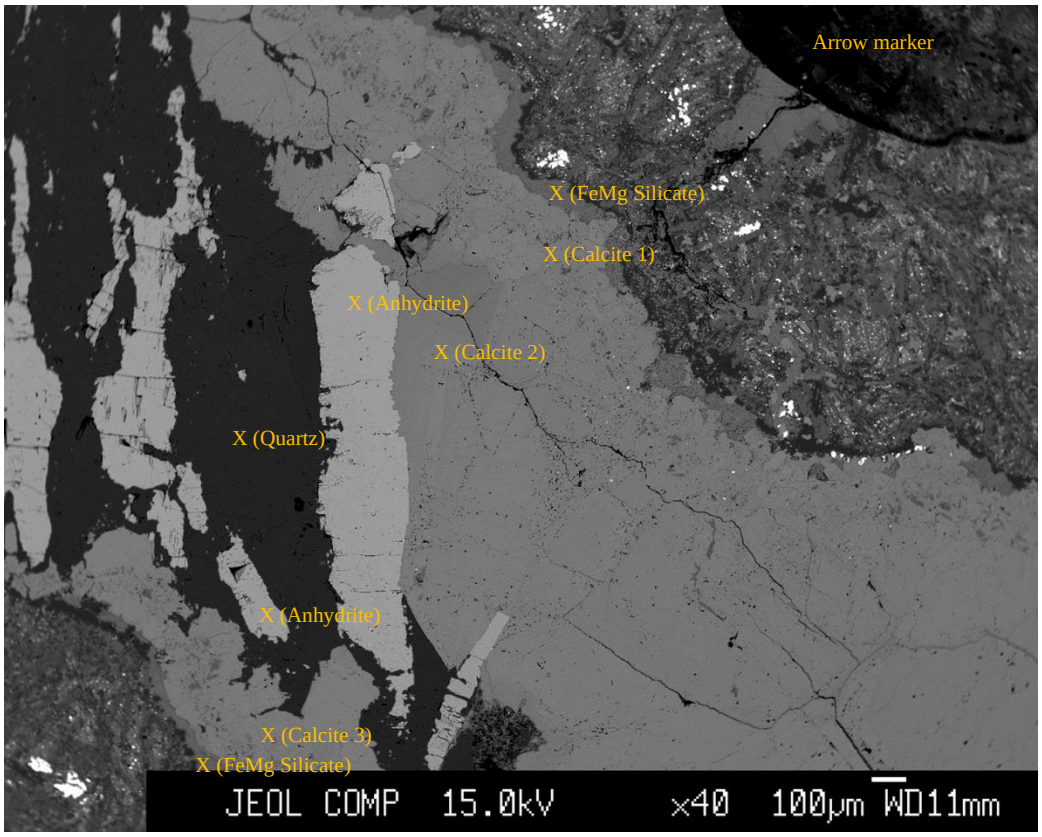

Figure 35 EMP BSE image and location of crystals analyzed for phase confirmation and WDS analysis in sample 123.2396A.

Table 7 WDS spot analysis results for calcite in sample 123.2396A. Common substitutes for Ca are included. Totals are low because carbon was not analyzed due to the use of a carbon coating.

Sample Name	Calcite #	CaO	MgO	FeO	MnO	BaO	SrO	MgO + FeO + MnO	Total
123.2396A Main Vein	1	52.6169	0.4006	1.1909	1.0548	0.0131	0.0424	2.6463	55.3187
123.2396A Main Vein	2	52.8247	0.1065	0.2162	0.4724	0.0000	0.0198	0.7950	53.6396
123.2396A Main Vein	3	52.1077	0.5711	1.4157	1.1635	0.0656	0.1675	3.1503	55.4912

In sample 123.2409, WDS analyses were performed on a region of the main vein and on a region of the smaller subsidiary vein (Figure 36; Figure 37; Table 8; Table 9). In the main vein, visible zonation is not present but the degree of Ca substitution does vary across the main vein, with MgO + FeO + MnO ranging from 0.4488 to 1.9795 (Table 8).

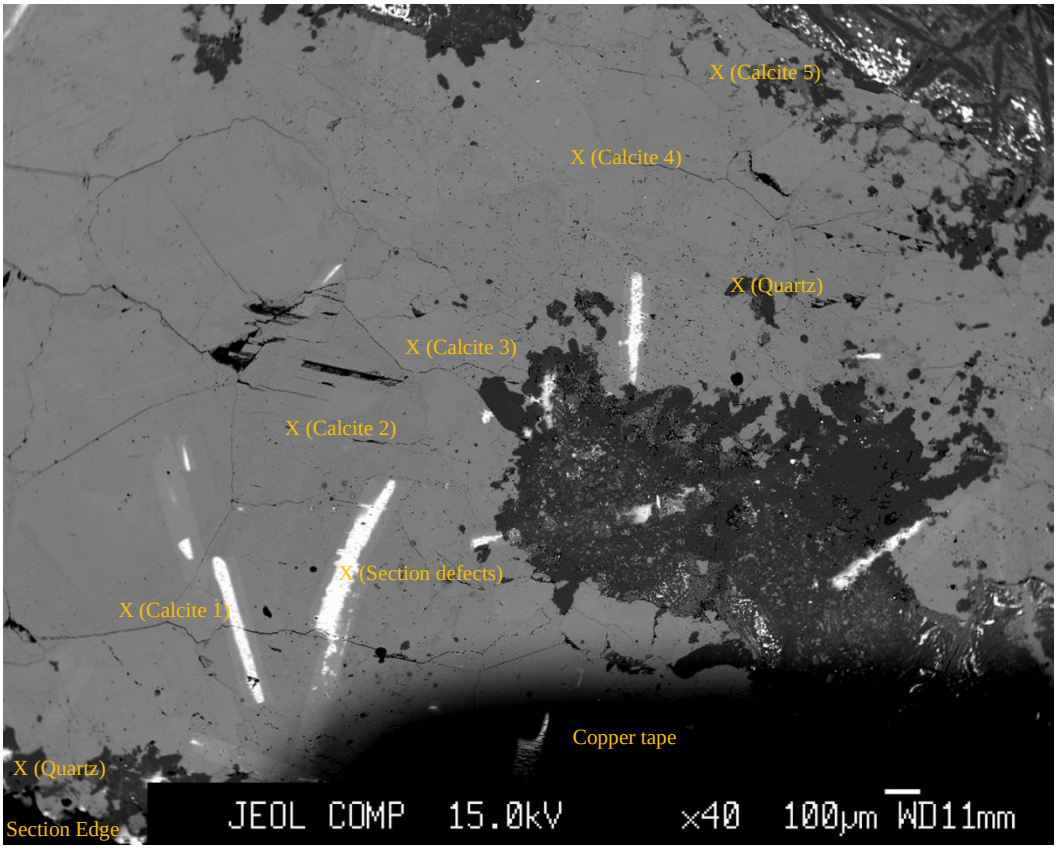

Figure 36 EMP BSE image and location of crystals analyzed for phase confirmation and WDS analysis in sample 123.2409, within its main vein of bands of blocky calcite. Bright, elongate spots are thin section defects.

Table 8 WDS spot analysis results for calcite in sample 123.2409 in the main vein. Common substitutes into calcite are included. Totals are low because carbon was not analyzed due to the use of a carbon coating.

Sample Name	Calcite #	CaO	MgO	FeO	MnO	BaO	SrO	MgO + FeO + MnO	Total
123.2409 Main Vein	1	53.6823	0.0886	0.1477	0.2413	0.0088	0.0658	0.4775	54.2345
123.2409 Main Vein	2	53.8318	0.1085	0.1050	0.2353	0.0000	0.1096	0.4488	54.3902
123.2409 Main Vein	3	55.5189	0.0955	0.2726	0.3462	0.0882	0.2420	0.7143	56.5634
123.2409 Main Vein	4	54.5813	0.2059	0.3193	0.4850	0.0000	0.0624	1.0102	55.6539

123.2409 Main Vein	5	55.3732	0.4714	0.6273	0.8807	0.0088	0.1230	1.9795	57.4845

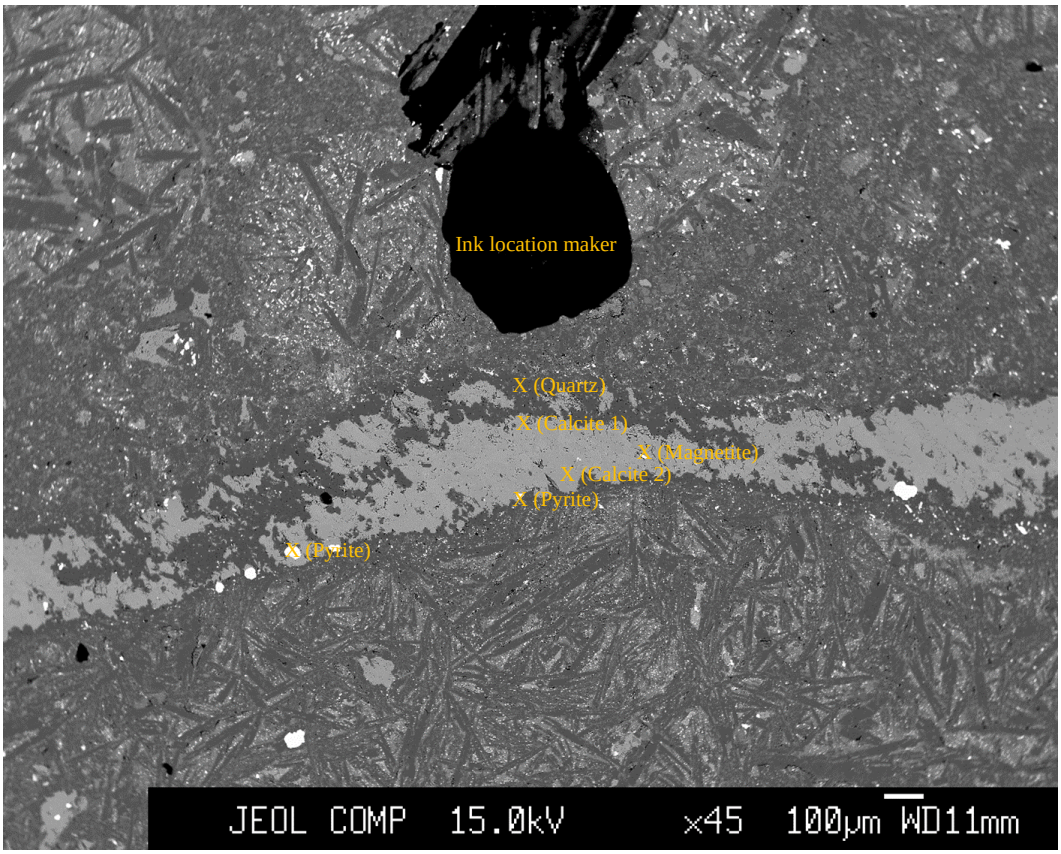

Figure 37 EMP BSE image and location of crystals analyzed for phase confirmation and WDS analysis in sample 123.2409, within its smaller subsidiary vein of elongate blocky to stretched calcite.

Table 9 WDS spot analysis results for calcite in sample 123.2409 in the small vein. Common substitutes into calcite are included. Totals are low because carbon was not analyzed due to the use of a carbon coating.

Sample Name	Calcite #	CaO	MgO	FeO	MnO	BaO	SrO	MgO + FeO + MnO	Total
123.2409 Small Vein	1	55.4198	0.2237	0.6465	0.9735	0.0176	0.0672	1.8436	57.3482
123.2409 Small Vein	2	55.5595	0.2290	0.1787	1.0465	0.0396	0.0080	1.4542	57.0613

In addition to WDS spot analyses, WDS element maps were generated for samples 62.1204.4, 62.1207, and 72.1387 to show spatial variations in Ca, K, Na, Si, Fe, Mg, Al, and Mn (Figure 38 to Figure 40).

Figure 38 shows a calcite vein containing host rock inclusions in sample 62.1204.4. Calcite is distinguished by the highest levels of Ca, while host rock inclusions (mostly albite) have high Si, Na and Al (Figure 37). The common Ca substitutes in calcite (Fe, Mg, and Mn) are all in very low concentration in calcite and do not appear zoned (Figure 37).

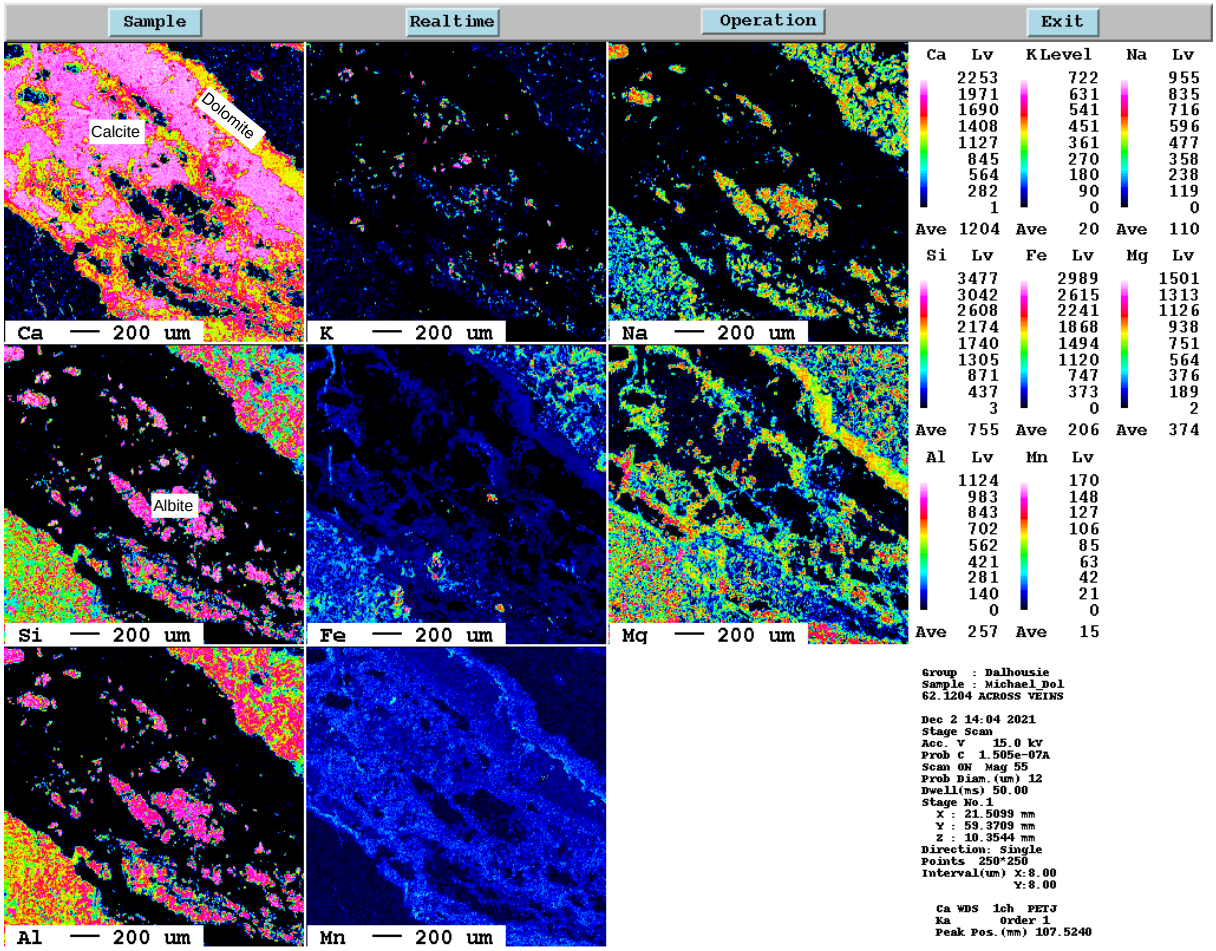

Figure 38 Element mapping of sample 62.1204.4 showing the spatial variation in Ca, K, Na, Si, Fe, Mg, Al, and Mn.

Sample 62.1207 shows a mixed calcite and quartz vein (Figure 39). Calcite occurs toward the edges of the vein, showing the highest levels of Ca; quartz shows the highest levels of Si (Figure 39). As in sample 62.1204.4, the common Ca substitutes in calcite are present in very low concentration and do not appear zoned (Figure 39).

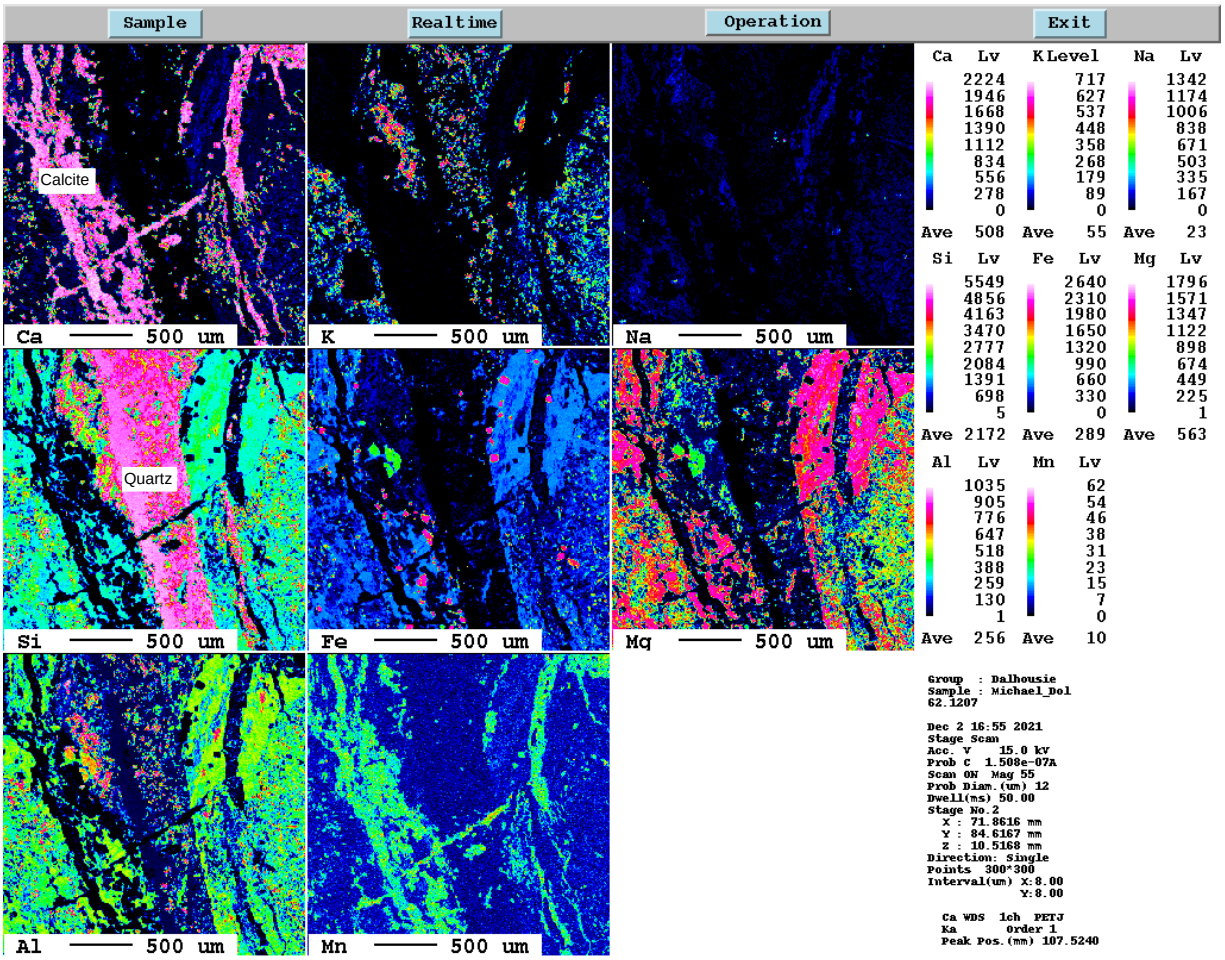

Figure 39 Element mapping of sample 62.1207 showing the spatial variation in Ca, K, Na, Si, Fe, Mg, Al, and Mn.

An intersection of the mixed-phase vein and the calcite vein is present in sample 72.1387 (Figure 40). The calcite vein displays the highest levels of Ca, while the mixed-phase vein shows a mixture of Ca and Mg, typical of the dolomite observed in this vein (Figure 40). While Mn may appear to be present in high quantity in the calcite vein, and may appear to have some zonation, note that the scale of Mn counts is drastically lower than the scale of Ca counts; the true amount and pattern of Mn is being exaggerated by this scale (Figure 40).

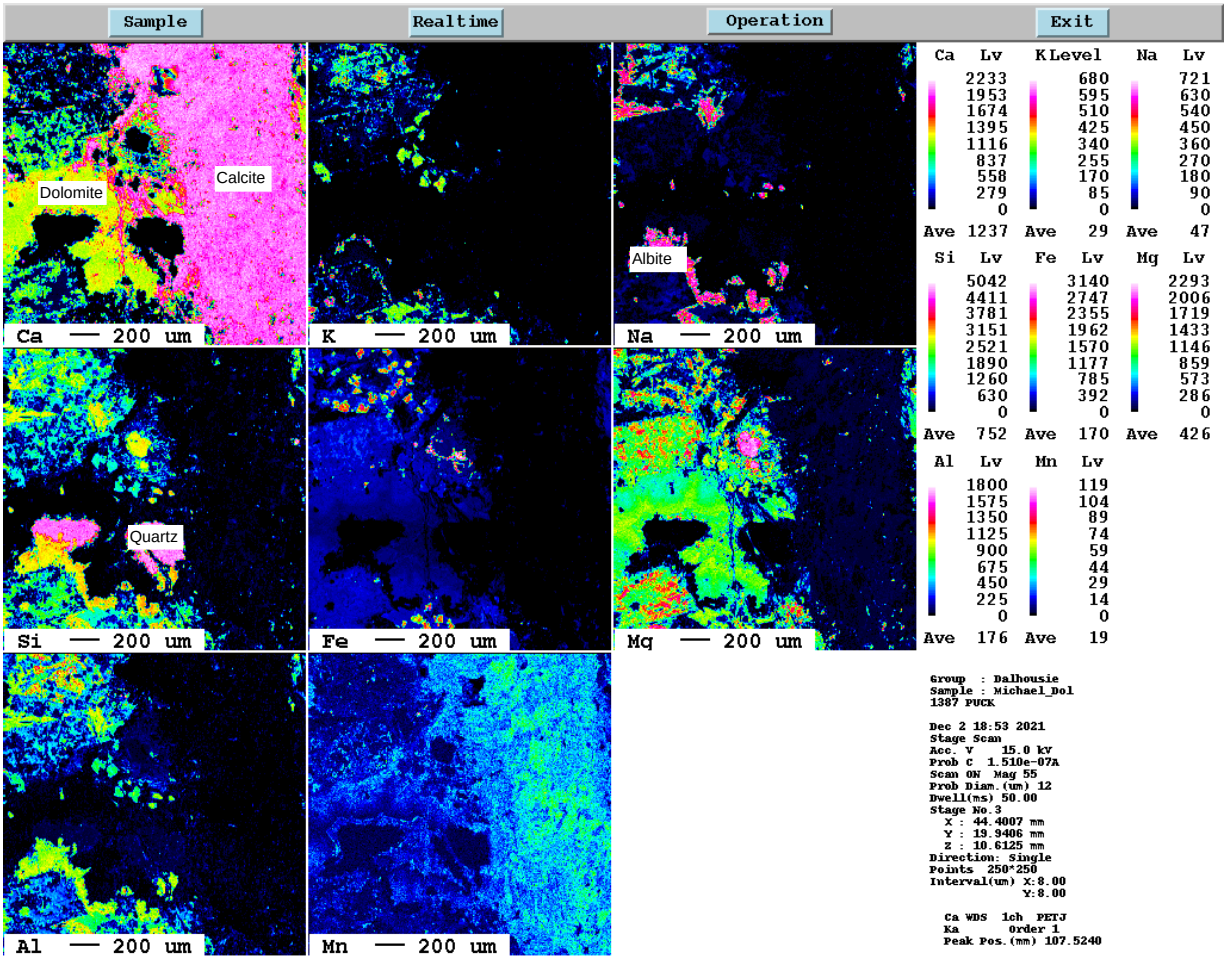

Figure 40 Element mapping of sample 72.1387 showing the spatial variation in Ca, K, Na, Si, Fe, Mg, Al, and Mn.

3.4 Calcite Substitution Characterization

WDS spot analyses were used to measure the composition of calcite phases in terms of the major metal substitutions for Ca (Mg, Fe, and Mn) (Figure 41). Of these three, Mn shows both the highest level of substitution by wt %, followed by Fe and then Mg (Figure 41). 30 total calcite crystals are analyzed (Figure 41).

a.

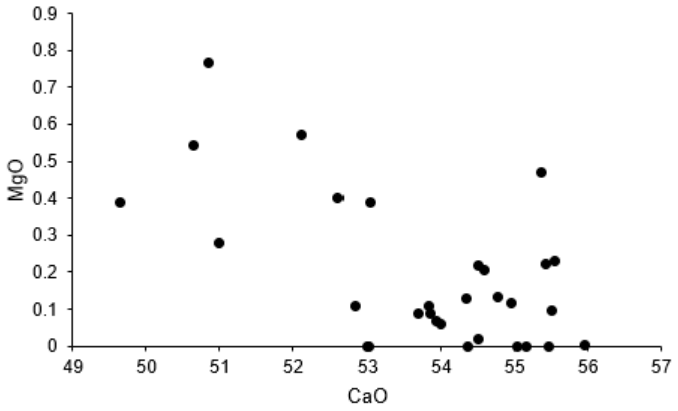

b.

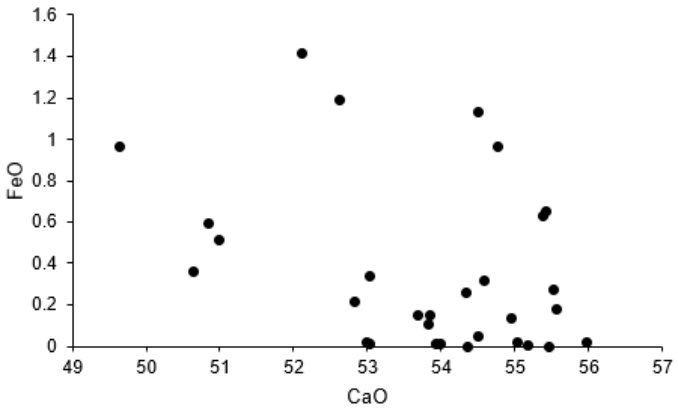

c.

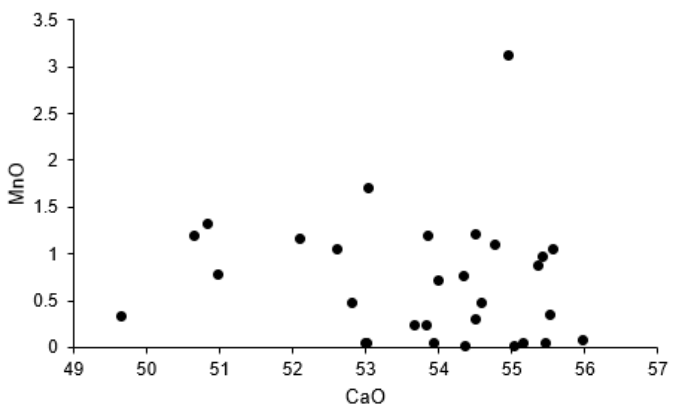

Figure 41 Scatterplots of the common metal substitutions for Ca in calcite versus Ca (a. = Mg, b. = Fe, c. = Mn). All data is reported in wt % oxides. n= 30.

3.5 REY in Calcite

REY data is normalized to the PAAS standard (McLennan 1989 as cited in Rollinson 1993). LREE/HREE ratios (calculated as La/Y), Ce anomalies (calculated as Ce/((La*Pr)^1/2)), Eu anomalies (calculated as Eu/((Sm*Gd)^1/2)), and Y anomalies (calculated as Y/((Dy*Ho)^1/2)) for all analyzed calcite are presented. Calcite numbers below refer to the numbered calcite crystals presented in the BSE images above (Section 3.3).

REY Data for Sample 62.1207

Both calcite crystals analyzed in sample 62.1207 show a similar trend, with LREEs enriched compared to HREEs, positive Eu anomalies, and no Ce anomalies (Figure 42; Table 10). Calcite 1 has a slight negative Y anomaly (Figure 42; Table 10).

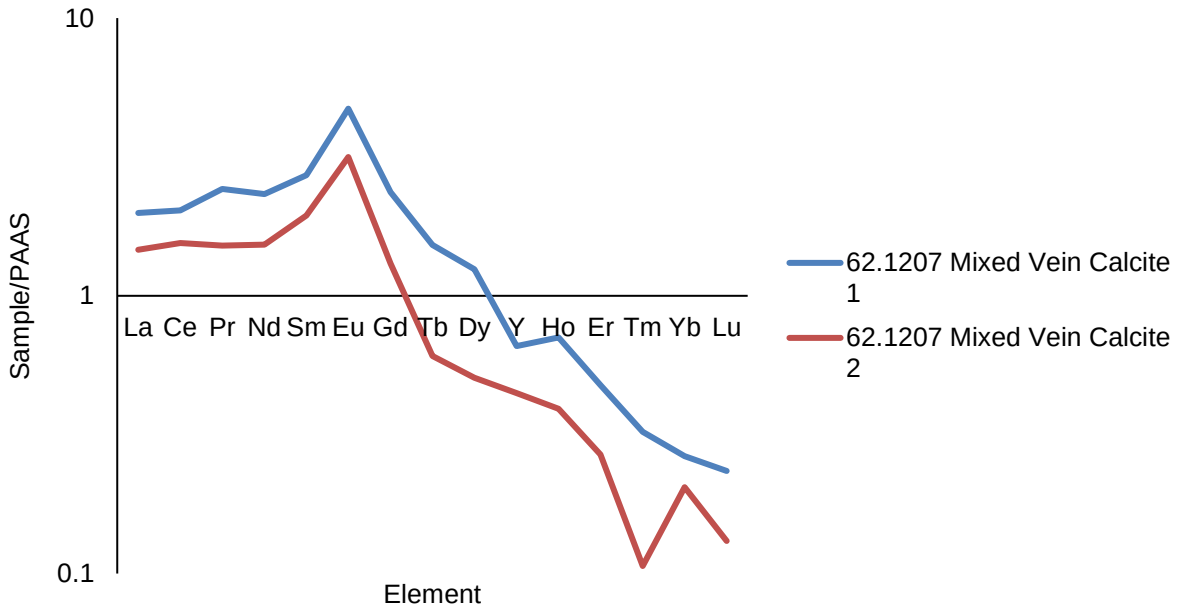

Figure 42 REY trends for calcite crystals analyzed in sample 62.1207.

Table 10 LREE/HREE ratio, Ce anomalies, Eu anomalies, and Y anomalies for analyzed calcite crystals in sample 62.1207.

Sample Name	Calcite #	LREE/HREE	Ce Anomaly	Eu Anomaly	Y Anomaly
62.1207 Mixed Vein	1	3.015314	0.925848	1.86233	0.70128
62.1207 Mixed Vein	2	3.288841	1.03963	1.981933	1.001493

REY Data for Sample 72.1387

Two of the calcite crystals in sample 72.1387 have similar trends, with LREEs enriched over HREEs, positive Eu anomalies, very small negative Ce anomalies, and no Y anomalies (Figure 43; Table 11). These two calcite crystals are in different veins, one being in the vein which is entirely calcite and the other being in the mixed vein (Figure 15). A third calcite crystal, which is also in the mixed vein, shows a different trend with a "saddle-like" REE shape showing LREEs becoming progressively more enriched and HREEs becoming progressively more depleted (Figure 43; Table 11). It also has a large positive Eu anomaly, small negative Ce anomaly, and negligible Y anomaly (Figure 43; Table 11).

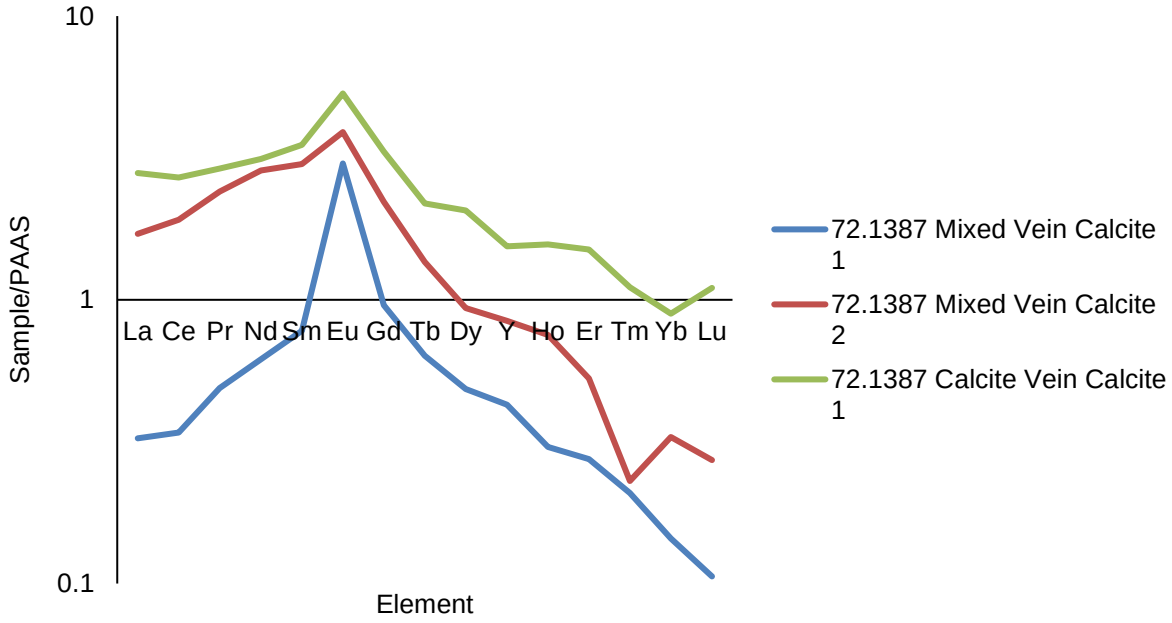

Figure 43 REY trends for calcite crystals analyzed in sample 72.1387.

Table 11 LREE/HREE ratio, Ce anomalies, Eu anomalies, and Y anomalies for analyzed calcite crystals in sample 72.1387.

Sample Name	Calcite #	LREE/HREE	Ce Anomaly	Eu Anomaly	Y Anomaly
72.1387 Mixed Vein	1	0.759909	0.855615	3.503367	1.115793
72.1387 Mixed Vein	2	1.30979	0.909931	1.872608	1.006284
72.1387 Calcite Vein	1	1.81115	0.947187	1.558826	0.858613

REY Data for Sample 113.2202.1

Calcite crystals were analyzed across both the single and dual domain regions of the vein in sample 113.2202.1 (Figure 19). Two trends are present. Single Domain Calcite 3, Single Domain Calcite 5, Dual Domain Calcite 1, and Dual Domain Calcite 2 are all depleted in LREEs relative to HREEs, while Single Domain Calcite 4 and Dual Domain Calcite 3 are enriched in LREEs relative to HREEs (Figure 44; Table 12). All crystals have positive Y anomalies (Figure 44; Table 12). All crystals except for Dual Domain Calcite 3 have positive Eu anomalies (Figure 44; Table 12). Ce anomalies are mostly negligible, with only Single Domain Calcite 5 showing a minor positive Ce anomaly (Figure 44; Table 12).

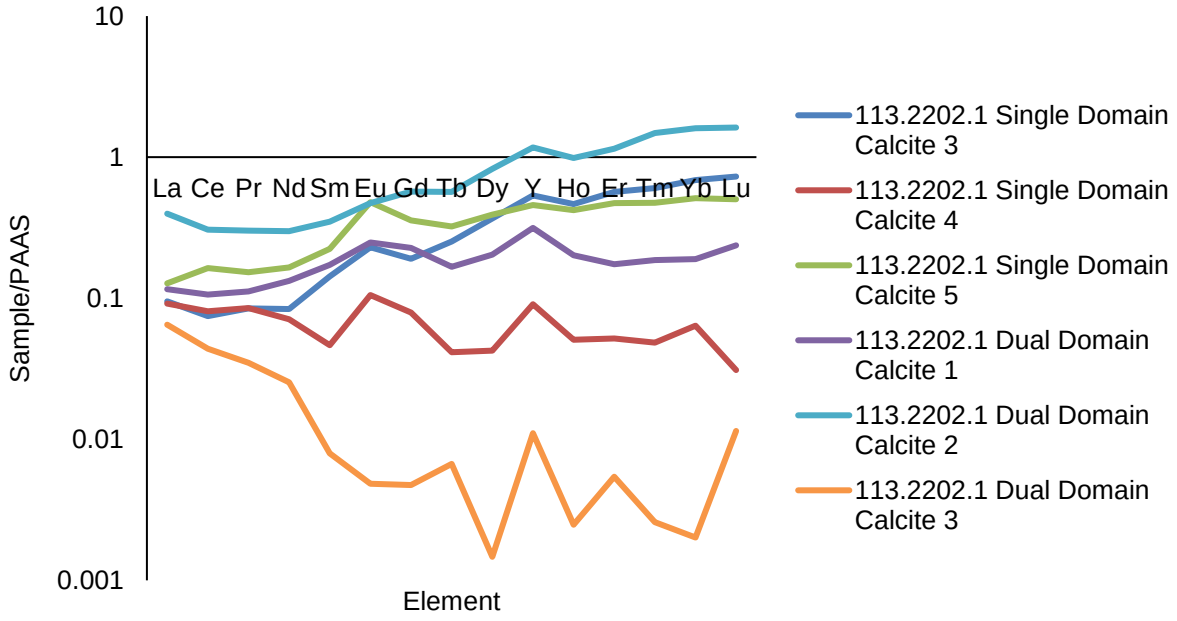

Figure 44 REY trends for calcite crystals analyzed in sample 113.2202.1.

Table 12 LREE/HREE ratio, Ce anomalies, Eu anomalies, and Y anomalies for analyzed calcite crystals in sample 113.2202.1.

Sample Name	Calcite #	LREE/HREE	Ce Anomaly	Eu Anomaly	Y Anomaly
113.2202.1 Single Domain	3	0.177128	0.831633	1.388889	1.297539
113.2202.1 Single Domain	4	1.008759	0.914348	1.734891	1.952326

113.2202.1 Single Domain	5	0.279321	1.169688	1.706292	1.124838
113.2202.1 Dual Domain	1	0.366719	0.933544	1.257131	1.556502
113.2202.1 Dual Domain	2	0.339159	0.885108	1.058948	1.293877
113.2202.1 Dual Domain	3	5.883573	0.920875	0.786726	5.782079

REY Data for Sample 123.2396A

All three calcite crystals analyzed in sample 123.2396A have similar REY trends, with depletion of LREEs relative to HREEs, positive Eu anomalies, and negligible Ce and Y anomalies (Figure 45; Table 13).

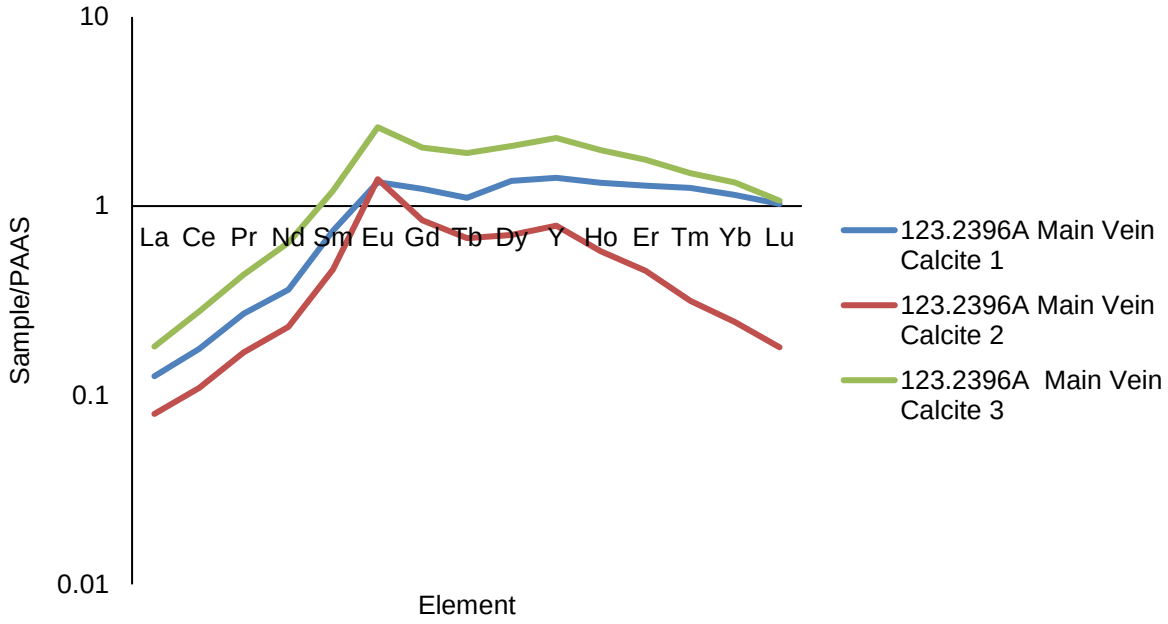

Figure 45 REY trends for calcite crystals analyzed in sample 123.2396A.

Table 13 LREE/HREE ratio, Ce anomalies, Eu anomalies, and Y anomalies for analyzed calcite crystals in sample 123.2396A.

Sample Name	Calcite #	LREE/HREE	Ce Anomaly	Eu Anomaly	Y Anomaly
123.2396A Main Vein	1	0.089355	0.953643	1.401737	1.050672
123.2396A Main Vein	2	0.101154	0.943886	2.224791	1.236039
123.2396A Main Vein	3	0.078875	0.988313	1.666618	1.132292

REY Data for Sample 123.2409

Five calcite crystals were analyzed in the main vein of sample 123.2409 and one was analyzed from the small vein (Figure 36; Figure 37). All crystals from the main vein have similar trends, with LREEs depleted relative to HREEs, large positive Eu anomalies and negligible Ce anomalies; minor positive Y anomalies are occasionally present (Figure 46; Table 14). In contrast, the crystal from the small vein is depleted in LREEs relative to HREEs and has a smaller positive Eu anomaly (Figure; Table 14).

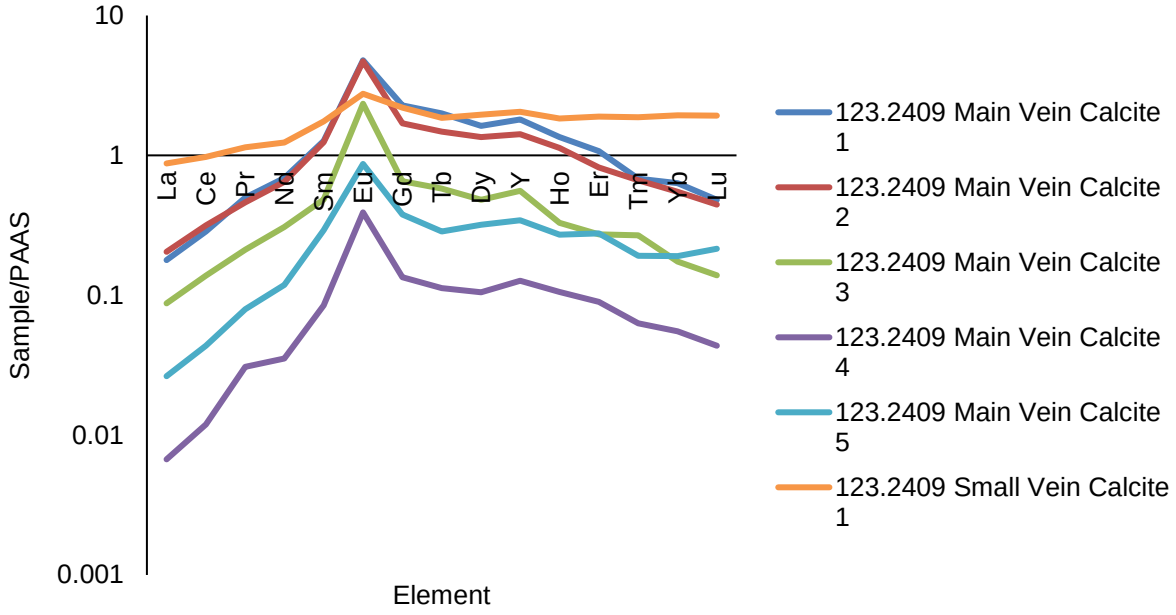

Figure 46 REY trends for calcite crystals analyzed in sample 123.2409.

Table 14 LREE/HREE ratio, Ce anomalies, Eu anomalies, and Y anomalies for analyzed calcite crystals in sample 123.2409.

Sample Name	Calcite #	LREE/HREE	Ce Anomaly	Eu Anomaly	Y Anomaly
123.2409 Main Vein	1	0.099015	0.9607	2.819597	1.214161
123.2409 Main Vein	2	0.144244	1.024223	3.24145	1.147138
123.2409 Main Vein	3	0.156634	1.014003	4.170137	1.405447
123.2409 Main Vein	4	0.052753	0.829167	3.665536	1.207531
123.2409 Main Vein	5	0.076682	0.953568	2.612386	1.168455

123.2409 Small Vein	1	0.427424	0.973504	1.407529	1.083195

Chapter 4: Discussion

4.1 Vein Mineral, Crystal Shape, and Vein Texture Interpretation

All samples are dominated by blocky calcite with interstitial, anhedral quartz. Blocky quartz is found in samples 62.1204.4 and 62.1207. Sample 62.1207 contains the only sampled example of veins dominated by quartz. Limited occurrences of an FeMg silicate are usually found at vein edges, but in some instances this phase can also be found centrally as an interstitial material (e.g., 14.313). Pyrite is observed as an accessory phase in most veins. Magnetite is found in sample 113.2200.5. Both pyrite and magnetite are found coexisting in sample 113.2202.1. Only one instance of dolomite is observed across all samples, with anhedral Fe-rich dolomite found with anhedral calcite in sample 72.1387. Anhydrite is found associated with quartz in sample 123.2396A. Only two instances of non-blocky crystal shape were identified. One instance of elongate-blocky to stretched calcite occurs in sample 123.2409, and one instance of elongate-blocky quartz occurs in sample 62.1207.

The predominance of blocky crystal shape suggests that all but one vein developed syntaxially (Bons et al. 2012). Only one small vein in sample 123.2409 is observed to have calcite which is elongate blocky to stretched in shape. Since crystal shape is mostly governed by growth competition, which is impaired by a lack of void space, this vein is likely still a syntaxial vein which experienced low growth competition (Bons et al. 2012). This is supported by the lack of a median zone which would be present in the case of antitaxial growth, and by the lack of a change in growth direction expected in a stretching vein (Bons et al. 2012).

Some diversity of syntaxial veins exists across the sampled veins. Six samples (113.2202.1, 123.2393, 123.2396A, 123.2396B, 123.2400, and 123.2409) contain blocky calcite with smaller crystal size on at least one edge of the vein; in sample 123.2396A, smaller crystal size occurs on both edges. This smaller crystal size is limited to a single crystal in width, after which significant crystal size increases are observed away from vein edges, with the exception of sample 123.2400; in this sample, crystal size is smallest at the edge, becomes larger away from the edge, and becomes smaller again at the vein centre. These samples differ from the other samples (14.313, 47.924, 62.1204.4,

62.1207, 72.1387, and 113.2200.5) which do not have differences in crystal size across their vein widths. An increase in crystal size away from the vein edge typically reflects a change in the physicochemical environment to favouring nucleation over growth, although the precise change which spurs this is uncertain (Bons et al. 2012). It is noted that there is an apparent association between crystal size change with depth, as all samples displaying a smaller crystal size toward the edge of their veins are from below 670.7m (Table 1).

The syntaxial veins of our samples can also be distinguished by whether there is a single apparent crack-seal cycle or multiple crack-seal cycles (Bons et al. 2012). Samples 62.1204.4, 62.1207, 123.2396B, and 123.2409 show evidence of multiple crack seal cycles. Sample 62.1204.4 is remarkably similar to the prototypical, multiple crack-seal vein proposed by Ramsay (1980), with repeated bands of blocky calcite interrupted by host rock inclusion trails (Figure 12). Each crack-seal cycle in sample 62.1204.4 appears to continue its growth direction where the previous cycle ended, creating continuous calcite crystals across the width of the vein (Figure 12). This further supports the conclusion that this is a syntaxial vein and not a stretching vein, as the growth direction of calcites through multiple crack-seal cycles would be variable in stretching veins (Bons et al. 2012). This consistency of direction suggests that the time elapsed between crack-seal cycles is minimal, as long pauses between cycles would inevitably lead to changes in growth direction, and that the physical conditions present in each cycle are similar (Bons et al. 2012). This is in contrast to the other three samples showing multiple crack-seal cycles. Sample 123.2396B shows two crack-seal cycles, with the first cycle generating the smaller calcite crystals observed toward the vein edge (Figure 25). The second cycle generates the remaining width of the vein located at the vein centre. It is likely that a significant amount of time elapsed between these cycles as thick bands of altered material are found adjacent to each calcite band. Sample 123.2409 has repeated bands of blocky calcite interspersed with bands of smaller blocky calcite, with some trails of host rock inclusions (Figure 29). This suggests that multiple crack-seal cycles occurred, and that each crack-seal cycle brought with it slightly different physical conditions which

favoured nucleation (small crystals) or growth (large crystals). The change in physical condition is likely that of the amount of void space generated as remarked upon earlier.

` The requisite conditions for the formation of blocky calcite, regardless of whether veins contain smaller calcite at their edge, or whether veins are produced from a single crack-seal cycle or multiple crack-seal cycles, is a low-velocity (or stagnant) fluid which has a long residence time in fracture void space (Bons et al. 2012). These fluid characteristics allow for crystal nucleation away from the fracture edge, resulting in larger, blocky crystals to grow directly from solution, and encouraging growth competition between crystals (Bons and Montenari 2005; Bons et al. 2012). This carries with it the requirement that little or no active deformation is occurring at the time of vein mineral deposition as an active differential stress field would necessarily develop a preferential growth direction in vein minerals (Ramsay 1980; Bons et al. 2012; VanderWal 2018).

4.2 Calcite Chemistry Interpretation

The sampled veins are remarkably homogenous in chemical composition. Calcite and quartz are the primary vein phases, together representing the vast majority of the volume of any given vein; it is difficult to identify other phases in thin section and they are often only revealed through BSE imaging. This suggests that Ca is by far the most dominant element in solution, and that the fluid from which vein minerals precipitate is mostly carbonic. As quartz is most often an interstitial phase, Si likely precipitates out of solution last and is confined to interstitial space between blocky calcites. Samples with a greater quartz component (e.g., 62.1207) may therefore represent a later-stage, Ca-poor, Si-rich fluid.

The most common substitutions for Ca in calcite are Fe, Mg, and Mn, which collectively represent 1.2 wt% of analyzed calcite on average (Figure 41; Table 2 to Table 9) (Bons et al. 2012). Of these, Mn is shows the greatest variation with crystal having up to 3.1 wt % Mn (Figure 41). Chemical zoning of individual calcite crystals is only observed in sample 113.2202.1, with Mn-enriched bands of calcite containing up to 3.1 wt% Mn (Figure 33; Figure 34; Table 5; Table 6). Given that such zonation is only observed once, and that it only occurs in a handful of crystals in one portion of the sample, and that it only

accounts for a few wt% of the analyzed crystals, this zonation likely only represents local changes in temperature at time of calcite precipitation. While Mn content varies between calcite crystals in all samples, it is not observed to develop zones such as in sample 113.2202.1.Calcite has been observed to preferentially incorporate Mn at high temperatures, thus the high-Mn regions likely formed at slightly elevated temperatures relative to other regions of crystal (Mucci and Morse 1983). This is further supported by the observation that Mn is preferentially incorporated low precipitation rates, concomitant with the large, blocky calcites observed in sample 113.2202.1 (Figure 19) (Mucci and Morse 1983).

4.3 Fluid Source from REY

Three trends can be identified across samples which were analyzed for REY data (Figure 47). The first trend is characterized by enrichment of LREEs relative to HREEs, large positive Eu anomalies, and a lack of substantial Ce and Y anomalies (Figure 47 a.). This trend is present in samples 62.1207 and 72.1387, except for sample 72.1387 Calcite 1 (Figure 47). The second trend is characterized by depletion of LREEs relative to HREEs, large positive Eu anomalies, and a lack of substantial Ce and Y anomalies (Figure 47 b.). This trend is observed in sample 72.1387 Calcite 1, and all calcite in samples 123.2396A and 123.2409 (Figure 47 b.). These two trends are similar to each other in their anomalies as both show large positive Eu anomalies and lack other substantial anomalies (Figure 47). When compared to known fluid standard, these trends are most similar to that of a high-temperature hydrothermal fluid (Figure 4) (Zhao et al. 2021).

Of the three possible fluids which could have contributed to the development of vein minerals in Bermuda, the REY trend observed in samples 62.1207, 72.1387, 123.2396A, and 123.2409 (Figure 47 a. and b.) are most similar to a high-temperature hydrothermal fluid (Zhao et al. 2021). High-temperature hydrothermal fluids are distinct from low-temperature hydrothermal fluids in their lack of negative Ce anomalies and their more pronounced Eu anomalies (Zhao et al. 2021). Both types of hydrothermal fluids are distinguished from ambient seawater in their lack of Y anomalies, and by the drastic Ce anomalies observed in seawater (Figure 4) (Zhao et al. 2021). Interestingly, the change

in LREE/HREE ratio observed across these samples is not expected in hydrothermal fluids, which typically have LREE/HREE ratios of roughly 1 (Sharm and Srivastava 2014; Zhao et al. 2021). There may be a weak correlation between depth and LREE depletion, with samples from deeper in the core having less LREE depletion (Figure 47). If this is the case, LREE may deplete as the fluid approaches the surface; this trend may be expected if fluids circulate from the bottom of the igneous units toward the top, with samples having higher LREE precipitating first. The difference observed in the relative enrichment or depletion of LREEs may also be caused by remobilization; LREEs are known to more readily become mobile should calcite experience a remobilization event (Bau and Moller 1991). However, we cannot be certain that this is the case. Cathodoluminescence methods would provide information about recrystallization, but attempts at using this method in the current work failed. The exact reasons for LREE depletion in these samples is not known.

The third trend is found solely in sample 113.2202.1 (Figure 47 c.). Some of these analyses are LREE enriched, others are LREE depleted; some have small positive Eu anomalies, others do not. The strongest commonalities between these analyses are their lack of substantial Ce anomalies and the presence of small positive Y anomalies (Figure 47 c.). This data is only sparingly called a trend as there is variation between individual analyses and they are grouped together on the basis that their meaning is uncertain.

The fluid identity corresponding to the REY trend observed in sample 113.2202.1 is unclear. The lack of a negative Ce anomaly should preclude this trend from representing low-temperature hydrothermal fluids or seawater, yet the presence of a slight positive Y anomaly is indicative of seawater (Figure 4; Figure 47 c.) (Zhao et al. 2021). In the calcite analyses for sample 113.2202.1 which yield a slight positive Eu anomaly, the magnitude of this anomaly is nowhere near such anomalies seen in high-temperature hydrothermal fluids (Figure 4; Figure 47 c.) (Zhao et al. 2021). Other calcite analyses in sample 113.2202.1 lack Eu anomalies altogether (Figure 47 c.). This mixture of REY trend features may support the identity of this fluid as a mixture between high-temperature hydrothermal fluid and seawater, but the evidence is not sufficient to be certain,

a.

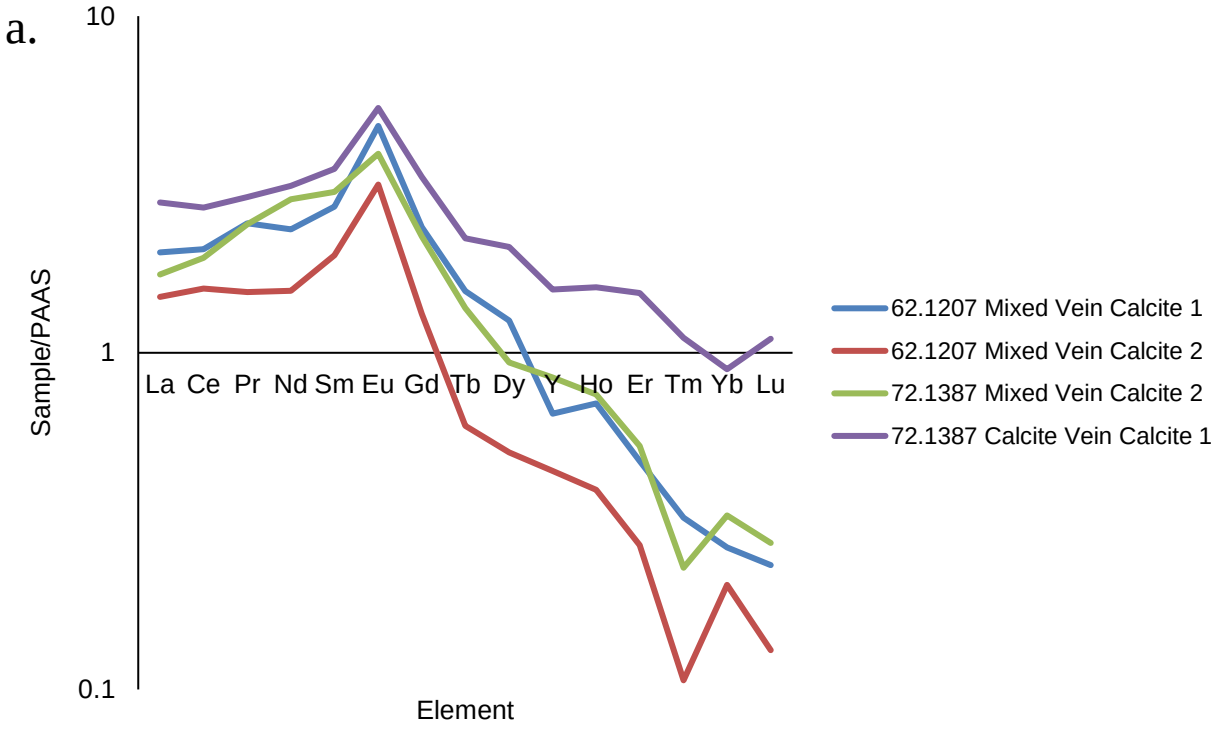
10
1
0.1
Sample/PAAS
La Ce Pr Nd Sm Eu Gd Tb Dy Y Ho Er Tm Yb Lu
Element
62.1207 Mixed Vein Calcite 1
62.1207 Mixed Vein Calcite 2
72.1387 Mixed Vein Calcite 2
72.1387 Calcite Vein Calcite 1

b.

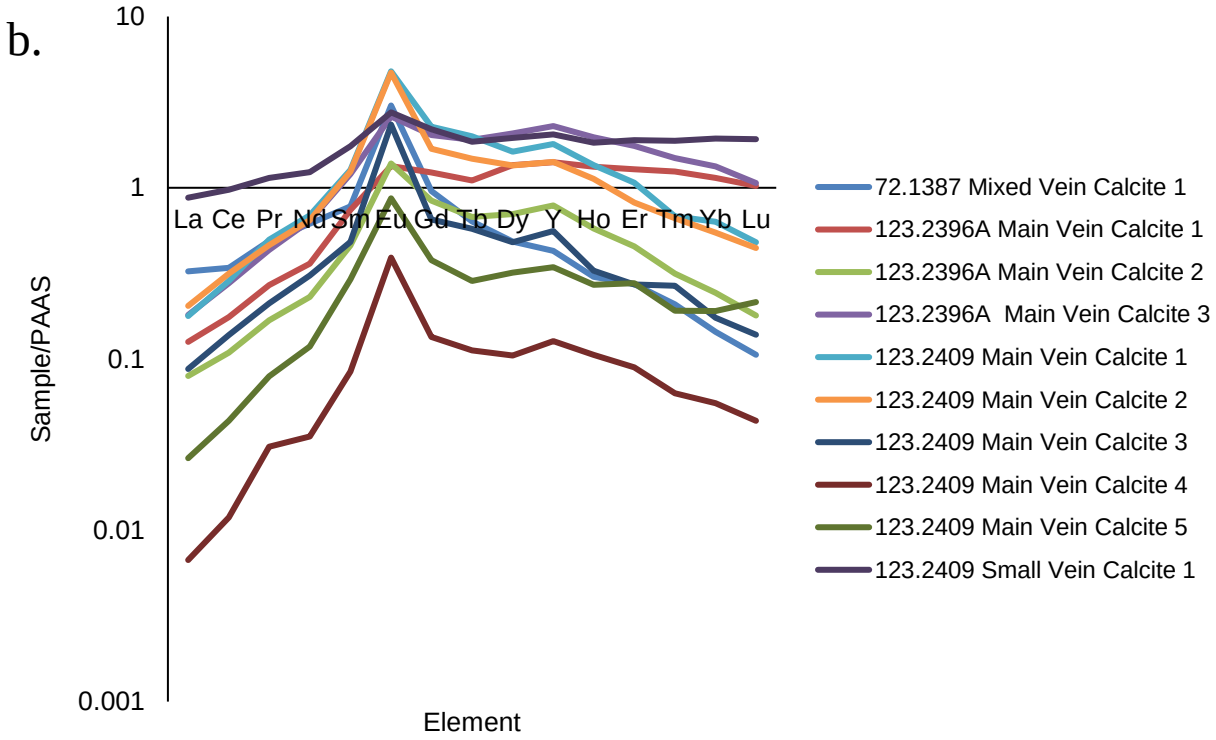
10
1
0.1
0.01
0.001
Sample/PAAS
La Ce Pr Nd Sm Eu Gd Tb Dy Y Ho Er Tm Yb Lu
Element
72.1387 Mixed Vein Calcite 1
123.2396A Main Vein Calcite 1
123.2396A Main Vein Calcite 2
123.2396A Main Vein Calcite 3
123.2409 Main Vein Calcite 1
123.2409 Main Vein Calcite 2
123.2409 Main Vein Calcite 3
123.2409 Main Vein Calcite 4
123.2409 Main Vein Calcite 5
123.2409 Small Vein Calcite 1

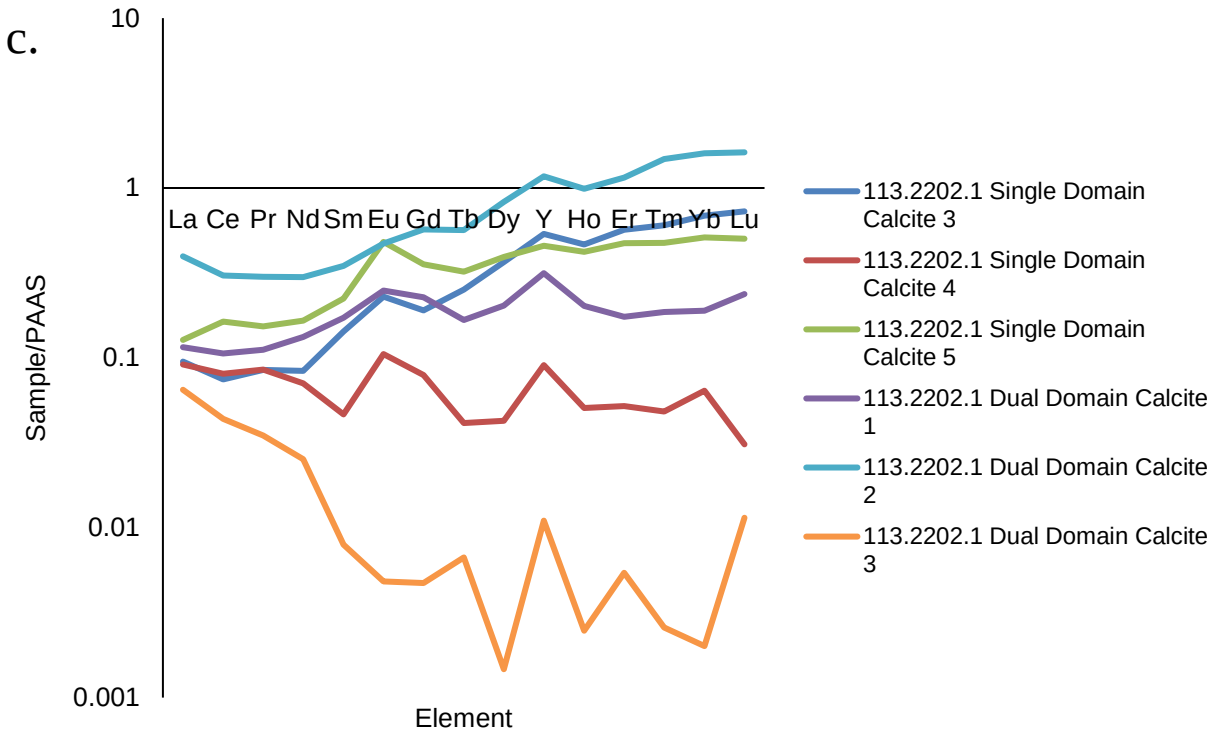

Figure 47 REY data showing grouped according to the three trends identified across samples. Trends a. and b. are most similar to high-temperature hydrothermal fluids, while trend c. is of unclear fluid origin (Zhao et al. 2021).

4.4 Limitations

The primary limitation to the present work is the sampling regime. Intended as a pilot study, this work is to be the first stage of study into the veins of the Bermuda igneous units. Random sampling of veins was aimed at retrieving sufficient material so that the essential methods of optical microscopy and trace element analysis of unaltered phases could be completed. It is likely that there is a greater diversity of vein minerals (Mazza et al. 2019 notes the presence of hæmatite veins), crystal shapes, and vein textures within the Bermuda igneous units than is reported herein. Crucially, this work reports only veins within the basaltic flows because a concerted effort to find veins within the ultramafic intrusive suite was not undertaken. This limitation makes it impossible to make conclusions about the relationship between veining and each igneous suite.

Furthermore, the suite of methods applied in the present work occupy a narrow domain of the analytical techniques developed for the study of carbonate veins. The

methods of cathodoluminescence, stable isotope analysis (carbon and oxygen), clumped isotope palaeothermometry, and radiogenic isotope (typically rubidium/strontium (Rb/Sr) and uranium/lead (U/Pb)) analysis have all been applied in previous study of carbonate veining (Bons et al. 2012; VanderWal 2018; Quandt et al. 2019; Quandt et al. 2021). Cathodoluminescence may reveal if recrystallization has occurred, and what the original crystal morphology of vein minerals was prior to this recrystallization (Bons et al. 2012). Cathodoluminescence was attempted by two different methods for the present work, but proper imaging was not possible. Stable isotope analysis can further restrain the fluid source and is considered less susceptible to error as isotopes of the same element do not fractionate according to chemical differences, as is the case with REYs (Bons et al. 2012; VanderWal 2018; Quandt et al. 2019; Quandt et al. 2021). Stable isotope analysis was not performed for the current work due to time limitations. Where recrystallization has not occurred, radiogenic isotope analysis can provide a method of aging vein calcite (Bons et al. 2012; VanderWal 2018).

Finally, limitations of detection limits and detection error are ever-present limitations for geochemical studies. Particular to the current work, detection limits for LA-ICP-MS required that linear transects be used instead of spot analyses for all calcite crystals because of the thickness of the thin section samples. Despite this attempt to expand the volume of material collected for analysis, 5 of the 25 analyzed calcite crystals returned values below detection limits.

4.5 Proposal for Future Study

Future studies on veins of the Bermuda igneous units should focus on conducting a systematic sampling of veins in the drill core and on additional analytical techniques. First and foremost, a representative sampling of the core is needed to fully describe veining, the distribution of veins between the two igneous suites, and to capture a wider diversity of vein minerals, crystal shapes, and vein textures. Additionally, the methods of cathodoluminescence, stable isotope analysis, and radiogenic isotope analysis as noted in section 4.3 should be pursued to further refine the conditions under which the veins formed and to assess the timing of their formation.

Chapter 5: Conclusions

This work has characterized the vein growth textures and crystal shapes present across 13 samples of veins in the Deep Drill 1972 drill core. It also presents the major, minor, and trace element compositions of select veins within those samples. As a pilot study, this work is intended to provide a starting point for further study of the veins of this drill core. While conclusions are limited, we can state that:

1. All sampled veins experienced syntaxial growth.
2. Calcite is the dominant vein mineral, and quartz is often found as interstitial material between calcite crystals. Veins where blocky quartz occurs may therefore represent a later-stage, Ca-poor, Si-rich fluid.
3. Calcite are always blocky, suggesting that nucleation was preferred over growth in the physical-chemical environment present during vein development.
4. Accessory minerals include pyrite, magnetite, and anhydrite.
5. Some veins show evidence from REY data of being derived from high-temperature hydrothermal fluids, while others show a mixed fluid origin or unclear REY trend. REY trends which are similar to high-temperature hydrothermal fluids yet have depleted LREEs may be evidence of remobilization.

References

Aumento F, Gunn BM. 1974. Geology of the Bermuda Seamount [unpublished]. Available from: http://www.geokem.com/files/Bermuda.pdf

Barker SLL, Cox SF. 2011. Oscillatory zoning and trace element incorporation in hydrothermal minerals: Insights from calcite growth experiments. Geofluids. 11:48-56.

Bau M, Moller P. 1991. Rare earth element fractionation in metamorphogenic hydrothermal calcite, magnesite, and siderite. Mineral. Petrol. 45:231-246.

Bau M, Dulski P. 1999. Comparing yttrium and rare earths in hydrothermal fluids from the Mid-Atlantic Ridge: Implications for Y and REE behaviour during near-vent mixing and for the Y/Ho ratio of Proterozoic seawater. Chem Geol. 155:77-90.

Bons PD, Montenari M. 2005. The formation of antitaxial calcite veins with well-devleoped fibres, Oppaminda Creek, South Australia. J Struct Geol. 27:231-248.

Bons PD, Elburg MA, Gomez-Rivas E. 2012. A review of the formation of tectonic veins and their microstructures. J Struct Geol. 43:33-62.

Debruyne D, Hulsbosch N, Muchez P. 2016. Unraveling rare earth element signatures in hydrothermal carbonate minerals using a source-sink system. Ore Geol Rev. 72:232-252.

Duncan RA. 1984. Age progressive volcanism of the New England seamounts and the opening of the central Atlantic ocean. J Geophys Res. 89(B12):9980-9990.

Fisher DM, Brantley SL, Everett M, Dzvonik J. 1995. Cyclic fluid flow through a regionally extensive fracture network within the Kodiak accretionary prism. J Geophys Res. 100:12881-12894.

Griffin DJ, Grover MA, Kawajiri Y, Rousseau RW. 2014. Supersaturation control during fractional crystallization [conference paper]. International Symposum on Industrial Crystallization; September 2014; Toulouse (FR). 6p. Note: I did not want to cite another textbook and this paper has a nice, succinct description of supersaturation.

Kennedy ME. 1999. Elements: Trace. In: Marshall CP, Fairbridge RW, editors. Encyclopedia of Geochemistry. Dordrecht (NL): Kluwer Academic Publishers. p. 222-223.

Mazza SE, Gazel E, Bizimis M, Moucha R, Beguilin P, Johnson EA, McAleer RJ, Sobolev AV. 2019. Sampling the volatile-rich transition zone beneath Bermuda. Nature. 569: 398-403.

McLennan SM. 1989. Rare earth elements in sedimentary rocks: Influence of provenance and sedimentary processes. Rev Mineral. 21:169-200.

Migaszewski ZM, Galuszka A. 2014. The characteristics, occurrence, and geochemical behaviour of rare earth elements in the environment: A review. Crit Rev Environ Sci Technol. 45(5):429-471.

Morgan WJ. 1981. Hotspot tracks and the early rifting of the Atlantic [conference paper]. Processes of Planetary Rifting; 1981 December 3-5; Napa Valley (CA): Lunar and Planetary Institute. 4p.

Mucci A, Morse JW. 1983. The incorporation of Mg^{2+} and Sr^{2+} into calcite overgrowths: Influences of growth rate and solution composition. Geochim Cosmochim Acta. 47:217-233.

Oliver NHS, Bons PD. 2001. Mechanisms of fluid flow and fluid-rock interaction in fossil metamorphic hydrothermal systems inferred from vein-wallrock patterns, geometry and microstructure. Geofluids. 1:137-162.

Olsen SD. 2005. Petrogenesis of Bermuda's igneous basement: Petrology and geochemistry of the 1972 and 1980 recovered dyke rocks [master's thesis]. Copenhagen (DK): University of Copenhagen

Paton C, Hellstrom J, Paul B, Woodhead J, Hergt J. 2011. Iolite: Freeware for the visualization and processing of mass spectrometric data. J Anal At Spectrom. 11:2508-2518.

Quandt D, Micheuz P, Kurz W, Kluge T, Boch R, Hippler D, Krenn K, Hauzenberger CA. 2019. Geochemistry of vein calcites hosted in the Troodos Pillow Lavas and their implication for the timing and physicochemical environment of fracturing, fluid circulation, and vein mineral growth. Geochem. Geophys. 20: 5913-5938.

Quandt D, Kurz W, Micheuz P. 2021. Post-magmatic fracturing, fluid flow, and vein mineralization in supra-subduction zones: A comparative study on vein calcites

from the Troodos ophiolite and the Izu-Bonin forearc and rear arc. Int J Earth Sci. 110:627-649.

Ramsay JG. 1980. The crack-seal mechanism of rock deformation. Nature (284):135-139.

Rollinson H. 1993. Using geochemical data: Evaluation, presentation, interpretation [textbook]. New York (NY): Routledge.

Sharma R, Srivastava PK. 2014. Hydrothermal fluids of magmatic origin. In: Kumar S, Singh RN, editors. Modelling of Magmatic and Allied Processes, Society of Earth Scientists Series. Switzerland: Springer International Publishing. p. 181-208.

VanderWal J. 2018. Calcite fracture-filling: A proxy for geothermal energy systems, and implications for the tectonic history of the Northeastern Midland Valley, Scotland [undergraduate thesis]. Halifax (NS): Dalhousie University. 79p.

Vogt PR, Jung WY. 2007. Origin of the Bermuda volcanoes and Bermuda Rise: History, observations, models, and puzzles. In: Foulger GR, Jurdy DM, editors. Plates, Plumes and Planetary Processes.Boulder (CO): Geological Society of America.

Zhao Y, Wei W, Li Sanzhong, Yang T, Zhang R, Somerville I, Santosh M, Wei H, Jiaqing W, Yang J, et a. 2021. Rare earth element geochemistry of carbonates as a proxy for deep-time environmental reconstruction. Paleogeogr. Palaeoclimatol. Palaeocol. 574:21p.